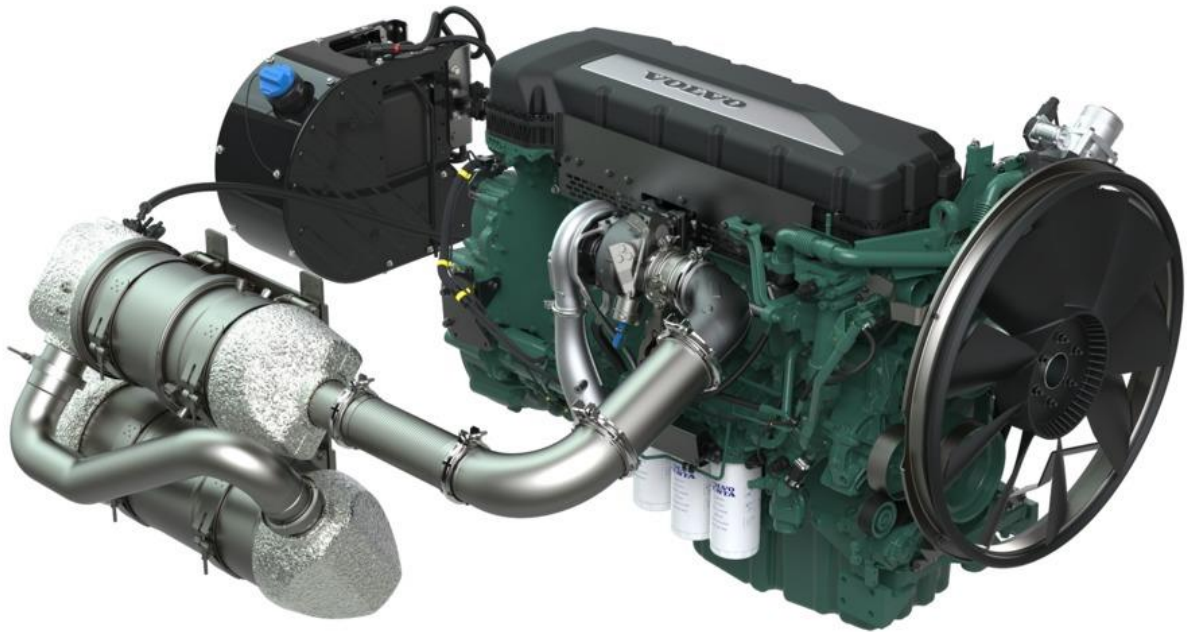




CHALMERS
UNIVERSITY OF TECHNOLOGY



Calibration and Validation of a 1D model for Exhaust Aftertreatment System in Heavy Duty Diesel Engines

Master's thesis in Automotive Engineering

Hongda Cen

MASTER'S THESIS IN AUTOMOTIVE ENGINEERING

Calibration and validation of a 1D Model for Exhaust Aftertreatment System in Heavy Duty Diesel Engines

Hongda Cen

Department of Mechanics and Maritime Sciences
CHALMERS UNIVERSITY OF TECHNOLOGY
Göteborg, Sweden 2018

Calibration and Validation of a 1D model for Exhaust Aftertreatment System
in Heavy Duty Diesel Engines
Hongda Cen

© Hongda Cen, 2018

Master's Thesis 2017:81
Department of Mechanics and Maritime Sciences
Chalmers University of Technology
SE-412 96 Göteborg
Sweden
Telephone: + 46 (0)31-772 1000

Cover:
TAD1180-1182VE, Stage V, Aftertreatment

Göteborg, Sweden 2018

Calibration and Validation of a 1D model for Exhaust Aftertreatment System in Heavy Duty Diesel Engines
Master's thesis in Automotive Engineering
Hongda Cen
Department of Mechanics and Maritime Sciences
Chalmers University of Technology

Abstract

Diesel engines are faced with more stringent legislation for higher fuel efficiency and lower emissions. New technologies have been designed to meet these needs. Volvo Penta has started a project called virtual test cell for increasing the effectiveness of verification and validation process. The goal is to reduce the testing and calibration time in physical test cells and increase the quality of products by moving part of activities to the virtual test cell. A model in the virtual test cell should be fast and have a shorter lead time. The current thesis was performed as a part of the Virtual Calibration project in collaboration with Chalmers University of Technology. It aims to refine an existing 1D model for exhaust gas aftertreatment system for Volvo Penta's configuration.

One of the key objectives of this thesis is to carry out the calibration work on a 1D Diesel oxidation catalyst (DOC) and Diesel particulate filter (DPF) chemical model in MATLAB/ Simulink. The model predicts temperature, pressure drop, soot loading and concentrations of NO_x , CO and HC. The work includes tuning the reaction rate parameters such as activation energies and pre-exponent factors in the purpose of minimizing the difference between experimental and simulation results. The other objective is to validate the model to evaluate if a 1D model is good enough to be used in a virtual test rig.

The model was calibrated to a steady state cycle called part load map (PLM). Temperatures and mass flow were high in the beginning and going down to lower as time elapsed. The result shows that the model accuracy is improved after the calibration. The temperature deviation becomes larger at high torque, and the errors of CO and HC concentrations are higher at a lower temperature. The residual of NO concentrations is mainly due to the temperature deviation and unknown initial soot loading in the DPF. The error of pressure drops across the DPF also comes from the unknown initial soot loading in the DPF. The model was then validated to a nonroad transient cycle (NRTC). The model errors become quite high at the transient points.

In the future, further calibration against transient data is needed to fully calibrate the model.

Keywords: Calibration, Validation, Diesel oxidation catalyst, Diesel particulate filter, Kinetic modelling, 1D simulation, MATLAB Simulink, Parameter estimation

Acknowledgments

This master thesis was carried out at AB Volvo Penta, Sweden, from June 2017 to October 2017. The work is a part of the Virtual Engine Calibration (VirCal) project funded by Fordonsstrategisk Forskning och Innovation (FFI) and Vinnova. The DOC and DPF chemical model used in this thesis are provided by Volvo Trucks in North America. Here, I wish to thank everyone who has accompanied and helped me along the way.

First, I would like to thank my examiner Jonas Sjöblom at Chalmers who is indeed an expert in Chemistry. For his interest in and continuous support and patient guidance in my thesis, I have learned the fundamentals of catalytic reaction and gained full of professional advice on analysis of test results. I want to appreciate my supervisor Jelena Andric at Chalmers who has organized the project, for her encouragement throughout my entire thesis and valuable revision of my report.

I want to extend my appreciation to Ethan Faghani, project manager of Engine Testing and Laboratories at Volvo Penta, for giving me the opportunity to contribute to the fantastic work we do and the best work environment. You always take the time to listen to my questions and discuss my work whenever needed. I would like to send special gratitude to my supervisor Qunlong Dong, in the Hagerstown North America site of Volvo. You have always patiently answered my questions by email and Skype meetings. I have learned much knowledge about Simulink model and calibration process. Then I would also like to acknowledge Sara, the engineer of the exhaust aftertreatment system team, who has given me the measurement data for model validation. Anton, the engineer of the Engine Testing team, who has helped me investigate the model accuracy. There are still some names may not be listed here, but I would like to acknowledge all of them for their kindness supporting throughout my work.

I also want to thank the other Master student Frida, who has done her thesis earlier at Penta. You have given me the data to start the project, and I have gained the inspiration by reading your thesis report.

Finally, I would like to gratitude my family and friends. Thank you for your encouragement and company.

Thanks,

Göteborg, January 2018

Hongda Cen

Contents

Notations	IX
1 Introduction	1
1.1 Background	1
1.2 Problem formulations and Purpose	3
1.3 limitations	3
1.4 Method and outline.....	3
2 Theoretical background	5
2.1 Heterogenous catalysis	5
2.2 Diesel oxidation catalysts.....	8
2.3 Diesel particulate filters.....	9
3 Model formulations	11
3.1 Model structure	11
3.2 Model assumptions	14
3.3 Heat transfer in the pipe	14
3.4 Chemical reactions	16
3.4.1 DOC	16
3.4.2 DPF	17
3.5 Flow-through substrate governing equations	18
3.6 Boundary and initial conditions	20
3.7 Pressure drop	20
3.8 Numerical solver and calculation flow chart	22
4 Calibration	23
4.1 preparation	23
4.2 Adjustable parameters	25
4.2.1 DOC model	25
4.2.1.1 Heat transfer parameters for DOC.....	25
4.2.1.2 Mass transport and kinetic parameters for DOC	26
4.2.2 DPF model	28
4.2.2.1 Heat transfer parameters for DPF.....	28

4.2.2.2	Mass transfer and kinetic parameters for DPF	28
4.2.2.3	Soot accumulation and pressure drop parameters for DPF	30
4.3	Parameter estimation.....	31
4.3.1	Estimation method	31
4.3.2	Processing measurement data	33
4.3.3	Parallel computing	34
5	Results and discussion	35
5.1	DOC calibration results	35
5.1.1	Tuning of parameters for DOC model.....	35
5.1.2	Temperature for DOC	37
5.1.3	CO concentrations for DOC	39
5.1.4	HC concentrations for DOC	44
5.1.5	NO concentrations for DOC	46
5.2	DOC model validation	49
5.2.1	DOC temperature validation	49
5.2.2	CO concentrations of DOC validation	51
5.2.3	HC concentrations of DOC validation	52
5.2.4	NO concentrations of DOC validation	53
5.3	DPF calibration results	55
5.3.1	Tuning of parameters for DPF model	55
5.3.2	Temperature for DPF	58
5.3.3	HC concentrations for DPF	60
5.3.4	NO concentrations for DPF	62
5.3.5	DPF pressure drop	64
5.4	DPF model validation	66
5.4.1	DPF temperature validation	66
5.4.2	Validation of other gas species concentration and pressure drop.....	67
5.5	Combined DOC and DPF model validation	67
5.5.1	Temperature PLM validation of DOC+DPF	67
5.5.2	Temperature NRTC validation of DOC+DPF	69
6	Summary and conclusion	70
7	Future work.....	71
	Reference.....	73

Appendix	75
A User’s guide in Simulink Design optimization	75
B DOC model calibration results	77
C DOC model validation results	82
D DPF model calibration results	83
E DPF model validation results	88
F Combined DOC and DPF model validation using PLM	94
G Combined DOC and DPF model validation using NRTC	101

Notations

A_i	Pre-exponential factor of the i^{th} species [1/s]
AL_Th_ch	Characteristic ash layer thickness for soot filtration [m]
$Clean_Wall_$	
$Cake_PM_Frac$	Fraction of PM trapped on top of the wall for an ash free DPF
$c_{p,g}$	Gas specific heat capacity [J/(kg·K)]
$c_{p,s}$	Substrate specific heat capacity [J/(kg·K)]
$c_{p,steel}$	Steel pipe specific heat capacity [J/(kg·K)]
D_i	The effective diffusivity for washcoat [m ² /s]
D_{AB}	The binary gas phase diffusivity [m ² /s]
d_c	Loaded collector diameter [m]
$d_{c,0}$	Clean collector diameter [m]
d_h	Hydraulic diameter [m]
d_{pore}	Pore diameter [m]
$E_{a,i}$	Activation energy of the i^{th} species [kJ/mol]
F	Friction factor equal to 28.454
F_wall	Reaction rate enhance factor for in-wall soot regeneration due to better contact with catalyst and higher local NO ₂ concentration than the flow channel.
G	Inhibition factor
GSA	The specific geometric surface area [m ² /m ³]
h	Convective heat transfer coefficient [W/(m ² ·k)]
K_i	Reaction rate constant [1/s]
Kn	Knudsen number
k_0	Nominal permeability [m ²]
k_{ash}	Ash layer permeability [m ²]
k_{soot}	Soot layer permeability [m ²]

k_{wall}	Filter wall permeability [m ²]
$k_{m,i}$	Mass transfer coefficient [m/s]
k_u	Kuwabara geometric function
L	Channel length [m]
MW	Gas molecular weight [g/mol]
$mass_{cat}$	Monolith mass per grid [kg]
Nu	Nusselt number [-]
OFA	Open frontal area (void fraction) [-]
P	Exhaust gas pressure (Pa)
Pr	Prandtl number [-]
Q	Exhaust volumetric flow rate [m ³ /s]
q	Heat transfer rate [W/m ²]
R	Molar gas constant equal to 8.314 [J/(mol·k)]
Ra	Rayleigh number [-]
Re	Reynolds number [-]
r_i	Reaction rate of i th species [mol/(s·m ³)]
SCF	Stokes-Cunningham slip correction factor [-]
SL_Th_ch	Characteristic soot layer thickness for soot filtration [m]
T_g	Gas temperature [k]
T_s	Solid wall temperature [k]
u_g	Gas velocity [m/s]
V_{trap}	Filter volume [m ³]
w_{ash}	Ash layer thickness [m]
w_{soot}	Soot layer thickness [m]
w_{wall}	Filter wall thickness [m]
W_{SL_Lim}	DPF wall maximum soot load, porous wall cannot take soot more than this level [g/L]
X	Axial direction of the channel
X	

Y_i	Concentration of i^{th} species [mol/m^3]
Greek letters	
ΔH_i	Heat of reaction of the i^{th} species [J]
ΔP	Pressure drop across the DPF
ΔT	Adiabatic temperature rise
ε	loaded filter porosity
ε_0	Nominal porosity
ϵ	Surface emissivity
λ	Exhaust gas-mean-free-path
λ_{air}	Thermal conductivity in air
λ_{gas}	Thermal conductivity in exhaust gas
μ	Gas dynamic viscosity [$\text{kg}/(\text{m}\cdot\text{s})$]
ν	Gas kinematic viscosity [m^2/s]
ξ_E	Pressure loss coefficient for channel in and out minor losses
ρ	Density [kg/m^3]
σ	Stefan-Boltzmann constant, equal to $5.676\cdot 10^{-8}$ [$\text{W}/\text{m}^2\cdot\text{k}$]

Definitions and abbreviations

ASC	Ammonia Slip Catalyst
CO	Carbon monoxide
CO ₂	Carbon dioxide
DOC	Diesel Oxidation Catalyst
DPF	Diesel Particulate Filter
EATS	Exhaust Aftertreatment system
EGR	Exhaust gas recirculation
NO	Nitrogen oxide
NO ₂	Nitrogen dioxide

NRTC	Nonroad Transient cycle
PLM	Part Load Map
PM	Particulate Matter
SCR	Selective Catalytic Reduction
TWC	Three-way Catalyst

1 Introduction

This chapter describes the topic of the thesis. Based on that information, the problem is formulated followed by limitations and method.

1.1 Background

Diesel engines are widely used in cars, highway trucks, ships, and construction equipment, taking advantage of their excellent performance in power and fuel efficiency, high durability and reliability. However, diesel engines emit higher quantities of nitrogen oxides (NO and minimal levels of NO₂, collectively known as NO_x) and particulate matter (PM), also referred to soot. They are major contributors to environmental pollution and are harmful to human health. NO is formed during the combustion with high temperature and excess of oxygen in the air and fuel mixture. It is a major contributor to the formation of the ozone, acidification and smog formation [1]. PM, consists mainly of carbonaceous matter, is formed during the combustion with low temperature and high local fuel-air equivalence ratio [2]. PM emissions may cause severe health problems like asthma, lung cancer and other cardiovascular issues [1]. Fine particulates (PM_{2.5}: diameter<2.5um) and ultra-fine particulates (PM_{0.1}: diameter<0.1um) can easily penetrate deep into the lung and cause illness in the human respiratory system [3].

Apart from NO_x and soot, there are also hydrocarbons (HC) and carbon monoxide (CO) in the exhaust which also contribute to heavy pollution. Hydrocarbons are composed of unburned fuel, partially decomposed fuel molecules or recombined intermediate compounds [2]. They are normally produced in low quantities in diesel engines. There are two primary sources of Hydrocarbons emissions under normal engine operating conditions: fuel is mixed too lean to auto ignite when the fuel is injected during the ignition delay period, or at the end of fuel injection process, fuel leaves the injector nozzle at low velocity and engages in combustion process lately, which lead to slower mixing with the air and local fuel rich region formation [4]. Hydrocarbons are toxic. They contribute to the formation of ground-level ozone and are potential to respiratory tract irritation and cause cancer [1]. Carbon monoxide is formed mainly due to incomplete combustion when an oxygen shortage occurs. CO is an odorless and colorless gas. When CO is inhaled by the lungs and entered the bloodstream, it can inhibit hemoglobin's capacity to transfer oxygen. This will lead to asphyxiation and make different organs operate abnormally, resulting in impaired concentration, slow reflexes, and confusion [1]. However, CO is usually minimal in diesel engines and considered to be unimportant, since the diesel engine is operating leanly with an abundant amount of air to oxidize the fuel to CO₂ fully.

Many emission regulations have been developed and implemented over the decades, to control and restrict these pollutants. As an example, table 1.1 shows the development of European emissions standards for diesel engines in non-road.

Table 1.1 EU Stage I-V emission standards for non-road diesel engines [5].

Cat	Net power (kW)	Date	CO (g/kWh)	HC (g/kWh)	NO _x (g/kWh)	PM (g/kWh)
Stage I	130≤P≤560	1999	5	1.3	9.2	0.54
Stage II	130≤P≤560	2002	3.5	1	6	0.2
Stage III	130≤P≤560	2011	3.5	0.19	2	0.025
Stage IV	130≤P≤560	2014	3.5	0.19	0.4	0.025
Stage V*	130≤P≤560	2019	3.5	0.19	0.4	0.015

* Stage V: refer to all types of engines which are above 56kW

As seen in table 1.1, regulation becomes only increasingly stringent for lower emissions. Especially for NO_x and PM in recent years. One of the technologies which can achieve a significant decrease in NO_x emissions is exhaust gas recirculation (EGR). The exhaust gas is returned to the combustion chamber, mixing with intake air, resulting in the lower combustion temperature and oxygen concentration, which can reduce NO_x formations [6]. However, only with the EGR cannot meet current emission standards of NO_x. Moreover, due to the reducing of temperature and less oxygen available, it can favor the formation of PM, HC and CO. Therefore, a diesel engine requires an exhaust aftertreatment system (henceforth EATS) to reduce all of them. Figure 1.1 illustrates a flow layout of EATS that includes a diesel oxidation catalyst (DOC), a catalyzed diesel particulate filter (DPF) and a urea-based Selective Catalyst Reduction (SCR) with an ammonia slip catalyst (ASC).

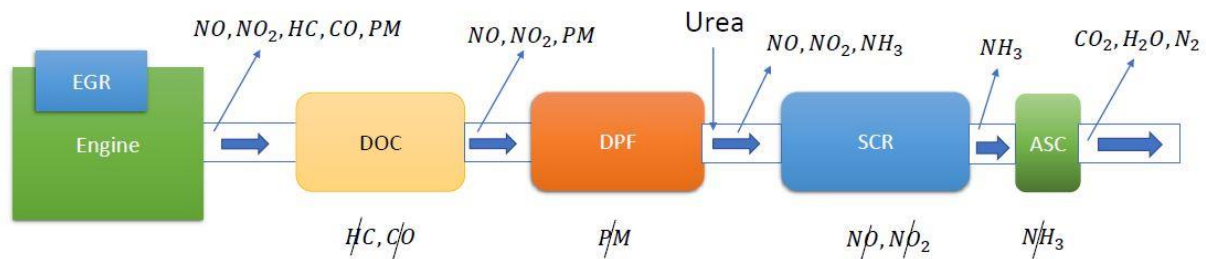


Figure 1.1 Schematic layout of exhaust aftertreatment system of diesel engines.

DOC is used to oxidize HC and CO to carbon dioxide (CO₂) and water (H₂O), together oxidize NO to NO₂. More generated NO₂ will promote low temperature PM oxidation in the DPF, and a desirable NO₂/NO_x ratio will benefit to the SCR performance. DPF capture PM while burning the PM which is called regeneration. SCR can be used to reduce NO_x to N₂ and H₂O. It uses ammonia (NH₃) as the reductant. NH₃ is usually stored in liquid form as water urea solution onboard since it is less hazardous and safely transported on travels. The final step, ammonia slip can be controlled by the ammoniac slip catalyst (ASC) installed downstream of SCR catalyst [7].

Volvo Penta has recently started a project called virtual test cell. The goal is to reduce the testing and calibration time in physical test cells and increase the quality of products by moving part of activities to the virtual test cell. A model in the virtual test cell should be fast and accurate.

There is an existing EATS model developed by Volvo Trucks in North America for US 10 EATS which is expected to be modified for the Volvo Penta applications. However, the reaction kinetics is complex. Reaction rates can be different for each catalyst which has a different aging condition. Reutilizing kinetic parameters from other literature may be inappropriate, which leads to the incorrectness of the model. Therefore, it is required calibration of kinetic parameters for a better model accuracy by

input from test cell and manufacturer data. These kinetic parameters are the activation energies and pre-exponential factors which need to be adapted to the model.

1.2 Problem formulations and purpose

One of the key objectives of this thesis is to carry out the calibration work on a 1D Diesel oxidation catalyst (DOC) and Diesel particulate filter (DPF) chemical model in MATLAB/ Simulink. The work includes tuning the reaction rates parameters in the purpose of minimizing the difference between experimental and simulation results. The work will also increase the understanding of heterogeneous catalyst system by investigating different phenomena during the simulation (at low and high temperature). Finally, the work should also validate the model accuracy using another test cell data to evaluate if a 1D model is good enough to be used in a virtual test rig.

- Develop a model calibration methodology with the help of parameter estimation toolbox to improve the model development, especially for a heterogeneous catalyst system
- Optimize heat transfer, reaction kinetics and mass transport parameters for the model.
- Study how the rate of conversion can be affected by kinetics and mass transfer. Study how the exhaust flow and temperature can influence the reaction during different engine operating points.
- The model, after being calibrated with measurement data can be used to describe the chemical reactions inside the catalyst.

1.3 limitations

This thesis work is limited to DOC and DPF model calibration. The calibration and validation of SCR and ASC will not be carried out due to the time plan of the project. The data using for calibration and validation are limited to test cell data. There is no specific DOE (Design of experiments) and no flow bench testing. Moreover, it is recommended to calibrate DPF model with clean filter data (the initial soot loading is zero before the measurement). However, only used filter data was available in this work. Furthermore, a method for parameter sensitivity analysis or calculation of parameter confidence intervals is out of the scope of this work.

1.4 Method and outline

The method in this thesis is first to carry out a literature study to gain a basic understanding of chemical and physical phenomena included in DOC and DPF systems. Then to load the provided test cell data and the hard specifications of Penta EATS system to the model correctly. When this is done, the calibration will be carried out to estimate the model parameters. The calibration work will be divided into two parts. First, to calibrate the DOC model and then the DPF. This will be done to avoid too many parameters that will be estimated simultaneously, which saves the computation time and reduce the correlation among the parameters. The software using for tuning parameters is MATLAB Simulink Design Optimization. When defining the parameters ranges, it can estimate multiple parameters during the simulation. The optimization method using in this work is nonlinear least squares. In each iteration, it computes and minimizes the error between the simulated and experimental outputs. If the method finds a local minimum, the estimation will converge and

terminate. After this above, the plot analysis for the calibration results will be done. Each model will be validated against another set of measurement data, which investigates the performance of the calibrated parameters. Finally, two individual models will be linked together and without extra calibration, a validation for the combined model will be performed. The summary and conclusion will be done in the end.

This thesis consists of seven chapters, which includes this introductory chapter. In the remainder of this paper, chapter 2 presents the theoretical background on heterogenous catalytic reaction, DOC and DPF. Chapter 3 introduces the overview of the DOC and DPF model with the mathematical equations for conservation and governing law in DOC and DPF system. Chapter 4 presents the calibration procedure, including test cell data to calibrate and validate the model. Adjustable parameters and the parameter estimation toolbox are also described in this chapter. Chapter 5 shows the results for tuning of the model parameters. The calibration effect and validation results are provided by plotting. The residual analyses also follow the discussion. Chapter 6 presents the summary and conclusions of this thesis. Many tasks still needed to be considered in the future. Some suggestions for future directions are left as future work in chapter 7.

2 Theoretical background

In this chapter, the fundamentals of catalytic reaction are introduced. The theory of diesel oxidation catalysts and diesel particulate filters are briefly explained. These are presented to increase an understanding of the background to the thesis goal.

2.1 Heterogeneous catalysis

A catalyst is a substance that can influence a reaction rate without being consumed in the reaction. It is neither one of the initial reactants nor final products. It can increase the rate by lowering the activation energy that the reactants must overcome, while does not alter the energies of the original and final states [8]. With catalysts, the reactions can occur at relatively low temperatures compared to the reactions without catalytic species. This can benefit the emission control process at temperature levels which are typical for engines. Figure 2.1 shows the energy path with and without a catalyst.

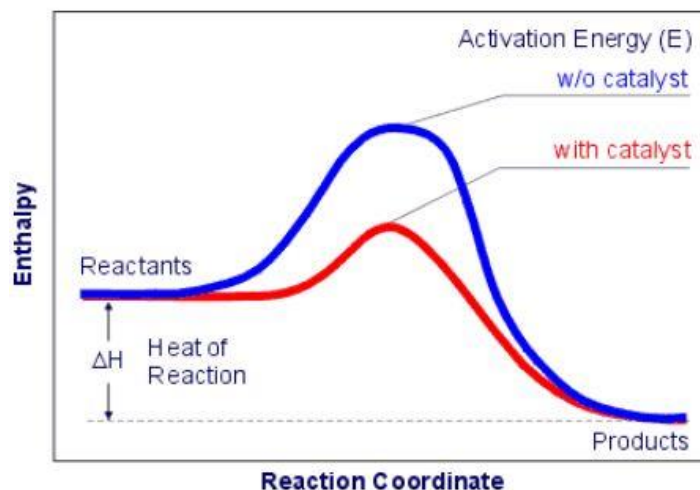


Figure 2.1 Reaction energy paths [8], reproduced with permission.

The catalyst system can be heterogeneous means that the catalyst is in a different phase than the reactants. In the exhaust aftertreatment, the reactants are gaseous, and the catalysts are noble metals, which are most commonly platinum group metals (PGM). They are suitable to be used as catalytic materials due to their high intrinsic activity. They are also known as active centers. The reaction rate depends on the number of active centers present. Faster rate requires more active centers. To increase the number of active centers, they are dispersed on a high surface area and within porous oxide support (carriers). The exhaust gases diffuse through the porous carrier to the active centers where the reactions take place. The most common carrier is alumina (Al_2O_3), which is called washcoat and coated on a substrate [8]. Figure 2.2 shows the dispersed catalysts on the washcoat.

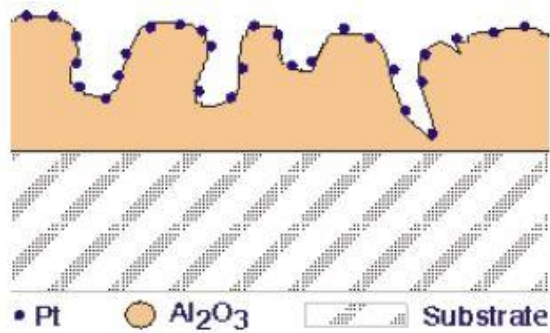


Figure 2.2 Active centers dispersed on a carrier [8], reproduced with permission.

The substrate is an extruded monolithic honeycomb which is made of cordierite (a synthetic ceramics). The honeycomb structure consists of many small parallel channels and sometimes called “flow-through” substrates. Its advantage is to increase the contact area between the gases and catalysts [9]. Figure 2.3 illustrates the structure of monolithic catalyst support.

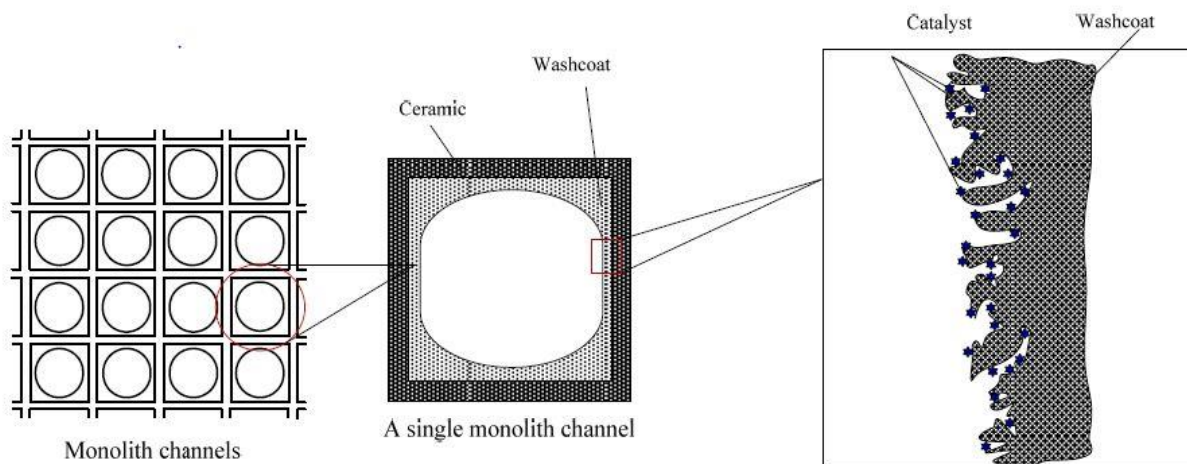


Figure 2.3 Illustration of the structure of monolithic catalyst support [10].

Both physical (mass transfer) and chemical (reaction kinetics) phenomenon can describe the conversion rate in heterogenous catalysts. They can be divided into seven steps [8]:

1. Bulk diffusion of reactants: The reactants must diffuse through the boundary layer to contact the catalysts at the outer surface of the washcoat.
2. Pore diffusions of reactants: Most of the reactants molecules must diffuse again through the porous washcoat into the internally dispersed active centers.
3. Adsorption of reactants: Chemisorption of reactants onto active centers.
4. Catalytic reaction: the reactions take place, and the reactants are converted into the products at the active centers.
5. Desorption of products: The products desorb from the active centers
6. Pore diffusions of products: Products diffuse through the porous washcoat to the outside surface.
7. Bulk diffusion of products: Products must diffuse again through the boundary layer toward the bulk gas.

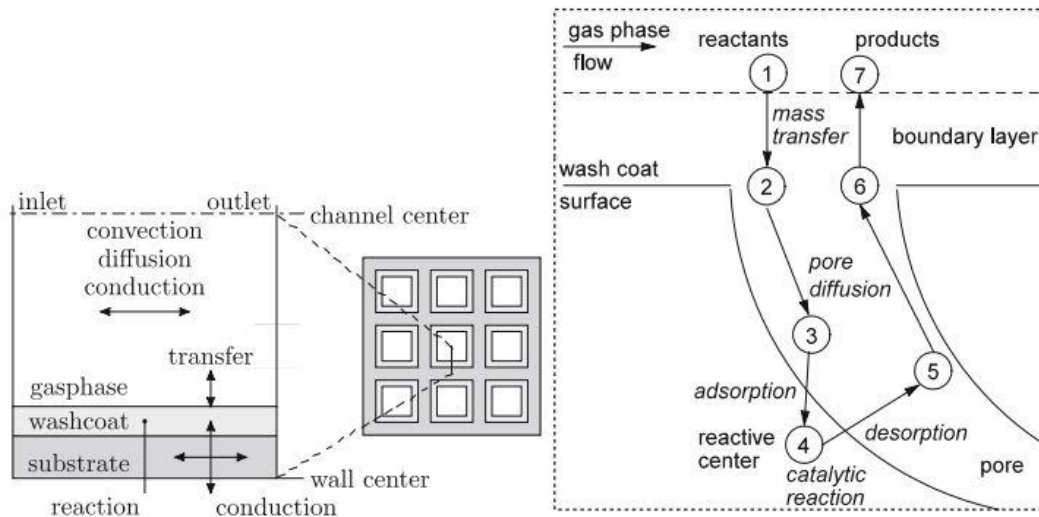


Figure 2.4 Schematic of a heterogenous catalytic reaction process [11].

The above steps are then classified into three main processes, chemical reaction, pore diffusion, and bulk mass transfer. Figure 2.5 illustrates the conversion efficiency against temperature. At low temperatures, the rate of chemical kinetics (step 3,4 and 5) is slower than the diffusion. The reaction kinetics controls this region. When the temperature increases, the reaction rates become faster as an exponential dependence on temperature. Pore diffusion (step 2 and 6) oversees the overall rate. Lastly, at high temperatures, both reaction kinetics, and pore diffusion rates are very fast, the control of the rate shifts to the mass transfer (step 1 and 7) due to that it has a lower dependence on temperature [8].

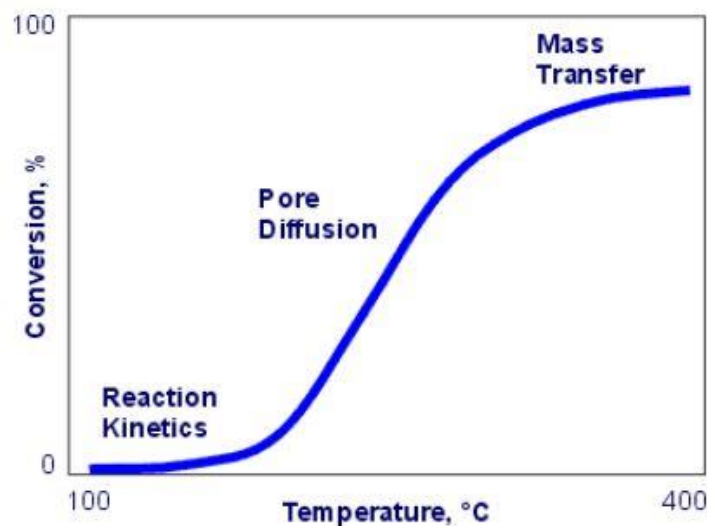


Figure 2.5 Regions for the rate limiting [8], reproduced with permission.

2.2 Diesel oxidation catalysts

DOC oxidizes CO and HC to CO₂ and water when there are sufficient amounts of oxygen present in diesel exhaust. Figure 2.6 shows the conversion efficiency of CO and HC in typical noble metal diesel oxidation catalyst. As seen in figure 2.6 (a), the conversions of CO and HC are almost zero at very low exhaust temperatures. Once the temperature increases, the conversions will also be higher, indicating the increase in the oxidation rate of CO and HC. Since HC and CO will mainly react with the oxygen instead of NO_x, therefore, DOC does not reduce NO_x but oxidizes NO to NO₂, which lead to adjusting of the NO₂/NO_x ratio. More generated NO₂ will promote low temperature PM oxidation in DPF, and a desirable NO₂/NO_x ratio will benefit the SCR performance. However, the rate of oxidation of NO will be limited at higher temperatures due to the thermodynamic equilibrium. The reaction will occur in the reverse direction rather than further progress. Even the catalysts cannot break the equilibrium but increase the reaction rate of the reverse reaction [8]. Figure 2.6 (b) illustrates NO conversion as a function of temperature. In all cases, the NO conversion begins to decay at around 250-350 °C due to the thermodynamic constraints.

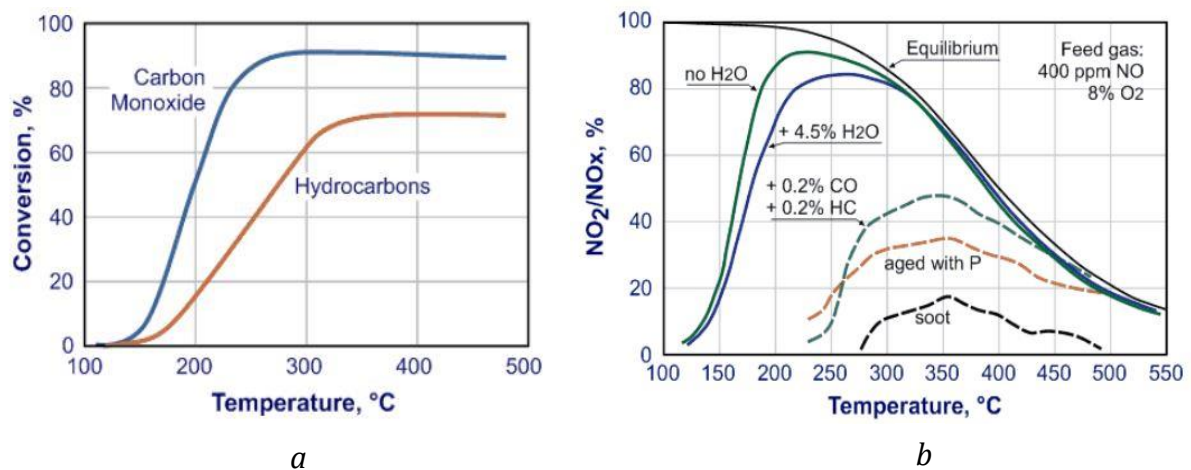


Figure 2.6 Conversion efficiency of CO, HC, and NO against temperatures in DOC [12], reproduced with permission.

PM (Here are referred to carbonaceous matters or soot) generally remains unchanged after passing through the DOC, because they have a large size compared to gas molecules and they have very small opportunity to contact with the active centers. Even if they can come into the catalysts, the rate of soot oxidation is much lower than that of CO and HC oxidation. Due to the short residence time and insufficient exhaust temperature, it is difficult to achieve any oxidation. Therefore, it is desirable to prolong the residence time by trapping the soot through the diesel particle filter [12], [13].

2.3 Diesel particulate filters

DPF is used to eliminate PM (apart from the soot, also consisting of ash, soluble organic and sulfate particulates. In the following, PM will be referred as soot for simplicity). The substrate of DPF is most commonly ceramic wall-flow monolith, which is obtained from the flow-through monolith. It is formed that at the inlet, the channel is plugged by an alternating way, so half of the inlet is plugged, and the other half will be closed at the outlet, thus forcing the flow to go through the porous wall and the structure acts as a mechanical filter. The filtration efficiency is more than 90%, which makes it an efficient design for trapping the PM [14]. Figure 2.7 shows the gas movement through the wall-flow monolith compared to the flow-through monolith.

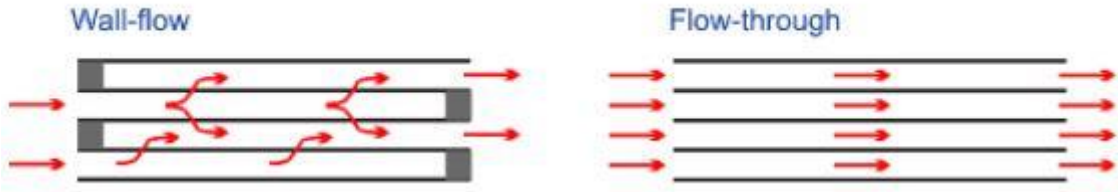


Figure 2.7 wall-flow and flow-through substrates [14], reproduced with permission.

There are two filtration mechanisms: deep-bed filtration and surface filtration. At the beginning with a clean filter, soot is deposited on the filter media through the deep-bed filtration. The mean diameter of the soot is smaller than the mean pore size of the filter, allowing the deposition of soot. After the porous wall is totally filled with the soot, soot starts forming a soot cake layer on the wall which is itself the filter medium. This type of filter is surface (cake) filtration. The pore diameter of the cake layer is less than the soot diameter, allowing a deposition through sieving [14]. The difference between deep-bed filtration and surface filtration is illustrated in figure 2.8.

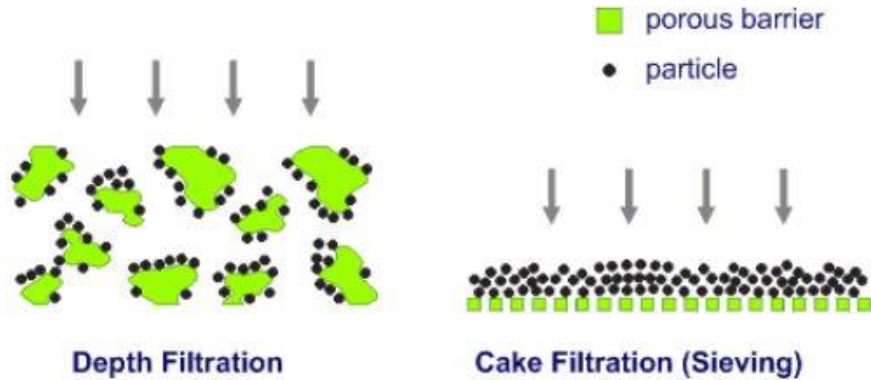


Figure 2.8 Two filtration mechanisms [14], reproduced with permission.

The formation of the cake layer can improve the filtration efficiency, thus trapping more soot. However, this will also create more flow resistance which causes an increase in back pressure or pressure drop. As a rise of the pressure drop level, the engine must produce more mechanical work to compress the exhaust gases to higher pressure in order to let them leave the cylinder [15]. This

will increase fuel consumption. Therefore, the collected soot should be burned by oxidation, which is called regeneration. There are two types of regeneration methods, known as active regeneration and passive regeneration. Active regeneration is oxygen-based regeneration. Soot oxidation is effective at temperatures about 600 °C, whereas, at the lower temperatures, the rates of the oxidation are very slow [13]. Unfortunately, often, the operating temperature is not high enough. Hence, the active regeneration uses late fuel injection in the engine or an external heat source like an electric heater or flame-based burner to oxidize the soot. Figure 2.9 shows the soot oxidation rates at different temperatures.

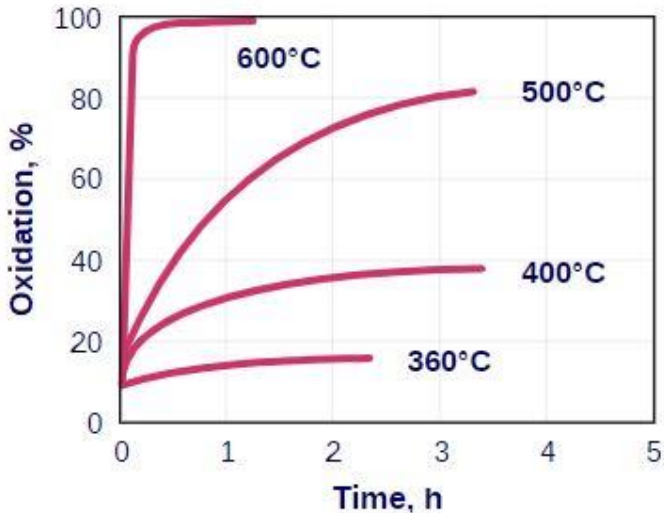


Figure 2.9 Soot oxidation rates [13], reproduced with permission.

It was found that NO₂ can be an oxidant more active than oxygen at low temperatures. With NO₂, the oxidation rates are noticeable at temperatures around 250 C, as illustrated by figure 2.10. In passive regeneration, the oxidation can occur at the low temperatures using NO₂ as the oxidizer. The DPF is also coated with the catalysts to promote the NO oxidation and hence increase the concentration of NO₂.

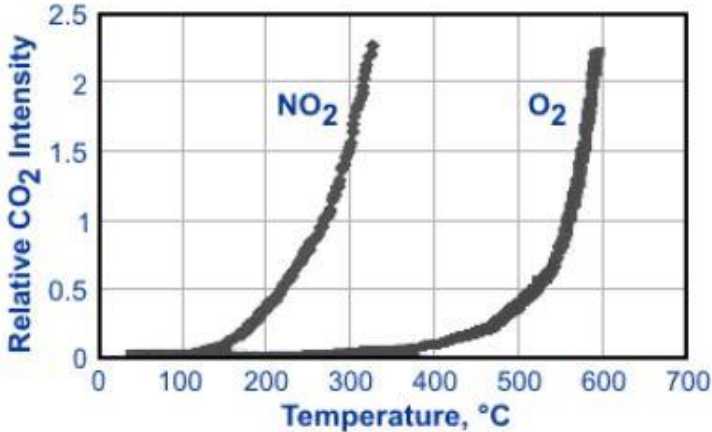


Figure 2.10 Soot oxidation by O₂ and NO₂ [13], reproduced with permission

3 Model formulations

In this chapter, the DOC and DPF chemical model is presented. The model is based on the conservation equations for mass, momentum, and energy with appropriate simplifications for diesel catalyst. The equations are solved numerically using simple first order Euler solver. The model then can predict the outlet temperatures, pressures, NO, NO₂, CO, HC concentrations and soot loading. Section 3.1 describes the model's structure. Section 3.2 presents the model assumptions. Section 3.3 describes the heat transfer across the pipe. Section 3.4 presents an overview of the chemistry in DOC and DPF. Model conservation equations (energy, momentum, and mass) for both solid and gas phases are demonstrated in section 3.5. Section 3.6 presents boundary and initial conditions, while section 3.7 describes the equations of the pressure drop model in the DPF. Finally, the numerical solver utilized in Simulink is presented.

3.1 Model structure

Model in this thesis consists of a sub DOC model and a sub DPF model. By connecting the output signals from the DOC model to the DPF input signals, the connecting between two systems can be achieved, see figure 3.1.

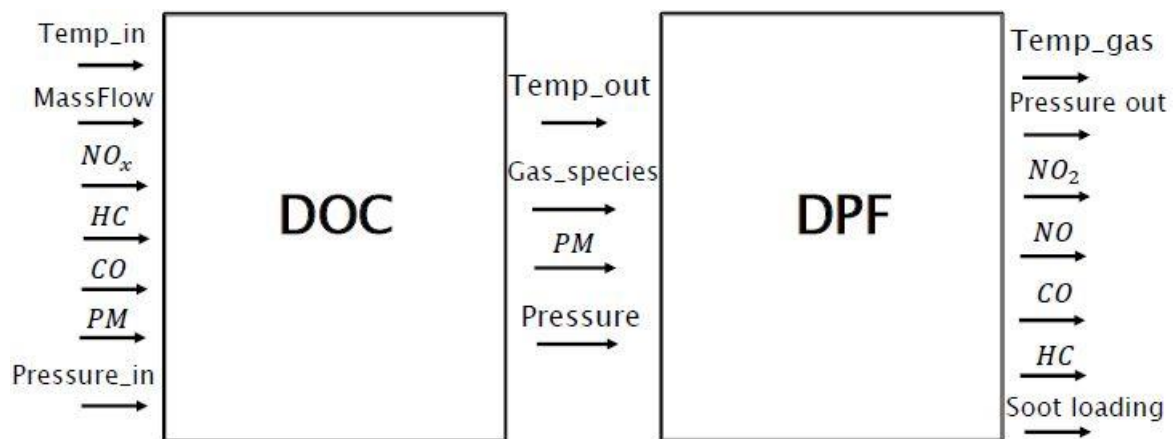


Figure 3.1 An overview of the DOC and DPF model used in this thesis. Abbreviations in the figure: Temp (Temperature), MassFlow (Exhaust mass flow).

Figure 3.2 and 3.3 illustrate the modeling of sub DOC model. DOC model consists of a pipe module which calculates the heat losses when exhaust flow goes through the pipe. The close behind is a mole fraction calculation module aiming for dealing with input species concentrations, and three sub elements with the same length connected behind. Each sub element is identical and represents a DOC grid where a thermal module and a chemical module are inside there. The thermal module calculates the exhaust gas temperature at the DOC outlet and the wall temperature which used as a reaction temperature of the chemical module. The chemical module contains a reversible NO oxidation reaction, HC and CO oxidation reactions. The inhibition factor is calculated based on the concentrations of HC, CO and NO.

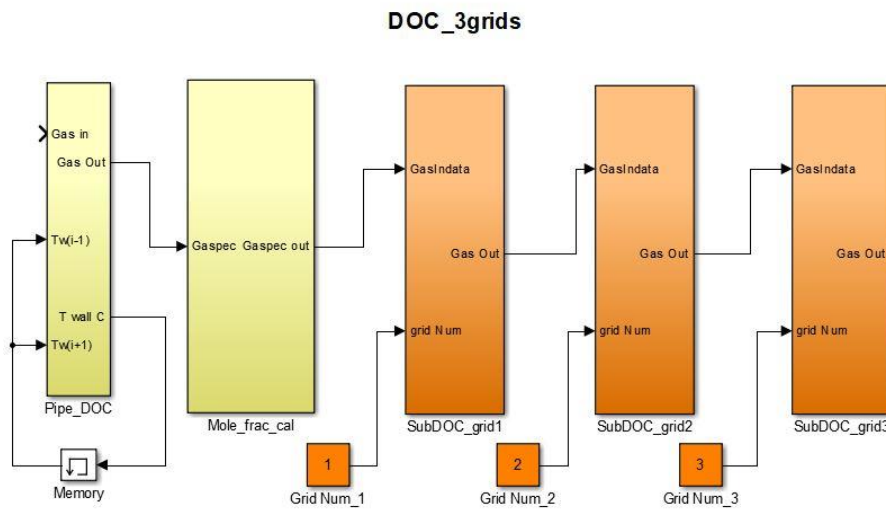


Figure 3.2 A schematic illustration DOC model in Simulink.

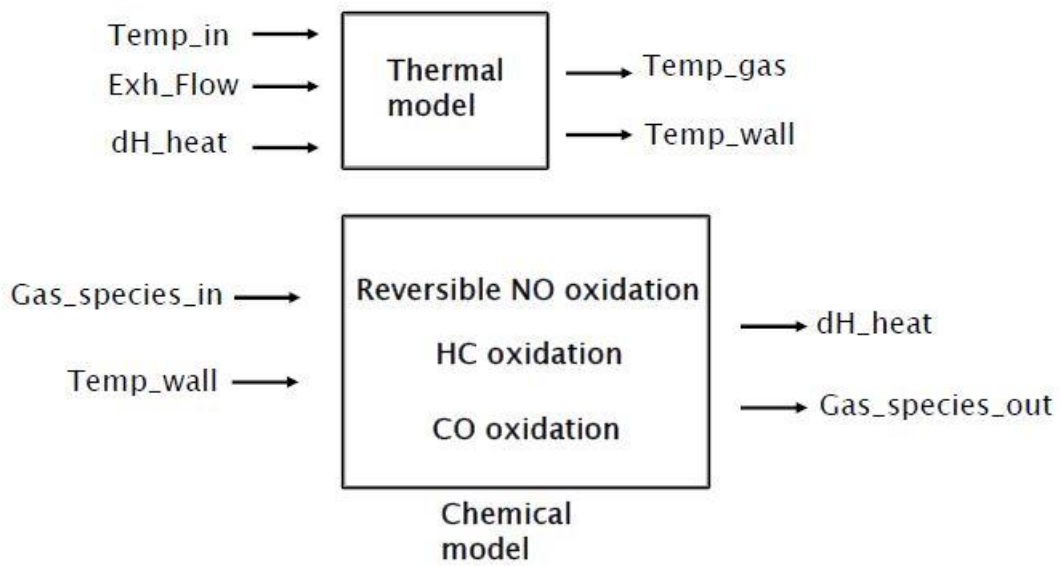


Figure 3.3 An overview of a DOC grid model. Abbreviations in figure: dH_{heat} (Heat release due to the oxidation).

The DPF model consists of three components which are one 0-D soot oxidation, and filtration model, one DPF 6 grids model and one 0-D pressure drop model, see figure 3.4.

The DPF 6 grids model is quite similar to the DOC grids model. The difference is, there is an extra NO formation due to the passive soot regeneration.

The 0-D soot oxidation and filtration model predicts the soot loading in the DPF filter. It consists of both passive and active mechanisms. The passive and active regeneration is with the temperature and NO₂ % from the sub element grid three from the DPF 6 grids model, to take the effects of on-site consumed and reformed NO₂. In the model, total soot load is divided into the load in soot cake and load in the porous wall. The formation of soot cake will reduce and even stop particulates accumulation to the porous wall, but passive regeneration by NO₂ still occur in the porous wall which results in a gradual decrease of the soot load in the wall.

The pressure drop model is based on the load filter case investigated by Konstandopoulos et al. [16]. The effects of in-wall soot loading with mean pore size and permeability are included. Flows in soot cake and filter wall have a slip and transitional effects when the mean-free-path of the gas molecules approaches the pore size of the porous medium. The details of the calculation of the pressure drop is introduced in section 3.7, on page 20.

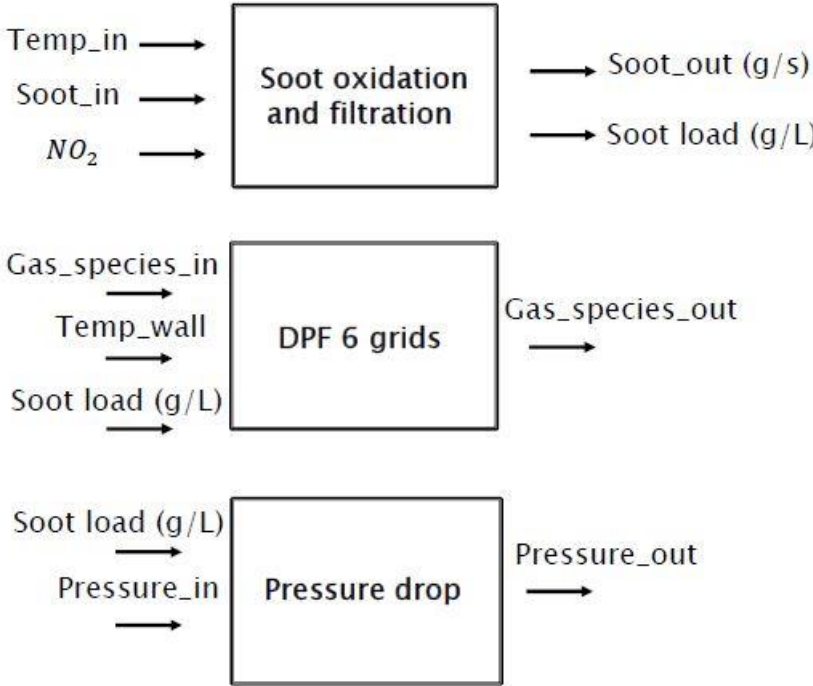


Figure 3.4 Modeling of the DPF model

3.2 Model assumptions

The basic assumptions used in this model are [17]:

- Heat and mass transfer between gas and solid phases in catalyst wall.
- Heat conduction in ceramic is neglected because it is much weaker than gas convection.
- Uniform flow distribution over the cross-section of the substrate, and fully developed laminar flow in substrate channels.
- Quasi-steady state gas phase is assumed due to its short residence time and a small mass fraction of gas.
- Transient behavior is covered by solid phase.
- Chemical reactions only occur on the wall surface, and at the wall temperature, gas phase reactions are negligible compared to catalytic reactions.
- Diesel exhaust is always oxygen rich, consumption of oxygen by after treatment reactions are negligible.
- All exhaust components are treated as ideal gases.
- Reaction rate constants follow the Arrhenius form, and prohibition effects are considered.
- Analytical solution for each catalyst segment for stable and fast simulation
- DOC only change the ratio of NO_2/NO_x , but do not change the absolute concentration of NO_x .
- The wall-flow DPF is simplified as a flow-through catalyst like DOC, but with a soot layer on the wall.
- HC and CO slip from upstream DOC are considered in the DPF.
- Soot is evenly distributed on the wall.
- Pressure drop, soot filtration, and soot passive/active regeneration are treated with 0_D models.
- Two-layer approach for DPF pressure drop, “deep-bed” and “soot cake”.
- CO and CO_2 formed by the active/passive regeneration are not handled in the model.
- At low temperatures, $\text{NO}_2 + \text{CO} \rightarrow \text{NO} + \text{CO}_2$ and $\text{NO}_2 + \text{HC} \rightarrow \text{NO} + \text{H}_2\text{O} + \text{CO}_2$ are neglected in both DOC and DPF.

3.3 Heat transfer in the pipe

There are three modes of heat transfer: conduction, convection, and radiation. All of them are considered in a pipe module. The heat transfer in the pipe is then described as the conduction and radiation in the pipe, convection between pipe and ambient, as well as convection between the exhaust gas and pipe [18].

Conduction in the pipe is given as:

$$\frac{q}{A} = K \frac{dT}{dx} \quad (2.1)$$

Where q is the heat-transfer rate in W/m^2 . A is the cut of pipe area normal to the direction of heat flow. K is the thermal conductivity, and $\frac{dT}{dx}$ is the temperature gradient over the pipe length.

Radiation in the pipe is given as follows:

$$\frac{q}{A} = \epsilon \cdot \sigma \cdot (T_s - T_a)^4 \quad (2.2)$$

where q is the radiation heat flux, A is the emitting surface, ϵ is surface emissivity, σ is Stefan-Boltzmann constant, which is equal to $5.676 \cdot 10^{-8}$ in $W/m^2 \cdot K$. T_s is the surface temperature while T_a is the temperature of the ambient.

It should be noted that the heat convection involves free or natural convection and forced convection. Natural convection means that fluid motion is not driven by any external source such as a pump or a fan, but by density differences and buoyant effect due to that a fluid is heated or cooled. Forced convection means that fluid motion is produced by an external force such as a pump or a fan. Convection between pipe and ambient is a mode of natural convection. It is presented as follows:

$$\frac{q}{A} = h \cdot (T_s - T_a) \quad (2.3)$$

where q is the rate of convective heat transfer between pipe and ambient, A is the pipe outer mantle area, normal to the direction of heat flow. h is the convective heat transfer coefficient, in $W/m^2 \cdot K$, determined in equation 2.4. T_s is the surface temperature while T_a is the ambient temperature.

$$h = \frac{Nu \cdot \lambda_{air}}{L} \quad (2.4)$$

Where λ_{air} is thermal conductivity in the air, L is the characteristic length, and Nu is the Nusselt number which is determined here as:

$$Nu = \left[0.6 + \frac{\left(0.387 \cdot Ra^{\frac{1}{6}} \right)^{\frac{8}{16}}}{\left[\left(1 + \frac{0.599}{Pr} \right)^{\frac{9}{16}} \right]^{\frac{8}{27}}} \right]^2 \quad (2.5)$$

Where Ra is the Rayleigh number. It is a dimension number associated with natural convection. The Ra is defined as:

$$Ra = \frac{g \cdot B}{v \cdot \alpha} (T_s - T_a) \cdot L^3 \quad (2.6)$$

Where g is acceleration due to gravity, B is thermal expansion coefficient (it is equal to the inverse of the temperature for the ideal gas), v is kinematic viscosity, α is thermal diffusivity, T_s is the surface temperature while T_a is the ambient temperature, and L is the characteristic length.

Pr in equation 2.5 is the Prandtl number, given as:

$$Pr = \frac{C_p \cdot \mu}{\lambda_{air}} \quad (2.7)$$

Where C_p is heat capacity in air and μ is dynamic viscosity in the air.

Convection between exhaust gas and pipe is a mode of forced convection. The flow in the pipe is turbulent and the Nusselt number is determined for a straight and smooth pipe as:

$$Nu = 0.027 \cdot Re^{0.8} \cdot Pr^{\frac{1}{3}} \quad (2.8)$$

Where Re is Reynolds number. By inserting the Nusselt number from equation 2.8 to equation 2.4, the convective heat transfer coefficient between exhaust gas and pipe can be determined.

Convection between exhaust gas and pipe is then presented as follows:

$$\frac{q}{A} = h \cdot (T_s - T_a) \quad (2.9)$$

where q is the rate of convective heat transfer between gas and pipe. A is the pipe inner mantle area, normal to the direction of heat flow. h is the convective heat transfer coefficient, in $W/m^2 \cdot K$. T_s is the surface temperature while T_a is the ambient temperature.

3.4 Chemical reactions

3.4.1 DOC

Three basic reactions occurring in a DOC are:



The oxidation of carbon monoxide is simplified and explained in equation 2.10. Hydrocarbon oxidation is presented in equation 2.11. The composition of hydrocarbon in diesel exhaust is very complicated. Typical hydrocarbon distributions for diesel engine range from C1 to C40 [17]. So, the hydrocarbon oxidation is treated in a bulk way, and C1 with an H/C ratio 1.81 of the low sulfur diesel fuel is selected for this model. The lower heating value (LHV) of hydrocarbon for exotherm calculation is also assumed same as the LHV of the sulfur diesel fuel, 42900 KJ/Kg. NO oxidation is represented by equation 2.12. The reaction is assumed to be controlled by reaction kinetics and equilibrium.

Equations 2.13 to 2.15 show the reaction rates for the oxidation reactions of CO, HC and NO.

$$r_{CO} = \frac{-K_{CO} \cdot Y_{CO} \cdot Y_{O_2}^{0.5}}{G} \quad (2.13)$$

$$r_{HC} = \frac{-K_{HC} \cdot Y_{HC} \cdot Y_{O_2}}{G} \quad (2.14)$$

$$r_{NO_2} = \frac{K_{NO} \cdot Y_{NO} \cdot Y_{O_2}^{0.5} - K_{NO_2} \cdot Y_{NO_2}}{G} \quad (2.15)$$

Where K_i and Y_i are the reaction rate constant and concentration of the i^{th} species. The subscript i refers to the species. The rates constant follows the Arrhenius form:

$$K_i = A_i \cdot e^{\left(\frac{-Ea_i}{RT}\right)} \quad (2.16)$$

Where A_i is the pre-exponential factor, it is the frequency factor of molecules that will collide and be correctly oriented when they collide, and Ea_i is the activation energy of the i^{th} species [19].

The reaction rate of CO and NO are proportional to the square root of oxygen concentration. Considering together with the reversal NO_2 dissociation, the overall NO consumption rate is described by equation 2.15. The oxidation reaction of hydrocarbon is assumed to only occur on the wall surface. The reaction rate is proportional to both HC and oxygen concentrations at the wall surface. Since the change of oxygen concentration across a flow channel is small compared to the total oxygen concentration, the oxygen concentration at the wall surface is assumed to be the same as the bulk flow. The reaction rate of hydrocarbon is represented in equation 2.14.

The term G is an inhibition factor. It takes account of the inhibition effects of CO, HC, and NO on the reaction rates [20].

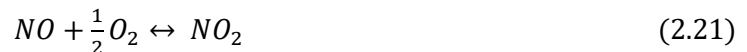
$$G = T[1 + K_1Y_{CO} + K_2Y_{HC}]^2 \cdot [1 + K_3Y_{CO}^2Y_{HC}^2] \cdot [1 + K_4Y_{NO}^{0.7}] \quad (2.17)$$

The first term of G, T, is a temperature dependence factor. The second term $[1 + K_1Y_{CO} + K_2Y_{HC}]^2$ represents the inhibition effects related to chemisorption of CO and HC. The third term $[1 + K_3Y_{CO}^2Y_{HC}^2]$ is used to fit experimental data at higher concentrations of CO and HC. Moreover, the last term $[1 + K_4Y_{NO}^{0.7}]$ represents the inhibition effects of NO on oxidation rates. Y_i is the concentration of the i^{th} species in the solid wall, and K_i is the adsorption equilibrium constants. It also follows the Arrhenius form and is given as:

$$K_i = A_i \cdot e^{\left(\frac{-Ea_i}{RT}\right)} \quad (2.18)$$

3.4.2 DPF

Chemical reactions in the DPF are formulated below:



The reaction rate expressions for the oxidation reactions of CO, HC and NO and inhibition functions are the same as for the DOC model. However, due to the much low precious metal loading of a DPF and different washcoat composition, the reaction constants can be diverse. Soot passive regeneration with NO_2 is included in the model and described by equation 2.22.

3.5 Flow-through substrate governing equations

Mass balance

The conservation of mass for the exhaust gases is:

$$\frac{\delta \rho_g}{\delta t} + \frac{\delta(\rho_g \cdot u_g)}{\delta x} = 0 \quad (2.23)$$

Due to the quasi-steady state gas phase, the first term on the left can be zero. The equation has then the following form:

$$\frac{\delta(\rho_g \cdot u_g)}{\delta x} = 0 \quad (2.24)$$

where ρ_g is the density of the gas, calculated using ideal gas law. u_g is the gas velocity, and x is the length of a sub DOC.

The conservation of species in the gas phase is:

$$OFA \cdot \frac{\delta Y_i}{\delta t} = -OFA \cdot u_g \cdot \frac{\delta Y_i}{\delta x} - GSA \cdot k_m \cdot (Y_{i,g} - Y_{i,s}) \quad (2.25)$$

Neglecting the accumulation term on the left, the species conservation in the gas phase is:

$$OFA \cdot u_g \cdot \frac{\delta Y_i}{\delta x} = GSA \cdot k_m \cdot (Y_{i,s} - Y_{i,g}) \quad (2.26)$$

Where OFA is the open fraction area, is often expressed as a percentage of the total substrate cross-section area (also known as the substrate void fraction), GSA is the specific geometric surface area defined as the total channel surface area per unit substrate volume [9]. $Y_{i,g}$ is the concentration of the i^{th} species in the gas phase, $Y_{i,s}$ is the concentration in the solid wall, and k_m is the mass transfer coefficient, which can be calculated from Sherwood number for fully developed laminar flow:

$$K_m = \frac{Sh \cdot D_i}{d_h} \quad (2.27)$$

Where Sh is the Sherwood number and depends on the geometry of the substrate, and the Reynolds number, as well as the Schmidt number. d_h is the hydraulic diameter of substrate channels, and D_i is the effective diffusion coefficient of the i^{th} species and calculated with the following equation:

$$D_i = D_{AB} \cdot D_0 \quad (2.28)$$

Where D_{AB} is called the binary gas phase diffusivity and D_0 is a factor which accounts for both the washcoat tortuosity and porosity [18].

The conservation of species in the solid phase is:

$$K_m \cdot (Y_{i,g} - Y_{i,s}) = r_i \quad (2.29)$$

The rate of transport of species from the exhaust gases to the wall must be equal to the rate of disappearance of species caused by the chemical reaction on the wall surface. Thus mass diffusion should be equal to the oxidation rates [17].

Momentum balance

The conservation of momentum in the gas phase is:

$$\frac{dP}{dx} = -\frac{d(\rho_g \cdot u_g \cdot u_g)}{dx} - \frac{F \cdot \mu \cdot u_g}{dh^2} \quad (2.30)$$

The first term on the right can be eliminated by substituting the mass conservation equation 2.24 in this formula. The equation can be rewritten as:

$$\frac{dP}{dx} = -\frac{F \cdot \mu \cdot u_g}{dh^2} \quad (2.31)$$

While considering the total length of the DOC, the pressure drop across DOC can be formulated as:

$$\begin{aligned} \frac{\Delta P}{L} &= -\frac{F \cdot \mu \cdot u_g}{dh^2} \\ \text{or } \Delta P &= \frac{F \cdot \mu \cdot u_g \cdot L}{dh^2} \end{aligned} \quad (2.32)$$

where F is the friction coefficient for a square channel which has a value of 28.454 [17], μ is the dynamic viscosity, and dh is the hydrodynamic diameter.

Energy balance

The conservation of energy in the gas-phase is:

$$OFA \cdot \frac{\delta(c_{p,g} \cdot \rho_g \cdot u_g \cdot T_g)}{\delta x} = GSA \cdot h(T_s - T_g) \quad (2.33)$$

Where $c_{p,g}$ is the gas specific heat, T_g is the gas temperature, T_s is the solid wall temperature, and h is the convective heat transfer coefficient. The latter were estimated using the Nusselt number for fully developed laminar flow. The expression is:

$$Nu = \frac{h \cdot dh}{\lambda_g} \quad (2.34)$$

Where dh is the hydraulic diameter, λ_g is the thermal conductivity of the gas.

The conservation of energy in the solid phase is expressed as follow:

$$(1 - OFA) \cdot \frac{d(C_{p,s} \cdot \rho_s \cdot T_s)}{\delta t} = GSA \cdot h \cdot (T_g - T_s) + GSA \cdot \sum q_i \quad (2.35)$$

Where $C_{p,s}$ is the substrate heat capacity, and ρ_s is the substrate density. The first term on the left side of the equation is an accumulation term. The right-hand side includes the convective heat transfer from the exhaust gas to the catalyst surface and the reaction heat produced by chemical

reactions. Heat transfer by conduction is assumed to be small compared to the convective transfer and therefore is neglected.

3.6 Boundary and initial conditions

In the DOC model, the initial conditions used to solve the differential equations described above are the exhaust temperature and species concentrations at DOC inlet. In the DPF model, the initial conditions are the temperature and species concentrations at the DOC outlet. Soot mass flow is injected from the engine while the DOC model does not handle the soot oxidation. The initial soot and ash loading are assumed to be zero in the model.

3.7 Pressure drop

The DPF pressure drop model is based on the load filter case investigated by Konstandopoulos et al. [16]. The total DPF pressure drop consists of various pressure losses components: friction in filter wall, soot cake layer, ash loading, pressure losses due to the inlet and outlet channel friction, plug friction, and the entrance and exit losses due to the contraction and expansion of the gases. An illustration of pressure drops is given in figure 3.7.

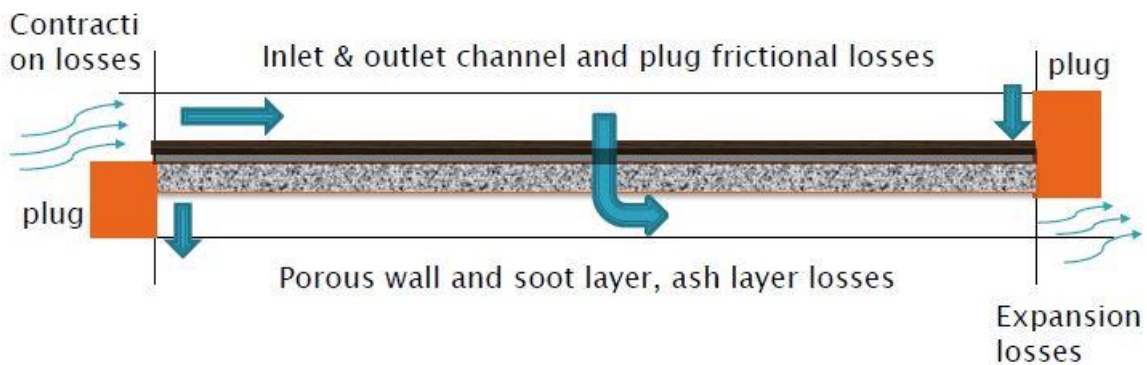


Figure 3.7 Schematic view of pressure drop locations through a channel of the DPF [21].

The expressions of different pressure loss components are summarized in table 3.1.

Table 3.1 The various pressure drop components and their formulations.

Pressure drop sources	Formulations
Filter wall	$\frac{\mu \cdot Q}{2V_{trap}} \cdot (d_h + w_{wall})^2 \cdot \frac{w_{wall}}{k_{wall} \cdot d_h}$
Soot layer	$\frac{\mu \cdot Q}{2V_{trap}} \cdot (d_h + w_{wall})^2 \cdot \frac{1}{2k_{soot}} \ln\left(\frac{d_h}{d_h - 2w_{soot}}\right)$
Friction in inlet channel	$\frac{\mu \cdot Q}{2V_{trap}} \cdot (d_h + w_{wall})^2 \cdot \frac{4FL^2}{3} \cdot \frac{1}{(d_h - 2w_{soot})^4}$
Friction In outlet channel	$\frac{\mu \cdot Q}{2V_{trap}} \cdot (d_h + w_{wall})^2 \cdot \frac{4FL^2}{3} \cdot \frac{1}{d_h^4}$
Ash layer	$\frac{\mu \cdot Q}{2V_{trap}} \cdot (d_h + w_{wall})^2 \cdot \frac{1}{2k_{ash}} \ln\left(\frac{d_h}{d_h - 2w_{ash}}\right)$

Plug	$F \cdot \frac{\mu \cdot u_g \cdot L}{d_h^2}$
Contraction and expansion	$\xi_E \cdot \frac{\rho \cdot u_g^2}{2}$

All the parameters are defined in the Notation at the beginning of the work. Here k_{wall} is the loaded filter wall permeability accounting for slip-flow correction of permeability. First, the local permeability of the filter wall is calculated by the following equation:

$$K = k_{soot,0} \cdot \frac{d_c(i,t)^2}{d_{c0}} \cdot \frac{k_u(\varepsilon(i,t))}{k_u(\varepsilon_0)} \quad (2.36)$$

Where $k_{soot,0}$ is the nominal soot layer permeability. $k_u(\varepsilon(i,t))$ is the kuwabara geometric function for sooted wall and $k_u(\varepsilon_0)$ is the kuwabara geometric function for the clean wall.

Then, it is calculated by considering slip and transitional flow effects. The effects depend on the local Knudsen, Kn number which is defined as:

$$kn = \frac{2\lambda}{d_{pore}} \quad (2.37)$$

Where λ is the mean-free-path defined by:

$$\lambda = v \cdot \sqrt{\frac{\pi MW}{2RT}} \quad (2.38)$$

The final loaded wall permeability is given as:

$$K_{wall} = SCF \cdot K \quad (2.39)$$

Where SCF is the Stokes-Cunningham Factor to correct for slip-flow effects. It is calculated by setting the local Knudsen number kn:

$$SCF = 1 + Kn \left(1.257 + 0.4e^{\frac{-1.1}{Kn}} \right) \quad (2.40)$$

k_{soot} and k_{ash} are calculated in a similar way as filter wall permeability. For details of the pressure drop calculation, see Konstandopoulos' paper: Fundamental Studies of Diesel Particulate Filters: Transient Loading, Regeneration and Aging, SAE 2000-01-1016 [16].

3.8 Numerical solver and calculation flow chart

The solver used in the model is fixed-step explicit solver using first order Euler's method [22]. It computes the value of a state at the next simulation time step by using an explicit function of the current values of both the state and the state derivate. The solver is expressed as follows:

$$x(n + 1) = x(n) + h \cdot Dx(n) \quad (2.41)$$

Where x is the state, n is the current time step, h is the step size, and Dx is the solver-dependent function that estimates the state derivative.

First order Euler's method (ode1) is the least computational complexity of the integration technique to compute the state derivatives. The simulation's accuracy and the duration depend on the step size taken by the solver. The results become more accurate with decreasing step size. So, for any given step size, the more computationally complex the solver is, the more accurate are the simulation results.

The flow chart for the model calculation is shown in figure 3.8.

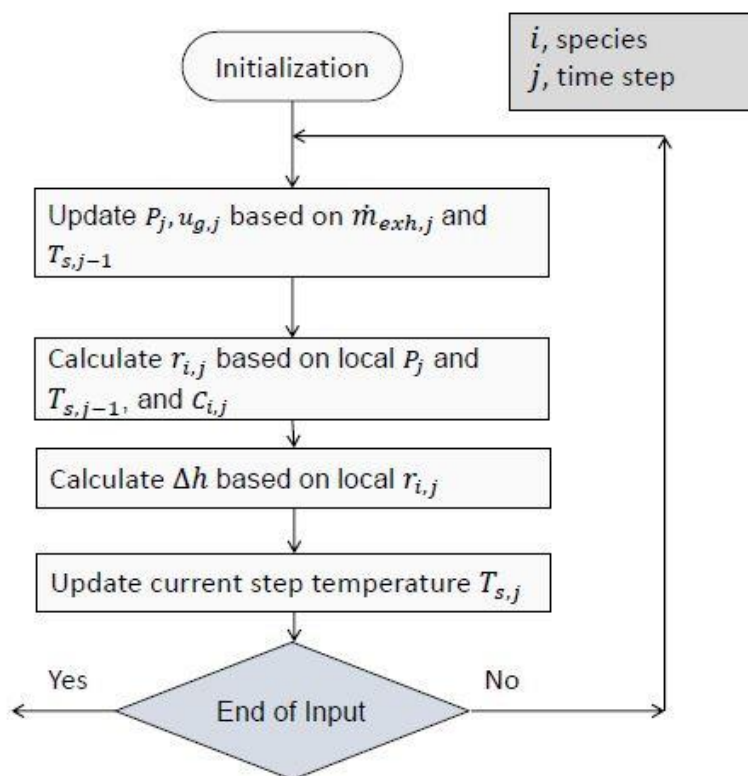


Figure 3.8 An overview of the model calculation process. Abbreviations in figure: P_j is the pressure, $u_{g,j}$ is the gas velocity, $\dot{m}_{exh,j}$ is the exhaust mass flow, $T_{s,j-1}$ is the wall temperature at the $j-1$ time step, $r_{i,j}$ is the reaction rate, $C_{i,j}$ is the species concentration and Δh is the reaction heat.

4 Calibration

In this chapter, the model calibration process is fully described. Test cycles using for the calibration and validation are presented in section 4.1. Parameters that need to be tuned for DOC and DPF model are formulated in section 4.2. The tuning process is described in section 4.3.

4.1 Preparation

Before using a catalyst model to evaluate engine emissions, the catalyst specifications of the system need to be defined in the model. These specifications are material properties, pipe and substrate geometries, substrate porosity and washcoat loading. Most of the geometric parameters are measurable, for example, pipe and substrate length, diameter and wall thickness, substrate cell density and substrate plug length. They can be physically measured. The supplier originally provides other parameters such as substrate density, porosity, mean pore size, and washcoat composition. The specific heat capacity for air and steel (Pipe is made of steel in this model), the viscosity of air, the conductivity of air, etc.... are however material properties. They have been well measured by the science/engineering societies and came from literature. In the model, they are treated as known values and are not subjected to calibration.

The parameters which need to be adjusted are especially the reaction kinetic parameters. To estimate these parameters, firstly, a test cycle together with emission measurements at turbo-out, post-DOC, and post-DPF locations for the DOC or DPF model are needed. A stage V non-road diesel engine was used as the exhaust source. The experimental input and output of temperature, pressure, and species concentrations are measured according to figure 4.1.

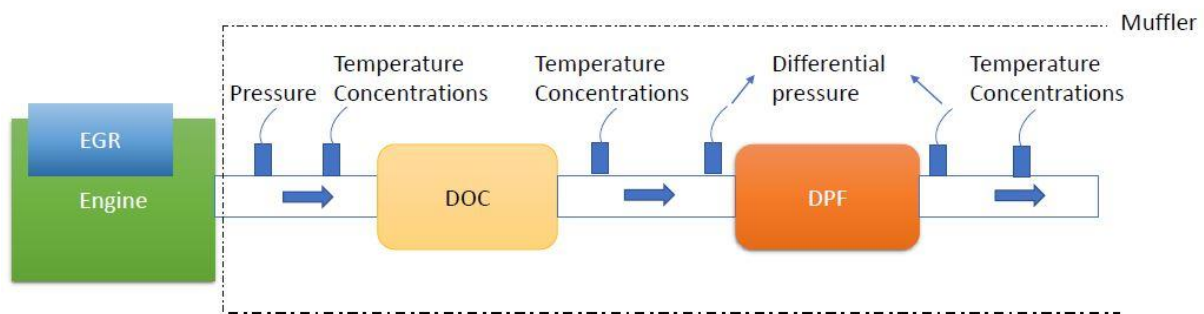


Figure 4.1 Experimental set-up

Based on the initial parameters' values and input data from the measurement, the model is implemented to obtain the simulation results. Then, the tuning of the parameters is performed for the purpose of minimizing the difference between experimental and simulation results.

A successful calibration will not only match the measured data which was used for tuning but other independent experimental data which were obtained in tests. Hence, it is necessary to perform a validation against other experiments after the calibration.

Test cycles that have been used for DOC and DPF model calibrations are called PLM (Part Load Map). PLM is a slow transient cycle of a total duration of around 26000 seconds. The temperature and mass flow were high in the beginning and going down to lower as time elapsed. Figure 4.2 shows the temperature profile and the engine speed and torque of the PLM.

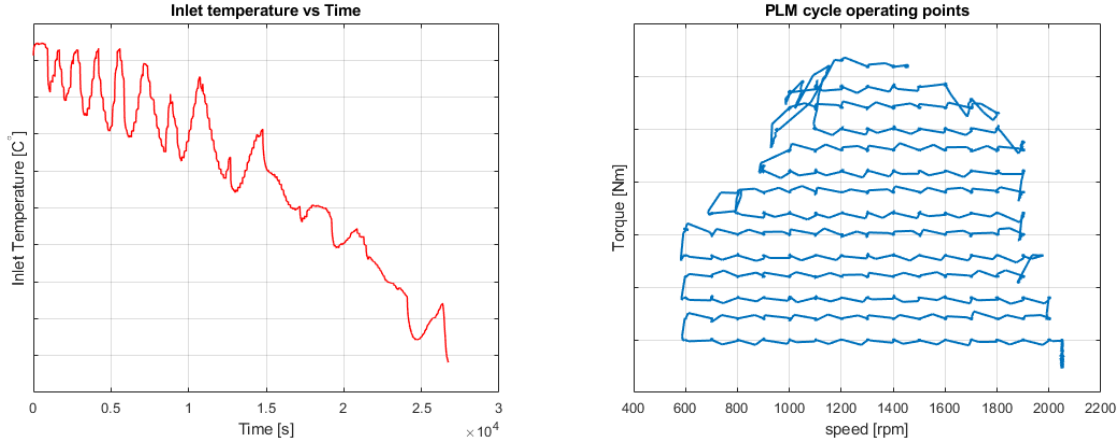


Figure 4.2 Temperature profile and engine operating points of PLM

As illustrated in figure 4.2, PLM operating points, PLM starts at high torque with high speed and then torque decreases slowly with speed varying. Finally, it stops at low torque with high speed.

Test cycles that have been used for model validations are called NRTC (Nonroad Transient Cycle). The NRTC is an authoritative test cycle for emission certification of nonroad engines [23]. It is a fast-transient cycle that the torque and speed change more frequently than PLM. The total duration is around 12000 seconds. Figure 4.3 shows the temperature profile and the engine speed and torque of the NRTC.

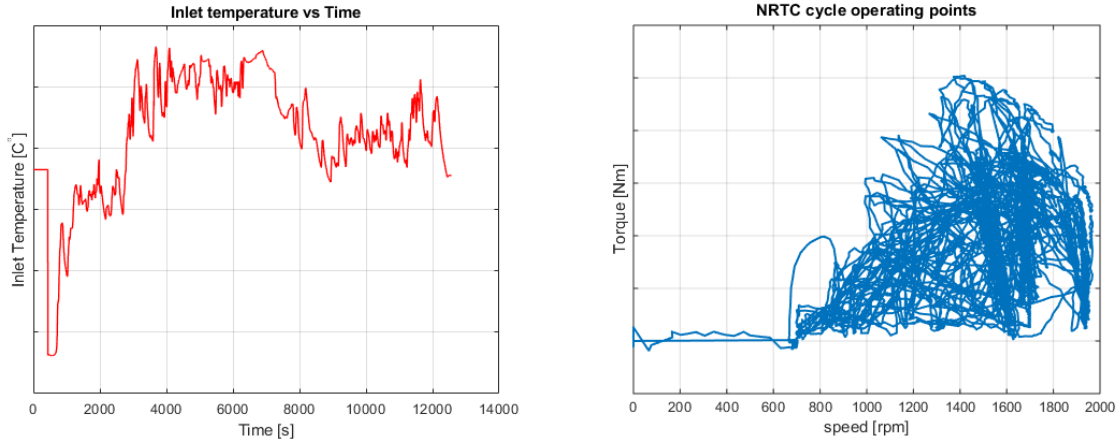


Figure 4.3 Temperature profile and engine operating points of NRTC.

As seen in figure 4.3, the transient behavior can be observed.

The calibration work was divided into two parts. First, to calibrate the DOC model and then the DPF. This has been done to avoid too many parameters that would be estimated simultaneously to save the computation time and reduce the correlation among the parameters. Finally, two individual models were linked together and without extra calibration, a validation for the combined model has been performed. Table 4.1 shows the plan of the calibration and validation of the model.

Table 4.1 Test cycles for model calibration and validation of DOC, DPF and combined DOC and DPF.

Model	Calibration	Validation
DOC	PLM	NRTC
DPF	PLM	NRTC
DOC+DPF	-	PLM+NRTC

4.2 Adjustable parameters

In this work, heat and mass transfer parameters are also tuned to complement the estimation of kinetic parameters. This section presents all the adjustable parameters of DOC and DPF model. The range of the parameters that allowed to vary during the estimation is described and the tuning order is also presented.

4.2.1 DOC model

4.2.1.1 Heat transfer parameters of DOC

The reaction rates have an exponential dependence on temperature as seen in the Arrhenius equation. This means that a big deviation of catalyst temperature can lead to the mismatch of reaction rates too. Therefore, the temperature is essential for estimation of the kinetic and mass transfer parameters. The heat transfer parameters can be estimated independently from the chemical reactions due to the concentrations of reacting species are small. The heat produced by the reaction does not affect the temperature in the same magnitude as the convective heat transfer. Thus, the heat transfer parameters were estimated before the other parameters.

The heat loss and thermal inertia (mass multiply by specific heat capacity) are both included during the estimation. The latter means how quickly and slowly the temperature increases or decreases. The heat loss term is added to the pipe which includes the heat conduction, radiation and convection between pipe and ambient, see chapter 3, section 3.3, on page 14. The heat conduction is too low compared to the convection and radiation. In the meantime, the radiation has a strong nonlinearity which is difficult to optimize (Temperature to the power of four). Therefore, convection between pipe and ambient was chosen to be tuned. Since the convection heat transfer coefficient is a function of the temperature, a scaling factor (*hpa_coef*) to the coefficient was defined to be an adjustable parameter.

The thermal inertia can be adjusted either by changing the steel pipe's specific heat capacity or the density or by changing the substrate's specific heat or the catalyst density. Increasing the density has the same effect as increasing the heat capacity because it is the product of the two variables used in the temperature model. So, the tuning parameters of the thermal inertia were selected as the specific heat capacity (C_{p_steel}) of the pipe and the mass ($mass_{cat}$) of the substrate. Table 4.2 shows the chosen heat transfer parameters and bounds which they can change during the optimization.

Table 4.2 Optimized heat transfer parameters for DOC

Optimized Parameter	Initial value	Lower limit	Upper limit
hpa_coef	1	0	Inf
C_{p_steel} [J/kg·K]	460	0	Inf
$mass_{cat}$ [kg]	2.3	0	Inf

The scaling factor for the heat transfer coefficient is one and defined as an initial value. The range is zero to infinite. The initial heat capacity and substrate mass are from heat transfer literature and catalyst configurations. They could be tuned since they might have bit variability during the manufacturing process and the range should not be too big. In this work, the lower and upper limit for the heat capacity and substrate mass were set as zero and infinity. The reason is that in the real system, there are supporting material and shell around the DOC substrate and DPF filter, the air outside DOC substrate and DPF filter is also hot and can affect the wall temperature, whereas the model does not consider these factors. Therefore, the range of the material properties would be set high to fit the experimental data better.

The parameters were scaled by dividing their current value by the scale value since the parameters have different orders of magnitude. The scale value is the default value determining from the estimation toolbox. It is defined as the next power of two greater than the current value.

All of them were tuned against the residual of outlet temperature. The residual is always defined as measured results minus simulated results.

4.2.1.2 Mass transport and kinetic parameters of DOC

Two types of the kinetic parameters were adjusted; pre-exponential multipliers (A) and activation energies (E_a) of species: NO, CO, HC, and for the inhibition factors. They were tuned together with the mass transport parameters, which were the effective diffusivities of the species. The model treats the washcoat layer as a smooth surface with zero thickness. Since the washcoat structure is very complicated to identify, thus, the simplification will influence the transport resistance due to the layer's thickness, tortuosity, and porosity. Therefore, a factor (D_0) which account for both the porosity and the tortuosity of different species was tuned with the purpose of minimizing the correlation between kinetic reaction and mass transfer. The tuning kinetic and mass transport parameters for species NO, CO and HC are summarized in table 4.3.

Table 4.3 Optimizing kinetic and mass transport parameters for DOC

Optimized Parameter	Initial value	Lower limit	Upper limit
Mass transport			
D_{0_NO} [m ² /s]	$1.8 \cdot 10^{-6}$	$1.8 \cdot 10^{-7}$	$1.8 \cdot 10^{-5}$
D_{0_HC} [m ² /s]	$3.2 \cdot 10^{-6}$	$3.2 \cdot 10^{-7}$	$3.2 \cdot 10^{-5}$
D_{0_CO} [m ² /s]	$4.2 \cdot 10^{-6}$	$4.2 \cdot 10^{-7}$	$4.2 \cdot 10^{-5}$
Kinetics			
E_{a_NO} [kJ/mol]	89.5	44.8	179
A_{NO} [1/s]	5945.6	594.6	59455.8
E_{a_HC} [kJ/mol]	95.5	47.7	191
A_{HC} [1/s]	$1.7 \cdot 10^9$	$1.7 \cdot 10^8$	$1.7 \cdot 10^{10}$
E_{a_CO} [kJ/mol]	57.7	29	115.4
A_{CO} [1/s]	63.3	6.3	633
Inhibition factors			
$A1_{CO}$ [1/s]	$2.1 \cdot 10^{-4}$	$2.1 \cdot 10^{-5}$	$2.1 \cdot 10^{-3}$
E_{a1_CO} [kJ/mol]	-8	-16	-3.9
$A2_{HC}$ [1/s]	0.24	0.02	2.4
E_{a2_HC} [kJ/mol]	-3	-6	-1.5
A_3 [1/s]	$2.4 \cdot 10^{-16}$	$2.4 \cdot 10^{-17}$	$2.4 \cdot 10^{-15}$
E_{a3} [kJ/mol]	-96.6	-193	-48.3
$A4_{NO}$ [1/s]	4.8	0.48	47.9
E_{a4_NO} [kJ/mol]	31	15.5	62

The mass transport parameters can be found in equation 2.28, in section 3.5, on page 18. The kinetic parameters are defined in equation 2.16 and 2.17 in section 3.4.1, on page 17. The initial values of the parameters were obtained from early calibration work on EATS of North America highway long-haul trucks. The bounds of the parameters were defined as follows: the pre-exponential factors (A) and scaling factors for effective diffusivities (D_0) were increased by ten times as an upper limit and reduced by 90 percent as a lower limit. The activation energies were increased double as the upper limit and cut half as the lower limit.

Looking at the inhibition factors in table 4.3, the adsorption constants for CO and HC and the adsorption constants for their interaction have negative activation energies. Generally, in the Arrhenius equation, the reaction rate will increase with increasing temperature when the activation energy is positive. The reason for using the negative activation energies is that at high temperatures, the chemisorption of CO and HC is expected to decrease with increasing temperature. The inhibition effects will therefore reduce. On the other hand, the positive activation energy of the NO adsorption

constant is due to that the inhibition effect of NO will, however, increase with increasing temperature [20].

The parameters were tuned against species concentrations residual which are NO, NO₂, HC and CO. However, the oxygen residual was not used for tuning because oxygen consumption is very minimal compared to its order of percentages since diesel engines operate with oxygen excess. It is close to the noise level of the measurement. To reduce the correlation and disturbance, oxygen residual is not considered in this work.

4.2.2 DPF model

The DPF model predicts more phenomena than the DOC, so there will be more model parameters. However, a lot of those parameters are not strongly inter-coupled and could be estimated as groups.

The temperature can be optimized independently from either chemical reactions and pressure drop as discussed in the DOC model. The soot accumulation corresponds to the pressure drop. Since the accumulation is a slow process. Hence, it can be tuned after tuning of species concentrations.

4.2.2.1 Heat transfer parameters of DPF

Similar as DOC, the tuning parameters are the scaling factor (*hpa_coef*) to the heat loss, the specific heat capacity of the pipe, while instead of substrate mass, the heat capacity of the substrate is tuned. It will give the same effect as tuning the substrate mass. Table 4.4 shows the chosen heat transfer parameters

Table 4.4 Optimized heat transfer parameters for DPF

Optimized Parameter	Initial value	Lower limit	Upper limit
<i>hpa_coef</i>	1	0	Inf
C_{p_steel} [J/kg·K]	460	0	Inf
$C_{p_catalyst}$ [J/kg·K]	750	0	Inf

4.2.2.2 Mass transport and kinetic parameters of DPF

It should be stressed that the CO concentrations are not calibrated in the DPF model. The DPF model mainly focuses on predicting NO₂ fraction in total NO_x. The model with CO oxidation is to account for CO slip from the DOC. In fact, in the DPF, there will be a certain amount of CO generated during the active and passive soot oxidation. The chemical reactions are shown in equation 4.1 and 4.2.

Active soot oxidation



Passive soot oxidation



Since the model doesn't include these two reactions, the calibration with the CO concentrations is ignored in this work. The pre-exponential multipliers(A), activation energies (E_a) and effective diffusivities of species: NO, HC and the inhibition factors were tuned as usual. The kinetic parameters for NO₂ consumption causing by soot were also estimated. Meanwhile, the PLM data was measured from a used filter, whereas the model considered initial soot loading as zero. To obtain better results, the passive and active soot regeneration rates were calibrated to regulate the thickness of the soot cake. The tuning parameters are summarized in table 4.5.

Table 4.5 Optimizing kinetic and mass transport parameters for DPF

Parameter	Initial value	Lower limit	Upper limit
Mass transport			
D_{0_NO} [m ² /s]	$1.8 \cdot 10^{-6}$	$1.8 \cdot 10^{-7}$	$1.8 \cdot 10^{-5}$
D_{0_HC} [m ² /s]	$3.2 \cdot 10^{-6}$	$3.2 \cdot 10^{-7}$	$3.2 \cdot 10^{-5}$
D_{0_CO} [m ² /s]	$4.2 \cdot 10^{-6}$	$4.2 \cdot 10^{-7}$	$4.2 \cdot 10^{-5}$
Kinetics			
E_{a_NO} [kJ/mol]	89.5	44.8	179
A_{NO} [1/s]	5945.6	594.6	59455.8
E_{a_HC} [kJ/mol]	95.5	47.7	191
A_{HC} [1/s]	$1.7 \cdot 10^9$	$1.7 \cdot 10^8$	$1.7 \cdot 10^{10}$
$E_{a_soot_NO2}$ [kJ/mol]	38	19	76
A_{soot_NO2} [1/s]	42	4.2	420
Soot regeneration			
$E_{a_soot_pas}$ [kJ/mol]	38	19	76
A_{soot_pas} [1/s]	0.01	$1 \cdot 10^{-3}$	0.1
$E_{a_soot_act}$ [kJ/mol]	125	62.5	250
A_{soot_act} [1/s]	60.9	6.1	609
Inhibition factors			
$A1_{CO}$ [1/s]	$2.1 \cdot 10^{-4}$	$2.1 \cdot 10^{-5}$	$2.1 \cdot 10^{-3}$
E_{a1_CO} [kJ/mol]	-8	-16	-3.9
$A2_{HC}$ [1/s]	0.24	0.02	2.4
E_{a2_HC} [kJ/mol]	-3	-6	-1.5
A_3 [1/s]	$2.4 \cdot 10^{-16}$	$2.4 \cdot 10^{-17}$	$2.4 \cdot 10^{-15}$
E_{a3} [kJ/mol]	-96.6	-193	-48.3
$A4_{NO}$ [1/s]	4.8	0.48	47.9
E_{a4_NO} [kJ/mol]	31	15.5	62

$E_{a_soot_NO2}$ and A_{soot_NO2} are activation energy and pre-exponential factor of soot led NO_2 consumption. Soot regeneration parameters are activation energies and pre-exponential factors of both passive and active soot regeneration, occurring in the soot layer. The rest of the parameters are similar to DOC. The initial values and bounds are the same as the DOC.

4.2.2.3 Soot accumulation and pressure drop parameters of DPF

After tuning of the species concentrations, the parameters of 0-D soot accumulation and pressure drop were estimated to calibrate the pressure drop of DPF. Since the initial soot loading is unknown, the physical properties of soot cake and wall substrate were adjusted to predict the pressure drop correctly. Table 4.6 illustrates the estimated parameters.

Table 4.6 Optimizing soot accumulation and pressure drop parameters for DPF

Parameter	Initial value	Lower limit	Upper limit
Channel			
F	28.454	24.2	32.7
ξ_E	2	0.02	200
Soot cake			
$\rho_{soot,c}$ [kg/m ³]	100	50	150
$\varepsilon_{soot,0}$	0.45	0.22	0.68
$k_{soot,0}$ [m ²]	$3.8 \cdot 10^{-14}$	$1.9 \cdot 10^{-14}$	$5.7 \cdot 10^{-14}$
SL_Th_ch [m]	$3 \cdot 10^{-6}$	$1.5 \cdot 10^{-6}$	$4.5 \cdot 10^{-6}$
$d_{pore,soot}$ [m]	$2.1 \cdot 10^{-6}$	$1 \cdot 10^{-6}$	$3.15 \cdot 10^{-6}$
Porous wall			
$\rho_{soot,w}$ [kg/m ³]	8	4	12
W_SL_Lim [g/L]	0.15	0.08	0.23
F_wall	1	0.5	1.5
$k_{wall,0}$ [m ²]	$3.21 \cdot 10^{-13}$	$1.6 \cdot 10^{-13}$	$4.8 \cdot 10^{-13}$
$d_{pore,wall}$ [m]	$1.8 \cdot 10^{-5}$	$9 \cdot 10^{-6}$	$2.7 \cdot 10^{-5}$
$\varepsilon_{wall,0}$	0.59	0.3	0.9
Ash			
ρ_{ash} [kg/m ³]	2500	1250	3750
AL_Th_ch [m]	$2.1 \cdot 10^{-7}$	$1 \cdot 10^{-7}$	$3.15 \cdot 10^{-7}$
$k_{ash,0}$ [m ²]	$3.2 \cdot 10^{-13}$	$1.6 \cdot 10^{-13}$	$4.8 \cdot 10^{-13}$
$d_{pore,ash}$ [m]	$3 \cdot 10^{-6}$	$1.5 \cdot 10^{-6}$	$4.5 \cdot 10^{-6}$
$Clean_Wall_Cake_PM_Frac$	0.75	0.38	1.1

All the parameters are defined in the Notation at the beginning of the work. In the channel, the F is the laminar flow pressure drop coefficient for a square tube. The initial value is from Konstandopoulos work [16]. For a perfect circular tube or pipe, the F is 32. The range for optimization is rather small, within $\pm 15\%$. ξ_E is the minor loss coefficient for pipe fittings, inlet, and outlet effects. Depending on the EATS hardware configurations, the range can vary quite a lot. In this

work, the minor loss coefficient is decreased by 0.01 as the lower limit and increased by 100 as the upper limit, which should be useful for the optimizer. The rest of the parameters are physical properties and adjusted within $\pm 50\%$. Since only the pressure drop data was available, the parameters were tuned against pressure drop residual.

Table 4.7 summarized total 61 parameters which have been calibrated in this work.

Table 4.7 Calibrated model parameters

Parameter type	Example	Number of parameters
Heat transfer	Scaling factor of convective heat transfer coefficient in the pipe. Heat capacity. Substrate capacity	6
Mass transfer	Scaling factor of the mass transfer coefficient	5
Chemical reaction properties	Reaction rate. Active and passive soot oxidation rate. Inhibition terms	32
Soot accumulation and pressure drop	Soot density. Soot layer thickness. Filter porosity. Filter wall permeability...	18

4.3 Parameter estimation

With determined adjustable parameters, the parameter estimation can finally be performed. The estimation method is presented in this section. The measured data is preprocessed before using it for estimation. Furthermore, a method of saving the estimation time and computer memory is also demonstrated.

4.3.1 Estimation method

The software used for tuning parameters is called MATLAB Simulink Design Optimization [24]. It uses optimization techniques to estimate model parameters. The parameters can be alternatively specified by setting lower and upper bounds. Considering the range of the parameters, in each optimization iteration, the software simulates the model with the current parameters and obtains a simulated response which tracks the measured response, it computes the error between the measured response and the simulated response. This error is error residual. It is presented in equation 4.3.

$$e(t) = y_{ref}(t) - y_{sim}(t) \quad (4.3)$$

$e(t)$ are the error residual. $y_{ref}(t)$ is the measured response and $y_{sim}(t)$ is the simulated response.

In each iteration, the optimization method minimizes the error residual by tuning the parameters progressively. The error residual can also be called the cost function or the objective function of this optimization problem. In the program, the default cost function is a sum of squared errors, which uses a least-squared approach. This cost function is selected to be used in this work. It is demonstrated in equation 4.4.

$$F(x) = \sum_{t=0}^{t=N} e(t) \cdot e(t) \quad (4.4)$$

Where N is the number of samples. $F(x)$ is the objective function. The software evaluates the cost function for a specific time interval. This interval is related to the measured response time base and the simulated response time base. The measured response time base is a series of time points which can be specified by users. The simulated response time base is from the simulated model and consists of all the time points.

The estimation is complete if the method finds a local minimum of the objective function and the estimation will converge and terminate. The optimized parameters can be obtained.

Many different optimization methods are using with the aim of minimizing the objective function and estimating the parameters. The nonlinear least squares method was used in this work. It is a recommended method for parameter estimation. It is implemented in the Matlab function `lsqnonlin`. The objective function is the residual sum of squares as the selected default cost function. It is presented in equation 4.5.

$$\min_x F(x) = \min_x (f_1(x)^2 + f_2(x)^2 + \dots + f_n(x)^2) \quad (4.5)$$

Where $F(x)$ is the sum of error squares. $f_1(x), f_2(x), \dots, f_n(x)$ represent error residual. N is the number of samples. X is the model parameters.

The basis of the `lsqnonlin` is to start at the initial parameters, approximate the objective function by a Taylor expansion and find a minimum of the objective function [25]. The `lsqnonlin` stops when the final change in the sum of squares relative to its initial value is less than the function tolerance. The function tolerance was set to 0.001 in this work. for more information of `lsqnonlin`, see for example [26].

The estimation program will also terminate when successive parameter values change by less than the parameter tolerance. This number was set to 0.001 and the iteration number was set to 100 in this work.

The algorithm of the `lsqnonlin` was chosen to be the trust-region-reflective (default). For this algorithm, the equations of the nonlinear system cannot be underdetermined, that is, the number of equations must be at least as many as the number of design variables.

4.3.2 Preprocessing measurement data

In the parameter estimation tool, the measured data can be preprocessed before using it. When the data was available, there were some outliers which deviate much from the mean values of the measured data. When estimating the parameters from data that containing unreliable outliers, the results may not be accurate. Hence, some outliers which were considered as measurement error according to test engineers and were removed or replaced before the parameter estimation.

Generally, using all measured data points to estimate model parameters is the most common way to perform parameter estimation. However, at a certain time interval, the deviation between experiment and simulation is not only due to the unknown parameters but the incorrectness of the model. These data points should therefore not be used for the estimation. Otherwise, it will cause the estimation error to the other time intervals.

As mentioned in the model assumption in chapter 3, section 3.2, on page 14, the model neglects NO_2 reduction reactions due to CO and HC at low temperature. The reactions are described in equation 4.6 and 4.7.



Figure 4.4 shows NO concentrations versus time for the measured output and inlet after 24000 seconds of PLM.

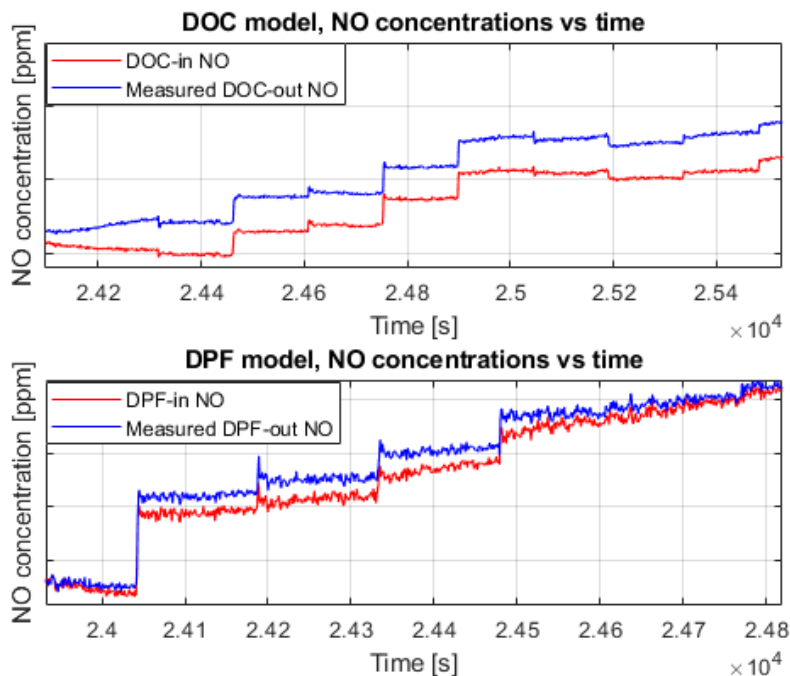


Figure 4.4 The upper chart represents the comparison of measured outlet NO concentrations and the inlet NO concentrations in DOC. The lower chart represents the comparison of measured outlet NO concentrations and the inlet NO concentrations in DPF.

Studying the plot of measured outlet concentration of NO and inlet NO concentrations of DOC and DPF models, it was found that the measured NO values are higher than the inlet concentrations after around 24000 seconds. This time region represents the low temperatures region. More generated NO can be explained by equation 4.6 and 4.7. If performing the calibration on this region, the program will force the simulated NO to be increased to match the measurement, resulting in a wrong direction of the calibration. The mismatches on the other region will occur. Therefore, ignoring the data points after 24000 seconds is preferred in this work.

On the other hand, since CO and HC will have been reacted with NO₂ according to the equations, the simulated CO and HC concentrations will also be inconsistent. However, the significant errors of CO and HC prediction are mainly due to the unknown kinetic parameters. Therefore, the estimations of CO and HC after 24000 seconds are still performed.

When specifying a start time and end time in the data preprocessing interface of the estimation toolbox, a portion of the measurement data can be extracted. This subset of data can be used in the estimation process.

4.3.3 Parallel computing

Parallel computing is used to speed up the parameter estimation. The default setting for MATLAB is only to use a single process core when performing computations. However, if having a multi-core computer, the full calculating ability is not utilized. Parallel computing distributes independent simulations to run them in parallel on several workers, on one local computer. The time used to simulate the model dominates the total estimation time. Therefore, distributing the simulations prioritizes the computational speed and reduces the estimation time. Parallel computing is available with the Nonlinear least squares, Gradient descent, and Pattern search estimation methods [27].

5 Results and discussion

In this chapter, simulation results of DOC, DPF and combined DOC and DPF model are shown by using the optimized model parameters. Further analysis of error residual is demonstrated to evaluate how successful the prediction of temperatures, pressure drop, and species concentrations can be achieved. Finally, the validations of the model are conducted, and the discussion of the validation results is also presented.

5.1 DOC calibration results

This section presents the final optimized parameters of the DOC model, obtaining from the estimation toolbox. Furthermore, the DOC simulation results are analyzed and discussed.

5.1.1 Tuning of parameters for DOC model

Table 5.1 Results of parameter tuning for DOC model

Optimized Parameter	Initial value	Optimized value	Lower limit	Upper limit
Heat transfer				
hpa_coef	1	5.4	0	Inf
C_{p_steel} [J/kg·K]	460	165.7	0	Inf
$mass_{cat}$ [kg]	2.3	3.05	0	Inf
Mass transport				
D_{0_NO} [m ² /s]	$1.8 \cdot 10^{-6}$	$1.9 \cdot 10^{-6}$	$1.8 \cdot 10^{-7}$	$1.8 \cdot 10^{-5}$
D_{0_HC} [m ² /s]	$3.2 \cdot 10^{-6}$	$3 \cdot 10^{-6}$	$3.2 \cdot 10^{-7}$	$3.2 \cdot 10^{-5}$
D_{0_CO} [m ² /s]	$4.2 \cdot 10^{-6}$	$8.9 \cdot 10^{-6}$	$4.2 \cdot 10^{-7}$	$4.2 \cdot 10^{-5}$
kinetics				
E_{a_NO} [kJ/mol]	89.5	72.4	44.8	179
A_{NO} [1/s]	5945.6	596.4	594.6	59455.8
E_{a_HC} [kJ/mol]	95.5	107	47.7	191
A_{HC} [1/s]	$1.7 \cdot 10^9$	$1.7 \cdot 10^8$	$1.7 \cdot 10^8$	$1.7 \cdot 10^{10}$
E_{a_CO} [kJ/mol]	57.7	57	29	115.4
A_{CO} [1/s]	63.3	629	6.3	633
Inhibition factors				
$A1_{CO}$ [1/s]	$2.1 \cdot 10^{-4}$	$2.2 \cdot 10^{-5}$	$2.1 \cdot 10^{-5}$	$2.1 \cdot 10^{-3}$
E_{a1_CO} [kJ/mol]	-8	-3.9	-16	-3.9
$A2_{HC}$ [1/s]	0.24	0.02	0.02	2.4
E_{a2_HC} [kJ/mol]	-3	-1.5	-6	-1.5
A_3 [1/s]	$2.4 \cdot 10^{-16}$	$2.4 \cdot 10^{-17}$	$2.4 \cdot 10^{-17}$	$2.4 \cdot 10^{-15}$
E_{a3} [kJ/mol]	-96.6	-48.3	-193	-48.3
$A4_{NO}$ [1/s]	4.8	47.9	0.48	47.9
E_{a4_NO} [kJ/mol]	31	16.2	15.5	62

The observations of the results can be summarized in the following points:

- For heat transfer parameters, the scaling factor of the convective heat transfer coefficient between pipe and ambient becomes higher after tuning. That means heat loss is increased and simulated outlet temperature decreases to agree with the measurement. Meanwhile, the thermal mass and heat capacity are also tuned to make the simulated temperature follow the measurement better.
- For mass transport and kinetic parameters, the scaling factors of the effective diffusivities for the species are tuned to reduce the influence of transport resistance to the reaction rates. The pre-exponential factors differ significantly comparing to the initial values as marked in bold font. They almost reach their maximum/minimum limits, while the adjusting of activation energies is relatively small. The tuning of the kinetic parameters shows that the reaction rates of NO and HC have been decreased, while the reaction rate of CO has been increased to agree with the measurement data.
- The inhibition mechanism is tuned to a large extent to meet the measurement since almost all of the parameters have reached their maximum/minimum limits. The reason why the tuning becomes such large can be the NO formation at low temperature is neglected in the model. To compensate this, the inhibition effects are tuned substantially.

Based on the calibrated parameters, the exhaust gas temperature and the species concentrations are simulated again to evaluate how accurate the model performs.

5.1.2 Temperature for DOC

Figure 5.1 shows the comparison of measured and simulated outlet temperature after the calibration. There is a good fit in general. To see the result clearly, a zoom-in look of the temperature and the comparison between before and after calibration is shown in figure 5.2. The rest of the zoom-in and comparison plots can be found in the Appendix.

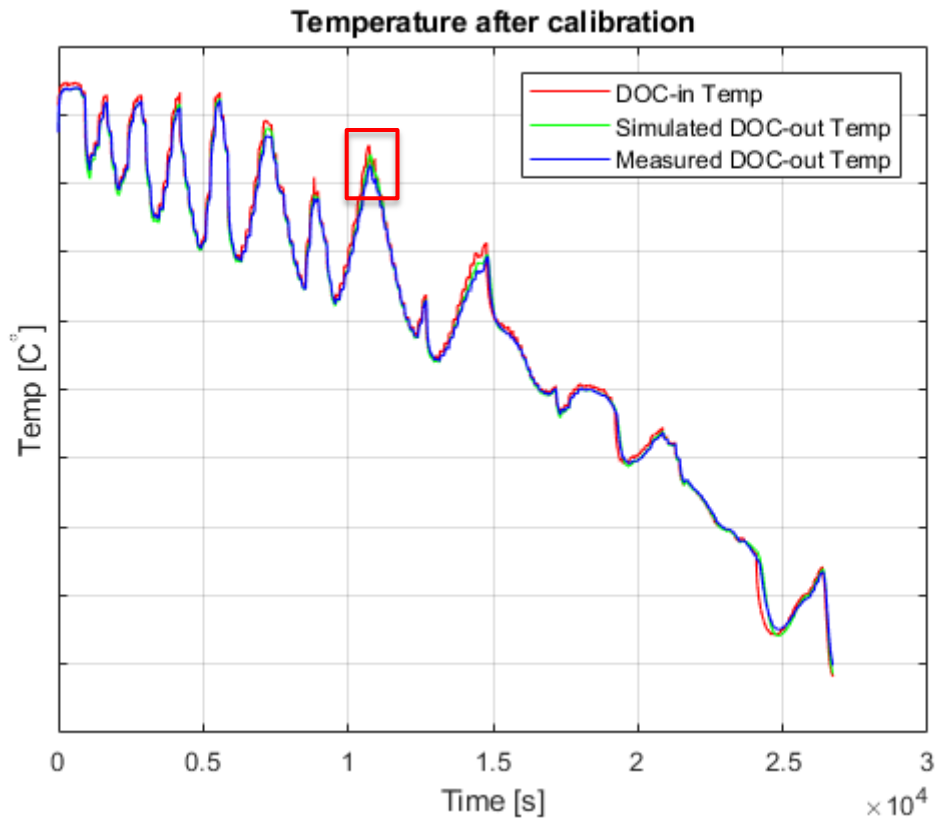


Figure 5.1 The measured (blue line) and simulated (green line) outlet temperature for all time points, together with the DOC inlet temperature (red line). The marked region is a zoom-in look which is shown in figure 5.2.

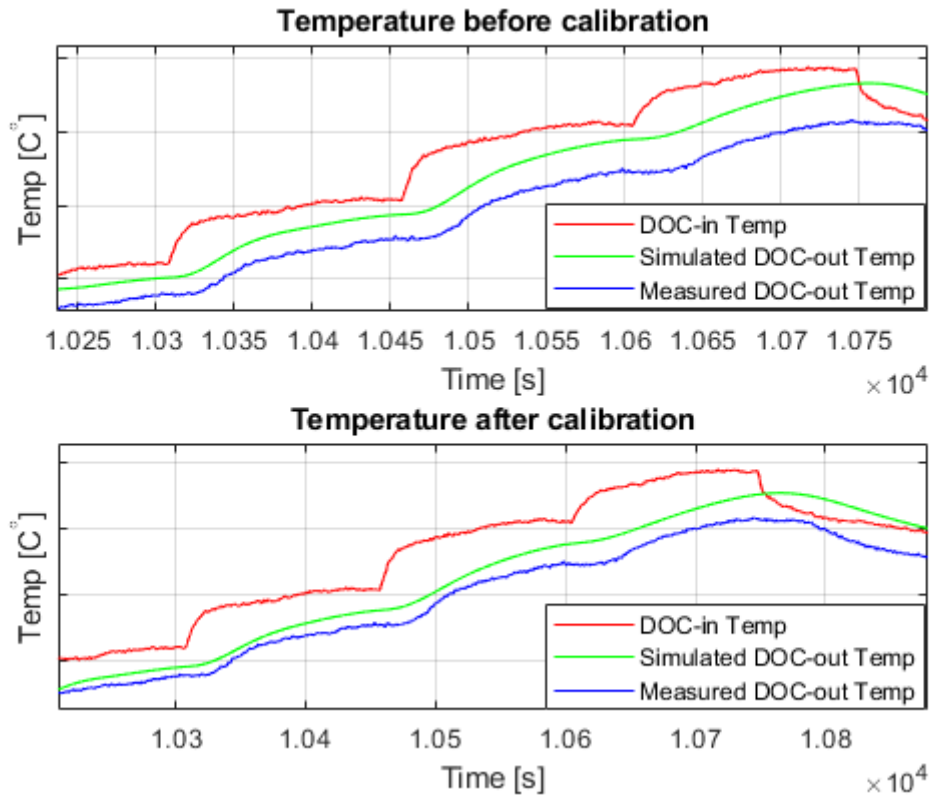


Figure 5.2 A zoom-in look of the temperature. The upper chart represents the outlet temperature before calibration, and the lower chart shows the temperature after the calibration.

It can be found in figure 5.2 where the simulated temperature follows the measurement better. To further analyze the result, a residual plot after the calibration is shown in figure 5.3. The exhaust mass flow versus time is also plotted to investigate the relationship between temperature and mass flow. The residual is defined as the difference between the measurement and simulation, according to the equation 4.3 in chapter 4, section 4.3, on page 31.

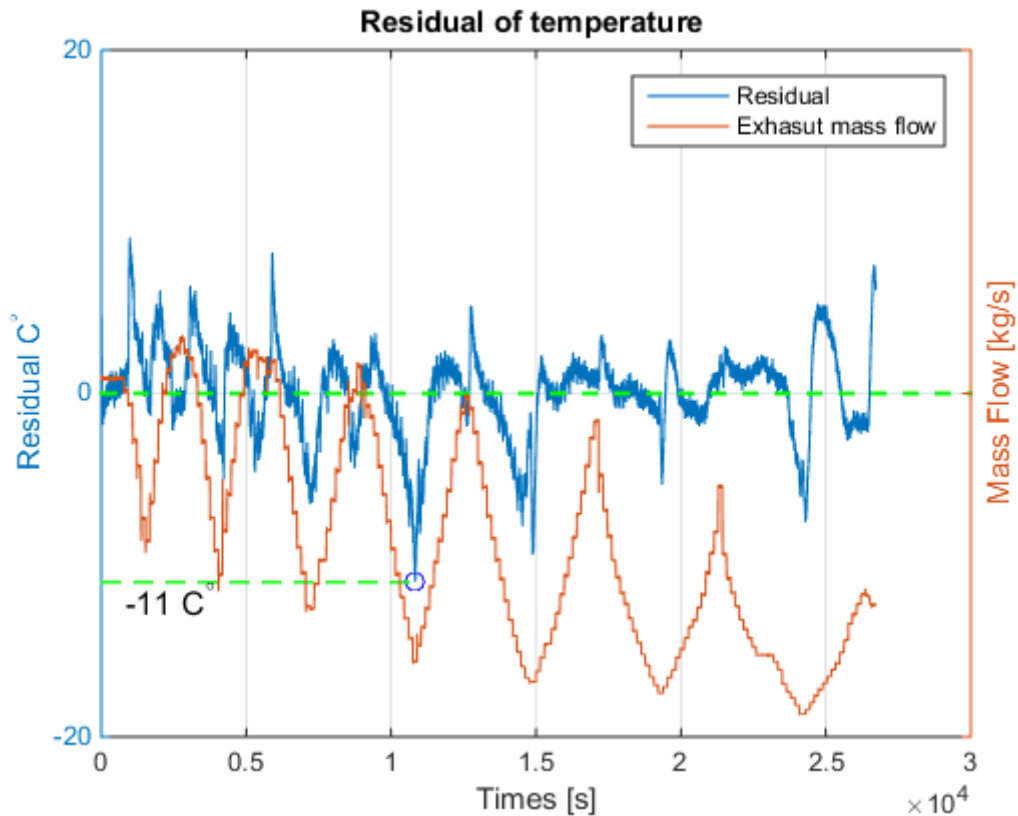


Figure 5.3 The residual (blue line) represents the difference between the measured and simulated outlet temperature. The maximum temperature deviation is 11°C. Meanwhile, the plot is compared with the exhaust mass flow (red line). The largest errors can be found at low mass flow.

As seen in figure 5.3, the errors can be observed either at very high mass flow or at very low mass flow. The residual tends to follow a pattern of the mass flow. This indicates that the temperature has a strong dependency on the mass flow. It should be stressed that the convective heat transfer in the pipe and the catalyst wall is closely connected to the mass flow. Therefore, the mass flow is an essential factor which can influence the outlet temperature. With only a scaling factor of the heat transfer coefficient by convection between pipe and ambient and two thermal inertia parameters to tune, a perfect fit can be difficult to achieve. Either a scaling factor of the convective heat transfer coefficient in the catalyst wall or parameters that correspond to the mass flow are recommended to be defined and optimized in the future calibration.

On the other hand, the reaction heat can also affect the temperature since the temperature tuning was performed before the reaction kinetics. However, as mentioned before, it probably not apparent since the species concentrations are so small. The increase in temperature due to the exothermic chemical reaction is zero assuming perfectly isolated heat transfer. This is called the adiabatic temperature rise [28]. Equation 5.1 shows the temperature rise formula.

$$\Delta T = \frac{\Delta H}{C_{p,g}} \quad (5.1)$$

Where ΔT is the adiabatic temperature rise (K), ΔH is the heat release (J/kg) and $C_{p,g}$ is the exhaust gas heat capacity (J/kg/K).

For DOC model, ΔT is calculated with equation 5.1 and the result is around 0.14 K. So, the reaction heat has a very small influence on the outlet temperature which can be neglected.

Another possible reason is that the heat conduction in the solid phase is neglected in the model, as mentioned in the model assumption, section 3.2, on page 14. However, the effect of the heat conduction had been proved to be important on the wall temperature [29]. Therefore, it is recommended to be added into the model in the future. Furthermore, the inlet pipe in the model is assumed to be straight, whereas the inlet pipe in the real aftertreatment system has 90 degrees bend. The bending will have an impact of the heat loss calculation in the pipe module since the Nusselt number is determined assuming a straight pipe.

5.1.3 CO concentrations for DOC

The comparison of measured and simulated CO concentrations after the calibration is shown in figure 5.4. For clarity, a zoom-in plot of the CO concentrations and the comparison between before and after calibration are presented in figure 5.5.

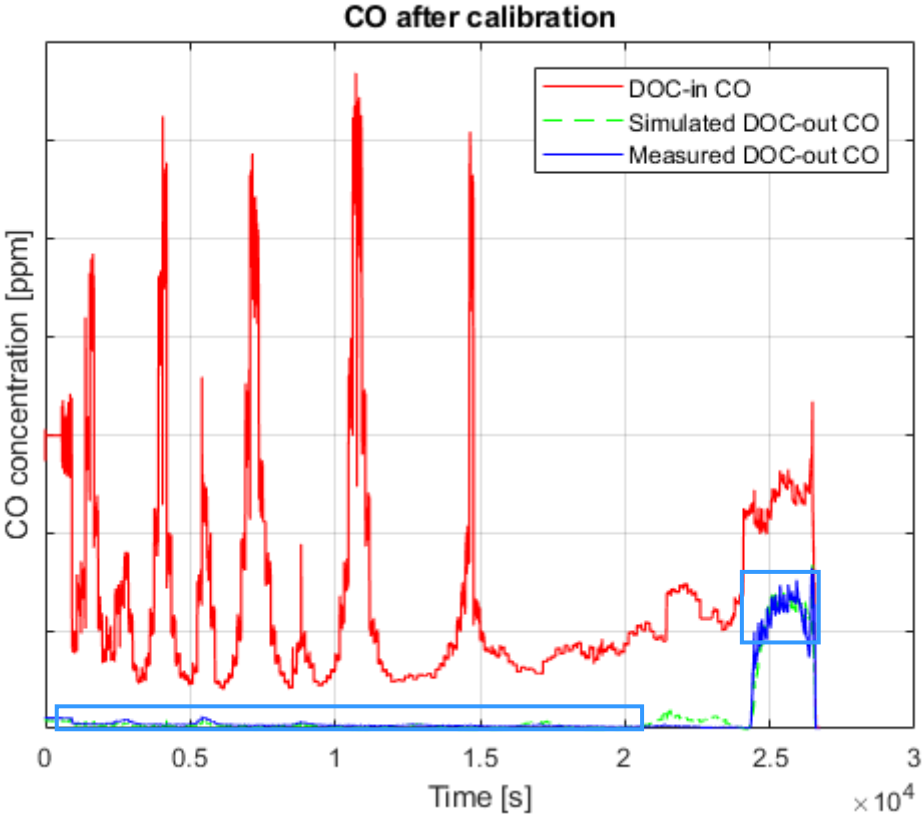


Figure 5.4 In the figure, there are measured CO concentrations (blue line), simulated CO concentrations (green line), and CO inlet concentration (red line). The marked region is a zoom-in look which is shown in figure 5.5.

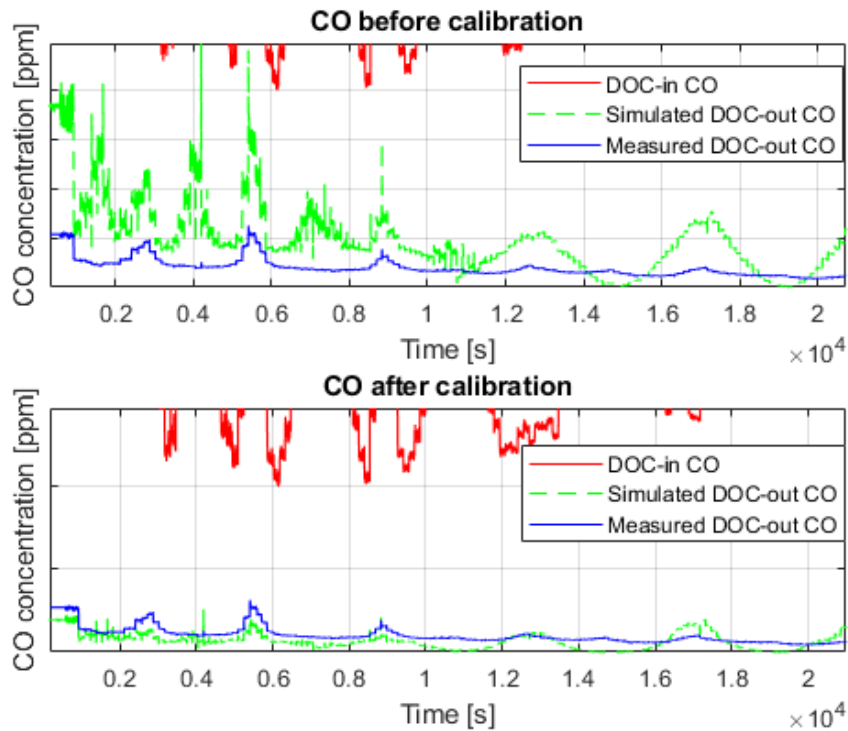


Figure 5.5 (a) A zoom in of the CO concentrations at $1 - 2 \cdot 10^4$ s. In the lower chart, the difference between measured and simulated CO concentrations is lower, proving an improvement after the calibration.

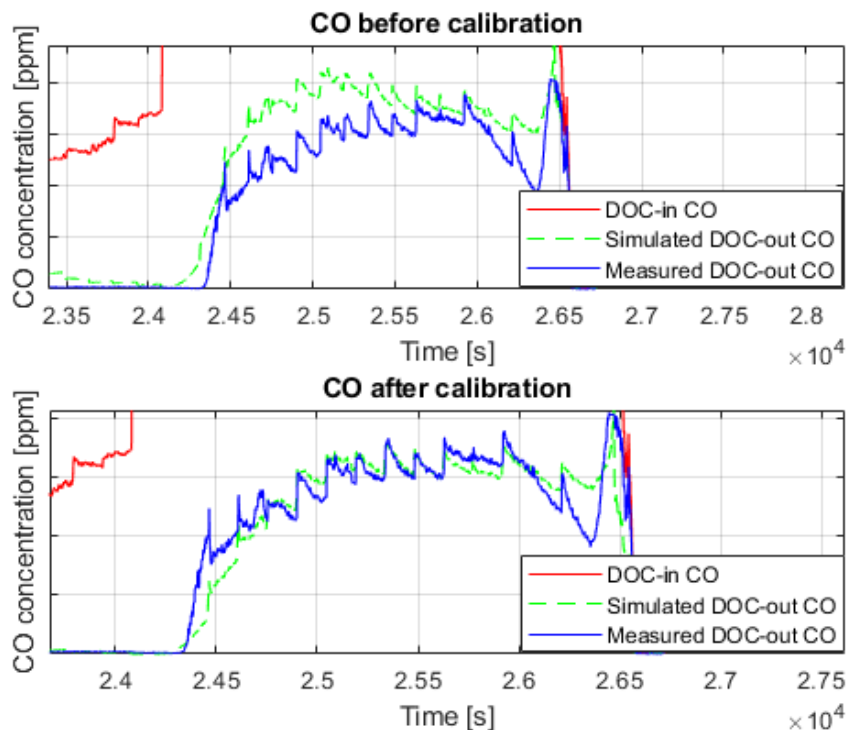


Figure 5.5 (b) A zoom in of the CO concentrations at the last part of the test cycle, corresponding to the lower temperature region. The calibration gives a lower difference between the measured and simulated CO concentrations, as shown in the lower chart comparing to the upper chart.

According to the comparison in figure 5.5, the agreement looks much better after the calibration. The CO reaction rate had been tuned to increase to fit the measurement according to the result table 5.1. It should be noted that there are NO₂ reduction reactions due to CO and HC at low temperature and there would be an extra CO consumption. However, the model neglects them. To compensate the model simplification, the reaction rate of CO in the model would be tuned to increase.

Another important thing is found at the beginning of the PLM cycle (first $1 \cdot 10^4$ seconds and the temperature is between 400°C and 500°C). The measured CO is not zero at high temperature. This phenomenon is called CO slip. The flow distribution in the DOC is nonuniform. Figure 5.6 shows a CFD simulation of the flow velocity in the DOC inlet.

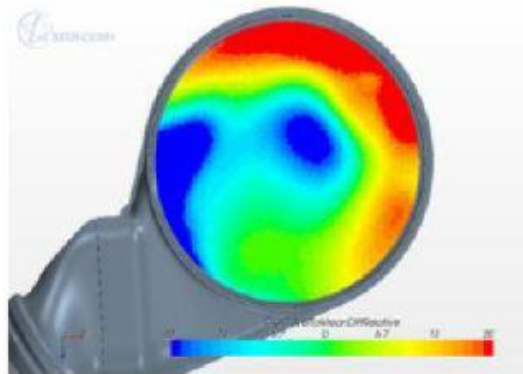


Figure 5.6 Result of a CFD simulation of the flow velocity in the DOC inlet pipe. Red represents high velocity, and blue represents the low velocity than the average. According to the figure, the flow distribution is not even.

The uneven flow distribution contributes a temperature and a velocity gradient. It could happen that CO would not be fully oxidized at high temperature. A previous thesis report about DOC model calibration has mentioned that the model did not capture the CO slip since the CO conversion was 100% at high temperature [30]. Fortunately, the model used in this thesis successfully captures the CO slip. The reason can depend on that the model considers the influence of transport resistance to the reaction rates. Therefore, the parameter D_{0_CO} , the scaling factor of the effective diffusivities for washcoat had been tuned to improve the reaction rate, as seen in the result table 5.1. To further investigate the mismatches, a residual plot together with the mass flow is shown in figure 5.7.

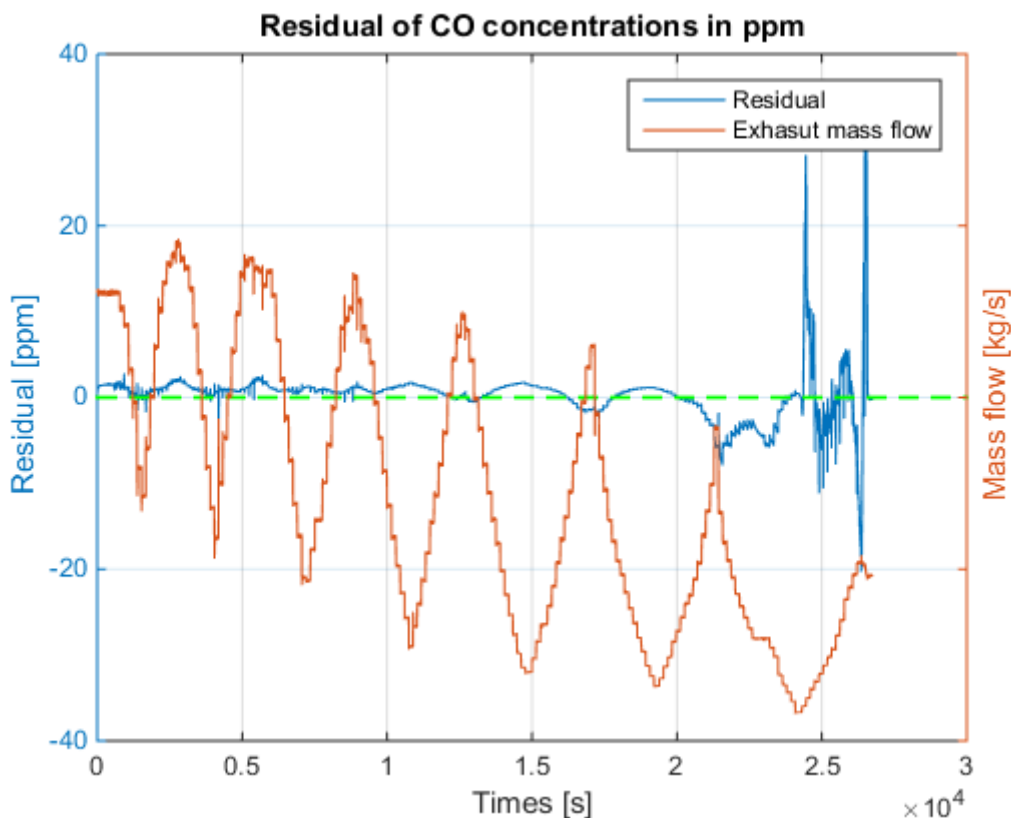


Figure 5.7 The residual (blue line) represents the difference between the measured and simulated CO concentrations. The maximum error is around 30 ppm. The residual is then compared with the mass flow (red line) and the biggest error can be found at the end of the test cycle in the lower temperature range.

From the figure 5.7, the error is large at the end of cycle where the temperature and the mass flow are low. Although the parameters have been optimized to give a best fit, the error still exists, and it can depend on many factors.

Firstly, one of the main reasons is the residual weighting. The molar fractions of NO, NO₂, CO, and HC at both catalyst inlet and outlet are different at some engine operating points. They can influence the residual sum square during the optimization. Therefore, the residual of the different species needs to be weighted to equalize the residual sum square. However, this work is not performed in this paper.

Secondly, the mismatch can depend on the high correlation among the estimated parameters. When there are too many parameters which deviate from the actual values, are estimated at the same time, the correlation among parameters presents. This can influence the accuracy of the parameter estimation.

Thirdly, from the table 5.1, nearly all the parameters of the inhibition factors and some of the kinetic parameters have reached their maximum/minimum limits. This means that further optimization of these parameters beyond the range which defined in this paper can probably improve the result. Furthermore, the rate equations have a strong nonlinearity themselves which make the estimation toolbox challenging to achieve a perfect agreement.

Finally, the uneven flow distribution can also affect the concentrations. A temperature and a velocity gradient will make the values of Reynolds number different in the channels, which results in variance in Sherwood number and diffusion coefficients, which eventually can affect the kinetics.

5.1.4 HC concentrations for DOC

The comparison of measured and simulated HC concentrations after the calibration is illustrated in figure 5.8. The zoom-in plots of the HC concentrations with the comparison between before and after calibration are presented in figure 5.9. The entire simulation result before the calibration can be found in the appendix.

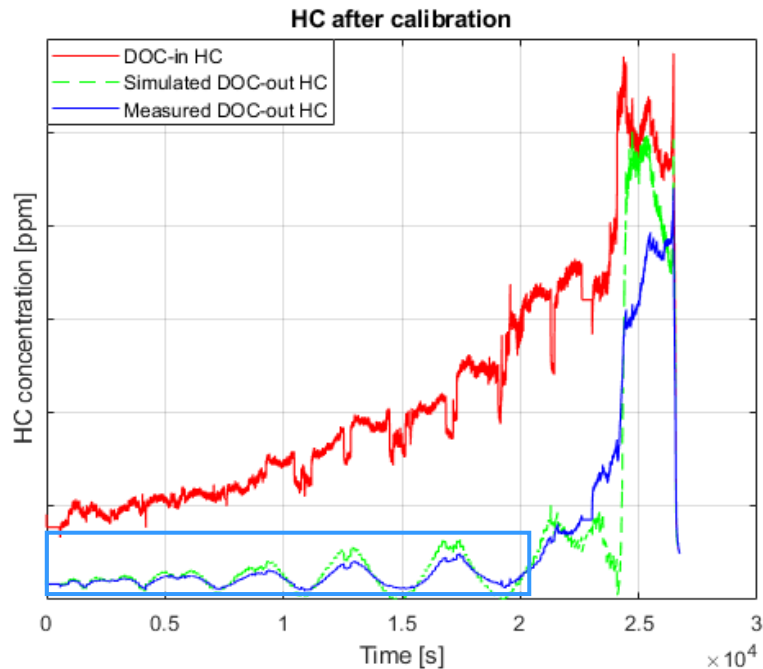


Figure 5.8 The blue line represents the measured HC outlet concentrations, and the green line represents the simulated HC outlet concentrations, as well as the HC inlet concentration (red line). The marked region is a zoom-in look which is shown in figure 5.9.

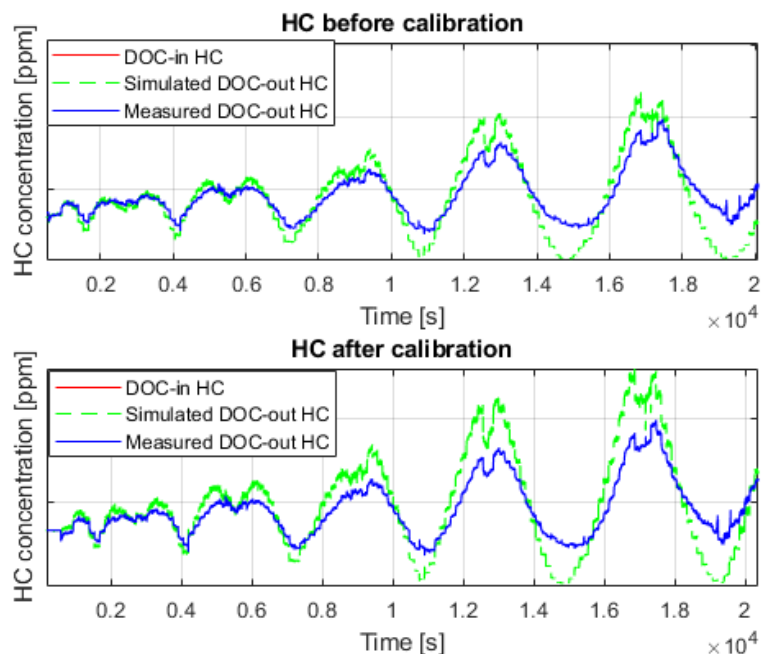


Figure 5.9 A zoom in of the HC concentrations at $1 - 2 \cdot 10^4$ s

In figure 5.8, the biggest deviation can be observed at the end of the cycle. According to the figure 5.9, the fit is good at high temperature but not be improved after the calibration. At high temperature, the measurement HC concentrations should be zero since the temperature is high enough to oxidize all hydrocarbon. However, a small part of HC concentrations is shown here which should be regarded as measurement error. The error then influences the parameter estimation on the low temperature region of the PLM cycle. A residual plot together with temperature versus time is illustrated in figure 5.10.

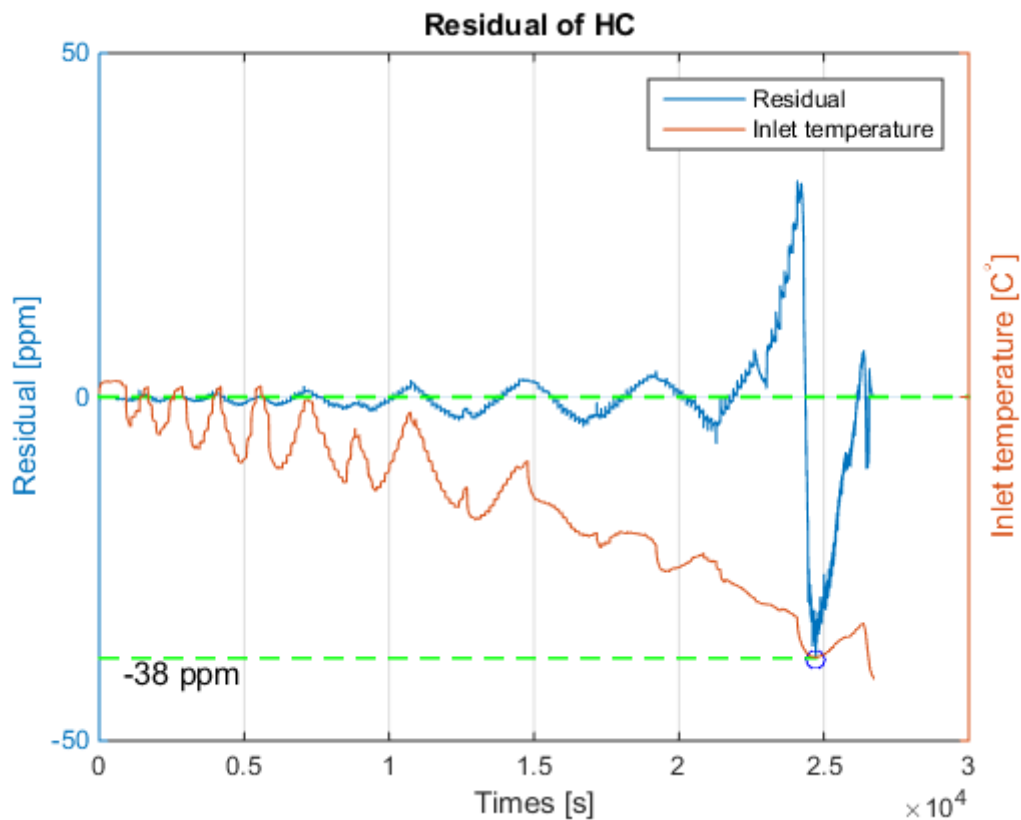


Figure 5.10 Residual of HC. The residual (blue line) represents the difference between the measured and simulated HC concentrations. The maximum error is around 38 ppm. The residual is then compared with the inlet temperature (red line), and the biggest error can be found at the end of the test cycle in the lower temperature range.

The measurement error can explain the residual at high temperature and the factors that have been discussed for CO. Besides, the HC is treated in a bulk way and represented as $\text{CH}_{1.8}$ in the model, but in fact, the composition of HC is very involved with different mass transport properties. This can influence the accuracy of the HC oxidation as well. Finally, as mentioned before, NO_2 reduction reactions at low temperature are ignored in the model. This should also be the reason for the large error at low temperature.

5.1.5 NO concentrations for DOC

The comparison of measured and simulated NO concentrations after the calibration is shown in figure 5.11. The zoom-in plots of the NO concentrations with the comparison between before and after calibration are presented in the appendix.

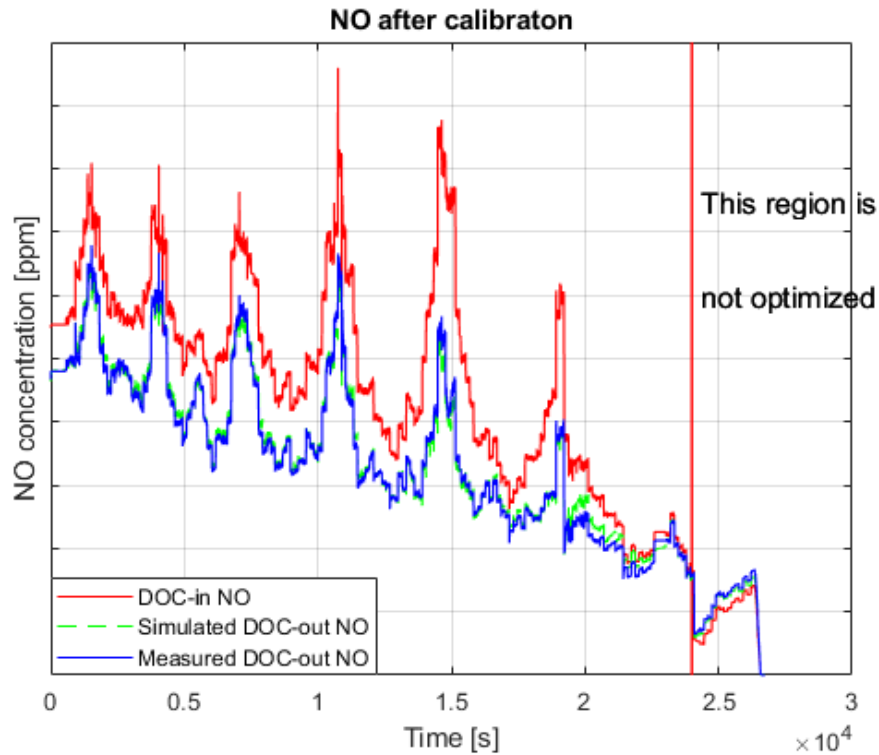


Figure 5.11 The blue line represents the measured NO outlet concentrations, and the green line represents the simulated NO outlet concentrations, as well as the NO inlet concentration (red line).

As seen in figure 5.11, the agreement of the outlet NO is quite good after the calibration. The NO residual plot, together with the temperatures is presented in figure 5.12. For clarity, a zoom-in plot at first 5000 seconds is shown in figure 5.13.

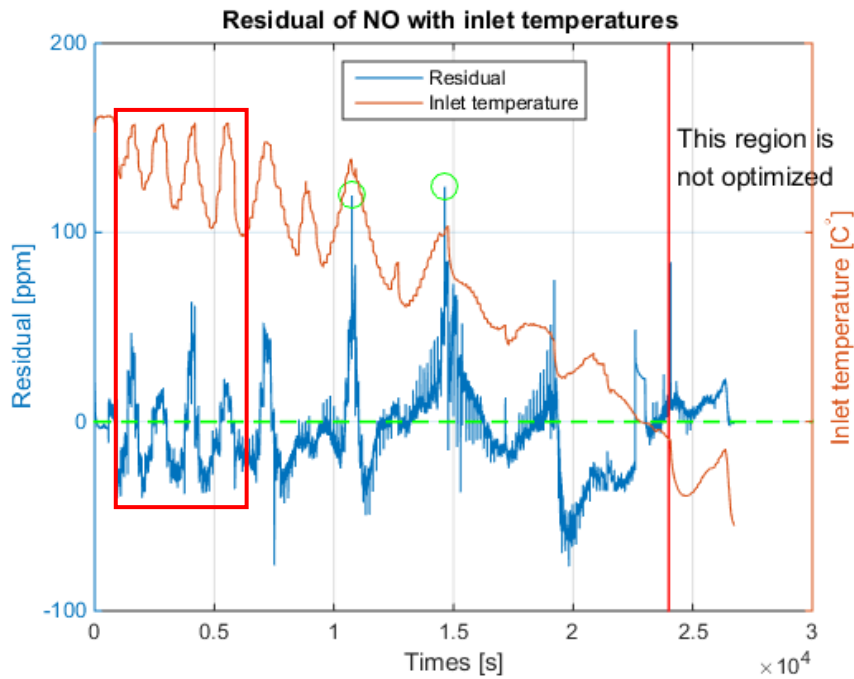


Figure 5.12 Residual of NO. The residual (blue line) represents the difference between the measured and simulated NO concentrations. It is then compared with the inlet temperature (red line). A zoom-in look at first 5000 seconds is illustrated in figure 5.13.

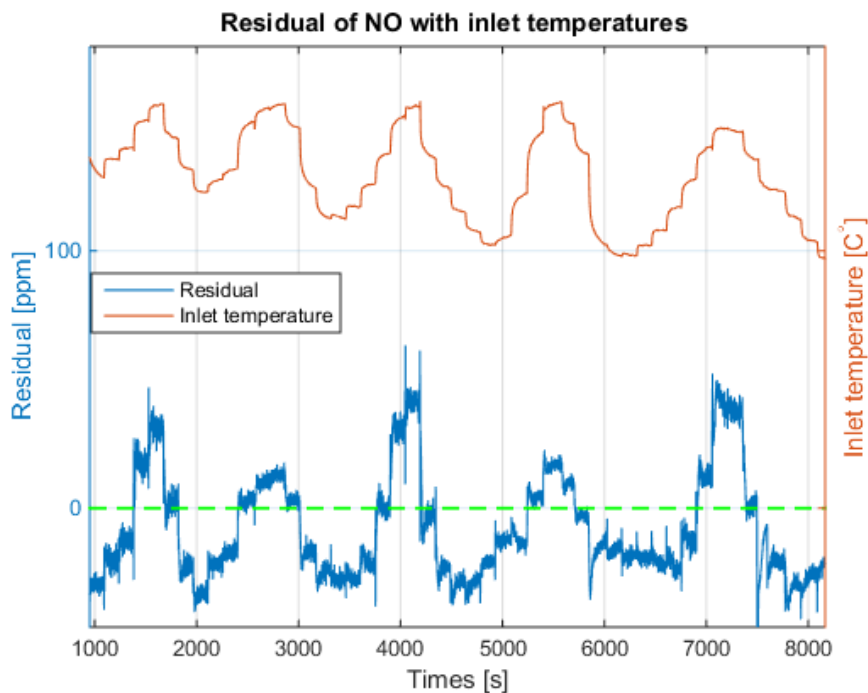


Figure 5.13 Zoom-in plots of the NO residuals

From the figure 5.12, two biggest errors are observed at around 11000 and 15000 seconds when the temperature is switching. In the figure 5.13, the residual follows the path of the temperature. The residual increases with temperature increasing or decreasing. If comparing these two errors with the residual of temperature at the same time points in figure 5.3, on page 39, it will be found that when the residual of temperature becomes larger, the NO error becomes more substantial as well.

Consequently, NO prediction has a strong dependence on the temperature. So, the most efficient way to reduce the NO prediction errors is to improve the temperature prediction.

Furthermore, residual weighting, the correlation among the parameters, and nonlinearity, as well as complexity of the chemical reactions, can all be the reasons why deviation occurs.

5.2 DOC model validation

In this section, the validation results are presented. The DOC model used optimized parameters was validated by running the NRTC. The discussion of the validation results is also added.

5.2.1 DOC temperature validation

Figure 5.14 and 5.15 show the validation result of the temperature. The residual plot is presented in the appendix.

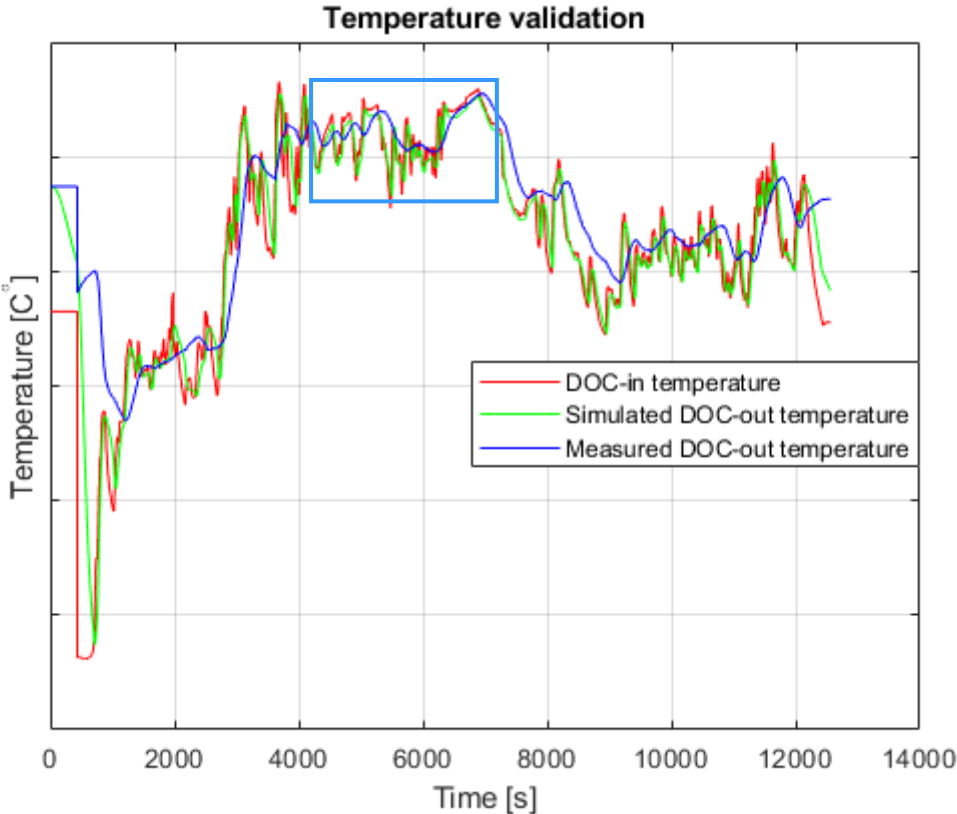


Figure 5.14 Measured (blue line) and simulated (green line) outlet temperature and together with inlet temperature (red line). The marked region is a zoom-in look which is shown in figure 5.15

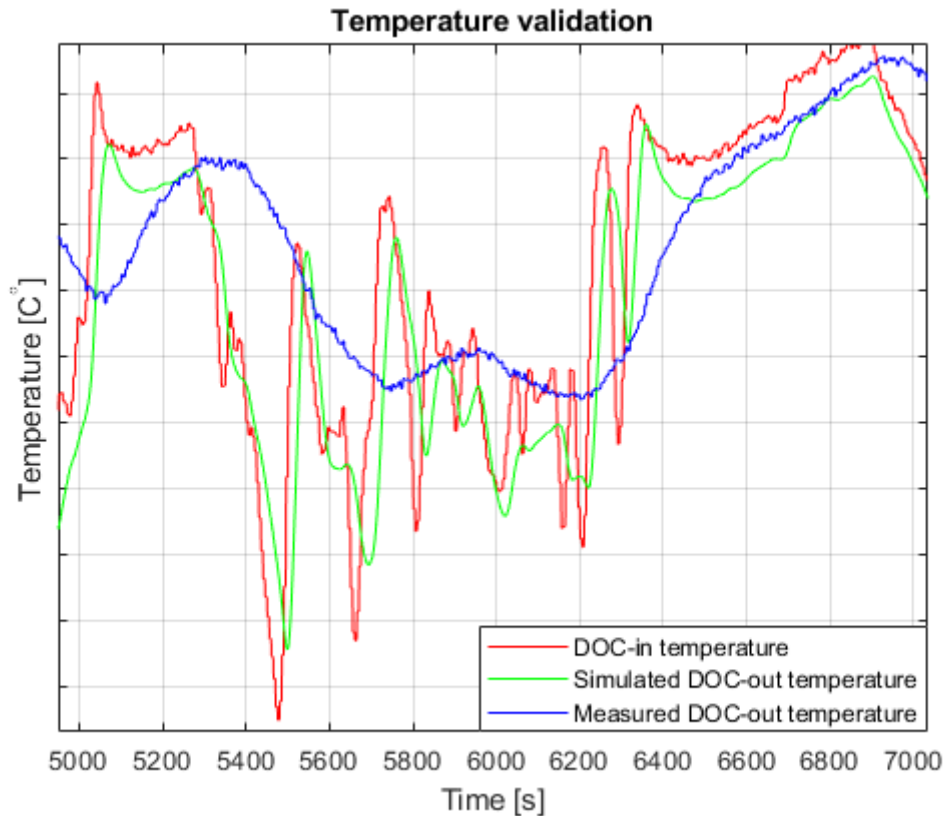


Figure 5.15 A zoom in on the temperature between 5000 and 7000 s.

From the figure 5.14 and 5.15, the fit is quite poor. Firstly, it can be observed in the beginning. Probably this is caused due to the temperature measured from the previous experiment was very hot which result in a big temperature deviation at the first 1000 seconds. This temperature error will simultaneously lead to the errors of simulated species concentrations. Therefore, all the validation results from the first 1000 seconds are ignored. Then the simulated temperature follows the inlet temperature very closely, indicating that the DOC thermal inertia is not high enough. This could be expected, since the NRTC has a strong transient behavior while the PLM is more like a steady state test cycle. Therefore, the calibrated thermal inertia maybe inconsistent with the validation of the NRTC.

5.2.2 CO concentrations of DOC validation

Figure 5.16 and 5.17 show the CO validation result.

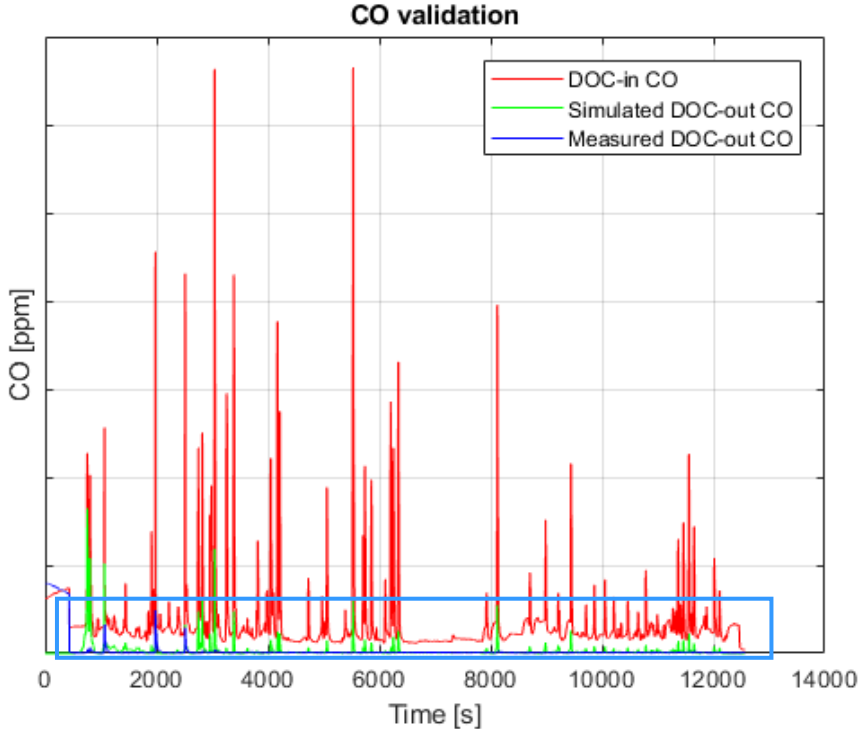


Figure 5.16 Simulated (green line) and measured (blue line) outlet concentrations of CO, and together with inlet CO concentrations (red line). The marked region is a zoom-in look which is shown in figure 5.17.

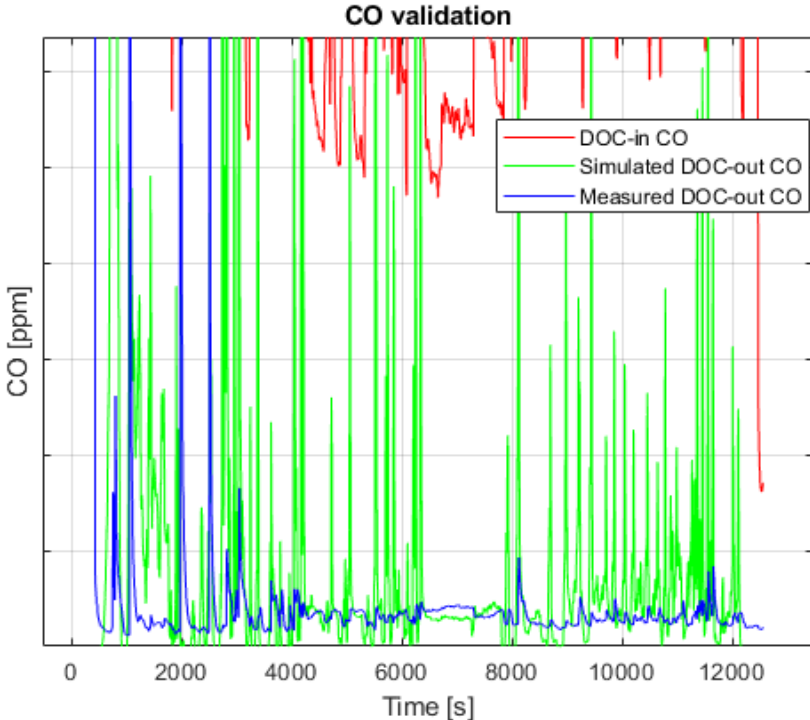


Figure 5.17 A zoom in of the CO concentrations between 1 and 12000 s.

As observed from the above figures, there are many spikes in the inlet CO concentrations. CO spikes can occur at transients such as accelerations from diesel engines. The simulated outputs almost follow the trend of the inlet CO, including several spikes as well. The incorrect temperature prediction can be one reason. The discrepancy between the measurement and simulation can be another reason, for example, the axial dispersion in the real system. The non-uniform inlet exhaust gas flow can also cause uneven temperature distribution, which results in the wrong conversion. Moreover, the incorrect kinetic parameters and mass transport parameters can also be the reason for the errors since they have been estimated using a steady state cycle. Further adjusting of both kinetic and mass transfer parameters against the transient cycle is needed and better modeling of axial dispersion is also suggested.

5.2.3 HC concentrations of DOC validation

Figure 5.18 shows the validation result of HC.

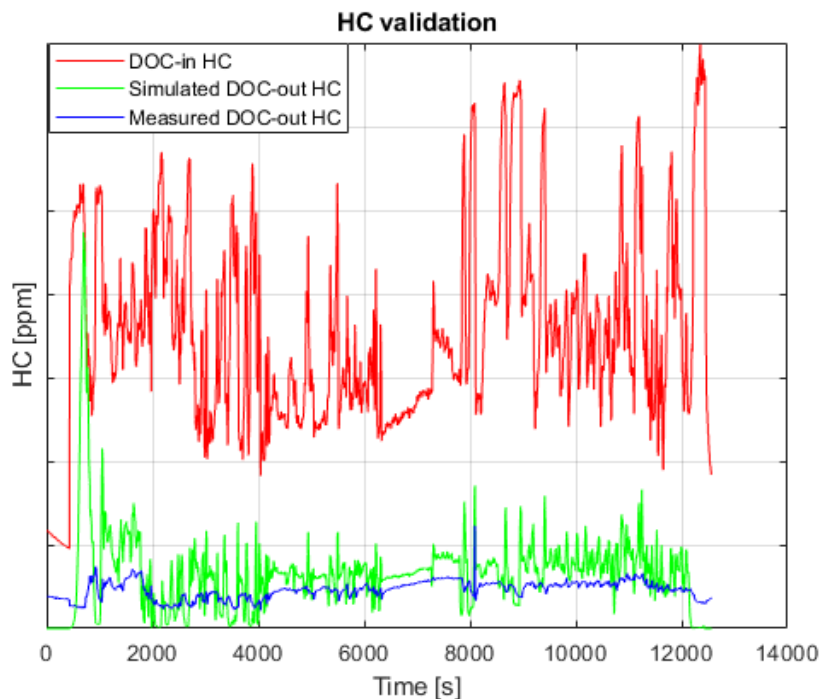


Figure 5.18 Simulated (green line) and measured (blue line) outlet concentrations of HC, and together with inlet HC concentrations (red line).

As seen in figure 5.18, the fit is quite ok. Nevertheless, as mentioned before, the measurement HC concentrations should be zero at high temperature. Here the measured HC is not zero which is regarded as the measurement error. The maximum error is however very low. Looking at the table of the European emissions standards for diesel engines in chapter 1, introduction, on page 2, the emission standard for HC is 0.19 g/kWh. How much is for example 10 ppm in g/kWh? Equation 5.2 and 5.3 show this conversion:

$$Power = \frac{Torque \cdot Speed (RPM) \cdot 2\pi}{60} \cdot 10^{-3} \quad [KW] \quad (5.2)$$

$$HC(ppm) \cdot \frac{M_{HC}}{M_{exhaust}} \cdot \frac{m_{exhaust}}{Power} \cdot 3.6 \cdot 10^6 \quad \left[\frac{g}{kWh} \right] \quad (5.3)$$

Where, M_{HC} is the molar mass of HC in g/mol, $M_{exhaust}$ is the molar mass of the exhaust gas which is 29 g/mol. $m_{exhaust}$ is the mass flow in kg/s.

Choosing an engine operating point when the simulated outlet HC is around 10 ppm, the HC concentration is in 0.023 g/kWh. For an industrial perspective, the error is so low that it can be acceptable.

5.2.4 NO concentrations of DOC validation

Figure 5.19 and 5.20 show the NO validation result. Since it is quite transient and difficult to interpret the simulated errors, the residual plot is shown in figure 5.21.

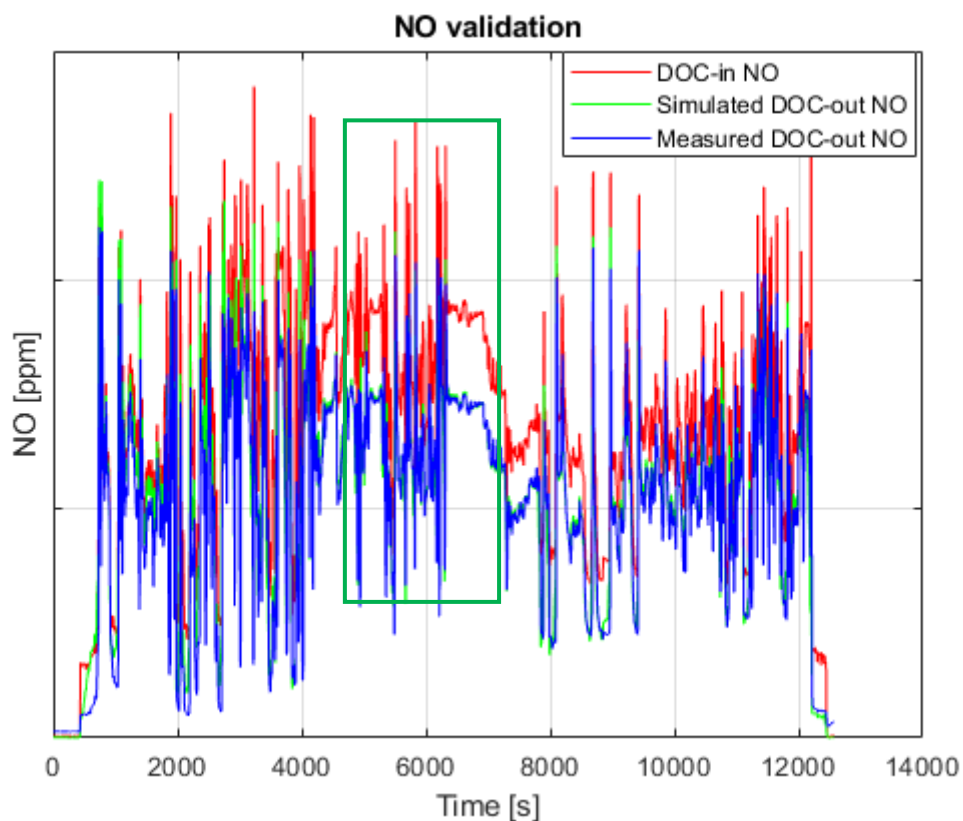


Figure 5.19 Simulated (green line) and measured (blue line) outlet concentrations of NO, and together with inlet NO concentrations (red line). The marked region is a zoom-in look which is shown in figure 5.21.

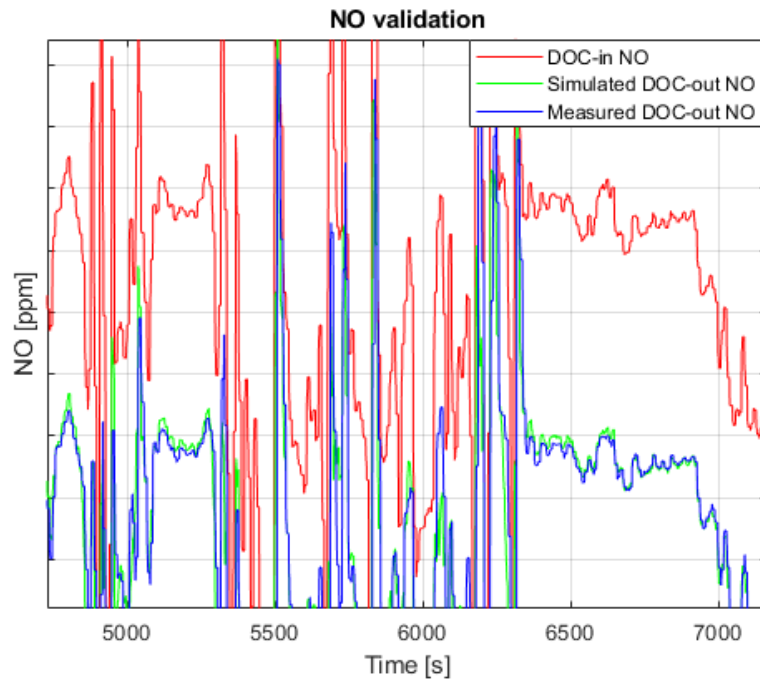


Figure 5.20 A zoom in of the NO concentrations between 5000 and 7000 s.

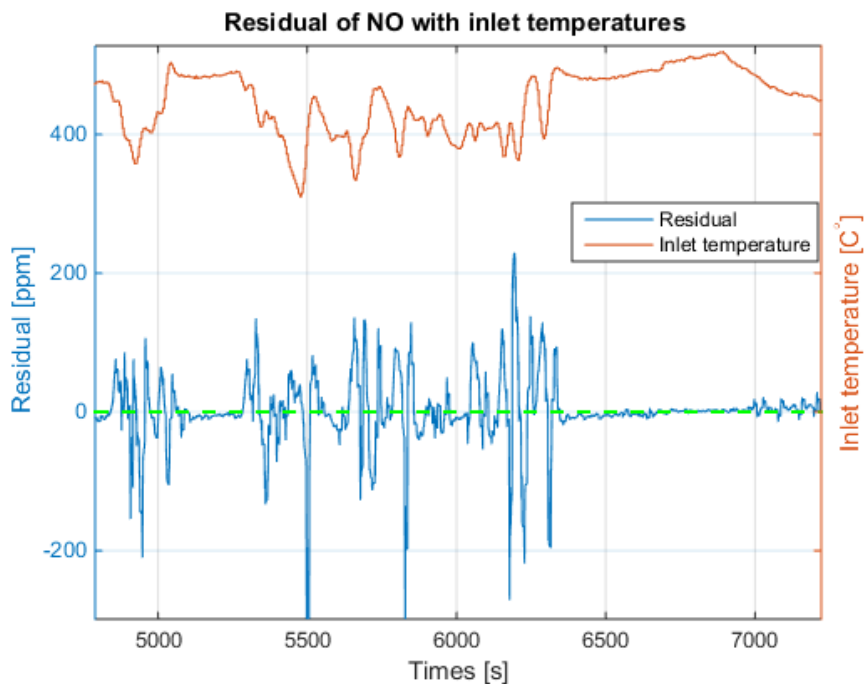


Figure 5.21 The residual (blue line) represents the difference between the measured and simulated NO concentrations. It is then compared with the inlet temperature (red line).

In figure 5.21, the maximum errors are observed at around 5500s, 5750s, and 6300s which are all more than 200 ppm. The incorrect temperature prediction can be one reason. Another is, when the inlet temperature oscillates, the residual increases. When the temperature is stable, the residual becomes smaller. This indicates that the prediction errors become large at transient points. Summing up, the validation results of NO will be improved if the temperature can be predicted correctly and transient data can be used for calibration.

5.3 DPF calibration results

This section presents the final optimized parameters of DPF model. Furthermore, the DPF simulation results using the optimized parameters are shown. The results will be analyzed and discussed.

5.3.1 Tuning of parameters for DPF model

Table 5.2 shows the optimized parameter values for heat transfer, mass transport and chemical reactions for DPF. It should be noted that CO was not optimized for DPF model since the model ignored the CO formation from both passive and active soot regeneration. Thus, the CO mass transport and kinetic parameters are not listed below and retain as optimized values from DOC.

Table 5.2 Results of parameter tuning for heat transfer, mass transport and kinetics of DPF model

Parameter	Initial value	Optimized value	Lower limit	Upper limit
Heat transfer				
hpa_coef	1	30.7	0	Inf
C_{p_steel} [J/kg·K]	460	2202.4	0	Inf
$C_{p_catalyst}$ [J/kg·K]	750	811.8	0	Inf
Mass transport				
D_{O_NO} [m ² /s]	$1.8 \cdot 10^{-6}$	$1.14 \cdot 10^{-6}$	$1.8 \cdot 10^{-7}$	$1.8 \cdot 10^{-5}$
D_{O_HC} [m ² /s]	$3.2 \cdot 10^{-6}$	$1.46 \cdot 10^{-6}$	$3.2 \cdot 10^{-7}$	$3.2 \cdot 10^{-5}$
kinetics				
E_{a_NO} [kJ/mol]	89.5	74.8	44.8	179
A_{NO} [1/s]	5945.6	754.9	594.6	59455.8
E_{a_HC} [kJ/mol]	95.5	110	47.7	191
A_{HC} [1/s]	$1.7 \cdot 10^9$	$1.7 \cdot 10^8$	$1.7 \cdot 10^8$	$1.7 \cdot 10^{10}$
$E_{a_soot_NO2}$ [kJ/mol]	38	44.5	19	76
A_{soot_NO2} [1/s]	42	181.7	4.2	420
Soot regeneration				
$E_{a_soot_pas}$ [kJ/mol]	38	65.3	19	76
A_{soot_pas} [1/s]	0.01	$2 \cdot 10^{-3}$	10^{-3}	0.1
$E_{a_soot_act}$ [kJ/mol]	125	92.4	62.5	250
A_{soot_act} [1/s]	60.9	129.5	6.1	609
Inhibition factors				
$A1_{CO}$ [1/s]	$2.1 \cdot 10^{-4}$	$2.1 \cdot 10^{-5}$	$2.1 \cdot 10^{-5}$	$2.1 \cdot 10^{-3}$
E_{a1_CO} [kJ/mol]	-8	-3.9	-16	-3.9
$A2_{HC}$ [1/s]	0.24	0.02	0.02	2.4

E_{a2_HC} [kJ/mol]	-3	-1.5	-6	-1.5
A_3 [1/s]	$2.4 \cdot 10^{-16}$	$2.4 \cdot 10^{-17}$	$2.4 \cdot 10^{-17}$	$2.4 \cdot 10^{-15}$
E_{a3} [kJ/mol]	-96.6	-48.3	-193	-48.3
A_{4_NO} [1/s]	4.8	47.9	0.48	47.9
E_{a4_NO} [kJ/mol]	31	15.5	15.5	62

Table 5.3 Results of parameter tuning for soot accumulation and pressure drop of DPF model

Optimized Parameter	Initial value	Optimized value	Lower limit	Upper limit
Channel				
F	28.454	25.2	24.2	32.7
ξ_E	2	0.03	0.02	200
Soot cake				
$\rho_{soot,c}$ [kg/m ³]	100	50.6	50	150
$\varepsilon_{soot,0}$	0.45	0.45	0.22	0.68
$k_{soot,0}$ [m ²]	$3.8 \cdot 10^{-14}$	$2.1 \cdot 10^{-14}$	$1.9 \cdot 10^{-14}$	$5.7 \cdot 10^{-14}$
SL_Th_ch [m]	$3 \cdot 10^{-6}$	$1.5 \cdot 10^{-6}$	$1.5 \cdot 10^{-6}$	$4.5 \cdot 10^{-6}$
$d_{pore,soot}$ [m]	$2.1 \cdot 10^{-6}$	$1.1 \cdot 10^{-6}$	$1 \cdot 10^{-6}$	$3.15 \cdot 10^{-6}$
Porous wall				
$\rho_{soot,w}$ [kg/m ³]	8	4	4	12
W_SL_Lim [g/L]	0.15	0.15	0.08	0.23
F_{wall}	1	0.56	0.5	1.5
$k_{wall,0}$ [m ²]	$3.2 \cdot 10^{-13}$	$2.3 \cdot 10^{-13}$	$1.6 \cdot 10^{-13}$	$4.8 \cdot 10^{-13}$
$d_{pore,wall}$ [m]	$1.8 \cdot 10^{-5}$	$1.8 \cdot 10^{-5}$	$9 \cdot 10^{-6}$	$2.7 \cdot 10^{-5}$
$\varepsilon_{wall,0}$	0.59	0.33	0.3	0.9
Ash				
ρ_{ash} [kg/m ³]	2500	2193.8	1250	3750
AL_Th_ch [m]	$2.1 \cdot 10^{-7}$	$1.9 \cdot 10^{-7}$	$1 \cdot 10^{-7}$	$3.15 \cdot 10^{-7}$
$k_{ash,0}$ [m ²]	$3.2 \cdot 10^{-13}$	$3.19 \cdot 10^{-13}$	$1.6 \cdot 10^{-13}$	$4.8 \cdot 10^{-13}$
$d_{pore,ash}$ [m]	$3 \cdot 10^{-6}$	$3 \cdot 10^{-6}$	$1.5 \cdot 10^{-6}$	$4.5 \cdot 10^{-6}$
$Clean_Wall_Cake_PM_Frac$	0.75	0.56	0.38	1.1

The observations of the final results from table 5.2 and 5.3 can be summarized in the following points:

- For heat transfer parameters, the scaling factor of the convective heat transfer coefficient between pipe and ambient becomes higher after tuning. That means heat loss is increased and simulated outlet temperature decreases to agree with the measurement. Meanwhile, the heat capacity of the steel and catalyst are also tuned to match the correct thermal mass. However, the optimized steel heat capacity is physically unreasonable. Further model improvement for heat transfer or only optimizing the substrate heat capacity are needed.
- For mass transport and kinetic parameters, the scaling factors of the effective diffusivities for the species are tuned to reduce the influence of transport resistance to the reaction rates. The pre-exponential factors differ significantly comparing to the initial values as marked in bold font, while they almost reach their minimum limits. Meanwhile, the adjusting of activation energies is relatively small. The tuning of the kinetic parameters shows that the reaction rates of NO and HC have been decreased
- Again, the inhibition mechanism is tuned to a large extent to meet the measurement. All the parameters have reached their maximum/minimum limits. The NO formation at low temperature and CO formation due to the soot oxidations are neglected in the model which can be the reasons for this high magnitude of tuning.
- Some of the parameters of soot accumulation and pressure drop are very close to their maximum/minimum limits. The magnitude of tuning is high. The main reason is due to the unknown initial soot loading. The filter used in the calibration was not a clean filter while the initial soot loading was assumed to be zero in the model.

Based on the calibrated parameters, the exhaust gas temperature, the species concentrations, and pressure drop are simulated again to evaluate how accurate the model performs

5.3.2 Temperature for DPF

Figure 5.22 shows the comparison of measured and simulated outlet temperature after the calibration. An example of the zoom-in plots is shown in figure 5.23 with the comparison of before and after calibration. The rest of the zoom-in and comparison plots can be found in the Appendix.

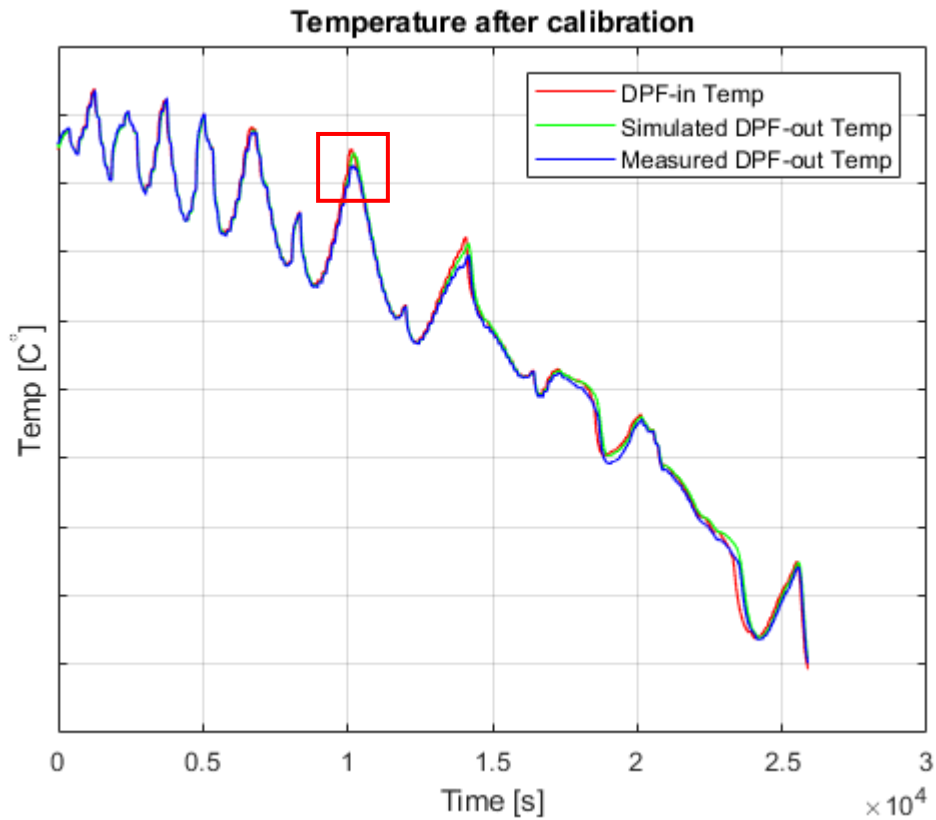


Figure 5.22 The measured (blue line) and simulated (green line) outlet temperature for all time points, together with the DPF inlet temperature (red line). The marked region is a zoom-in look which is shown in figure 5.23.

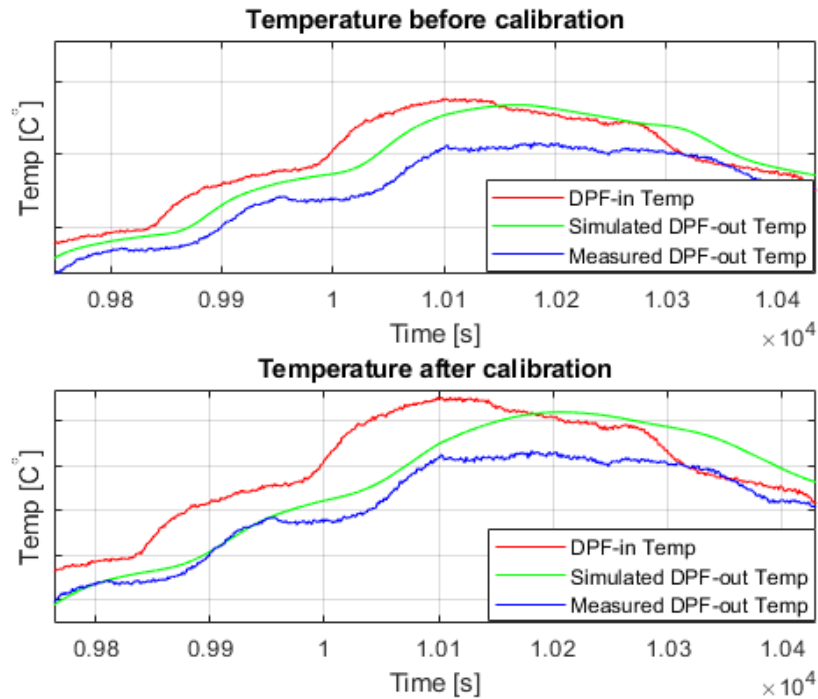


Figure 5.23 A zoom-in look at the temperature between $1 \cdot 10^4$ and $1.06 \cdot 10^4$.

From the figure 5.23, the result seems to be improved after the calibration. The further analysis of the DPF temperature result is conducted by studying the residual plot showing in figure 5.24.

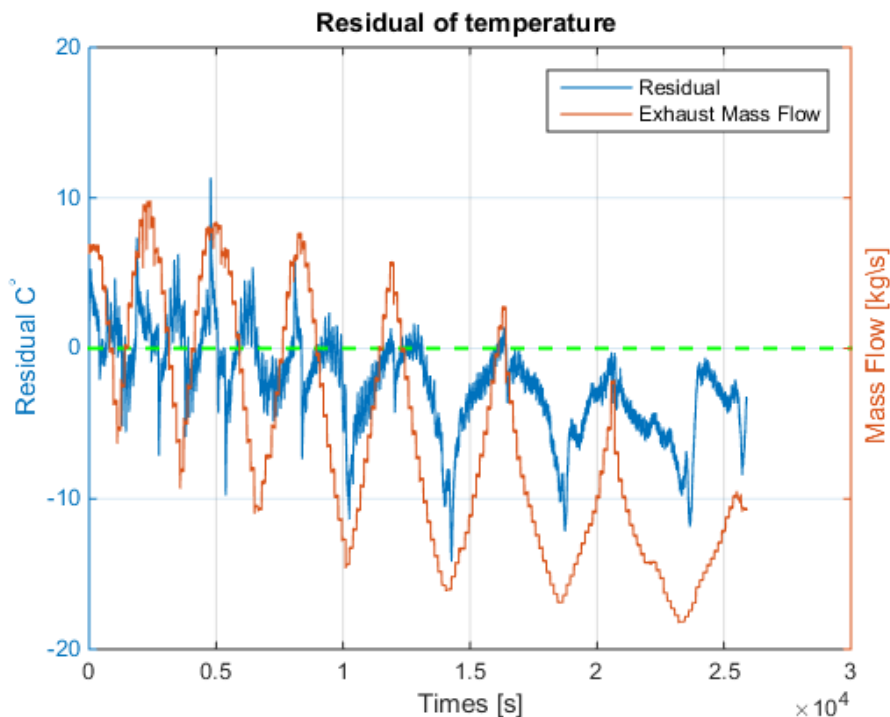


Figure 5.24 The residual (blue line) represents the difference between the measured and simulated outlet temperature. The maximum temperature deviation is around 15°C . The residual is plotted together with the mass flow to interpret the errors.

As seen in figure 5.24, the largest errors can be found either at very high mass flow or at very low mass flow. The mass flow is still an essential factor that can affect the temperature calibration. Similarly, the analysis of the DOC temperature result also applies to the DPF temperature calibration.

5.3.3 HC concentrations for DPF

The result of the HC concentrations is illustrated in figure 5.25. The zoom-in plots are shown in figure 5.26. The entire simulation result for temperature before the calibration can be found in the appendix.

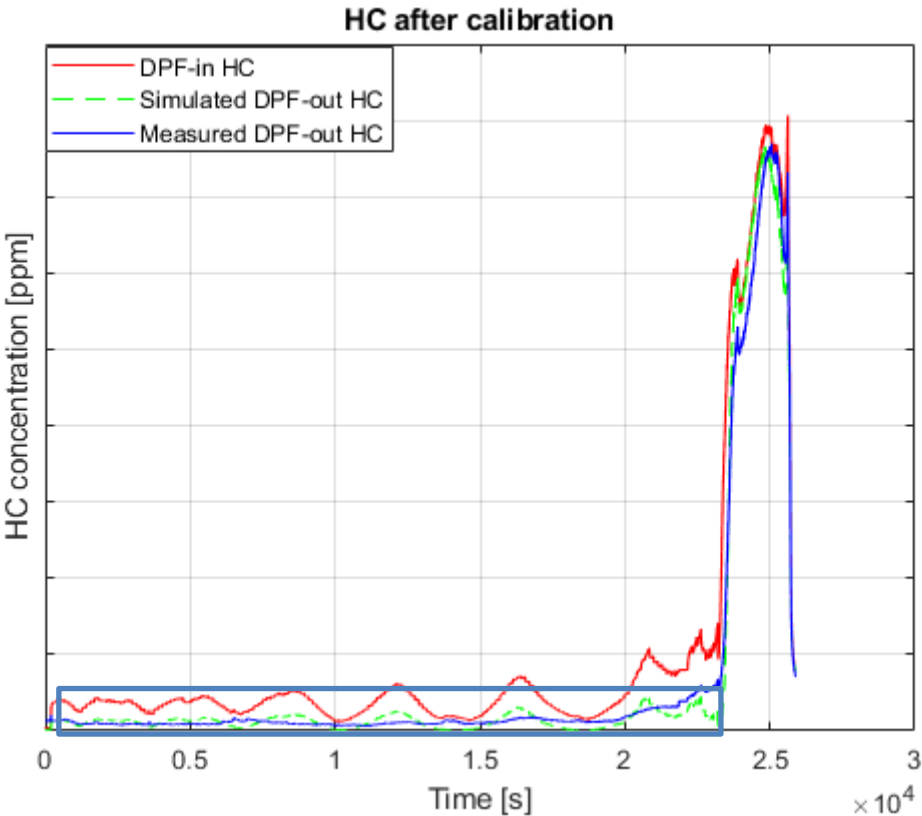


Figure 5.25 The blue line represents the measured HC outlet concentrations and the green line represents the simulated HC outlet concentrations, as well as the HC inlet concentration (red line). The marked region is a zoom-in look and shown in figure 5.26.

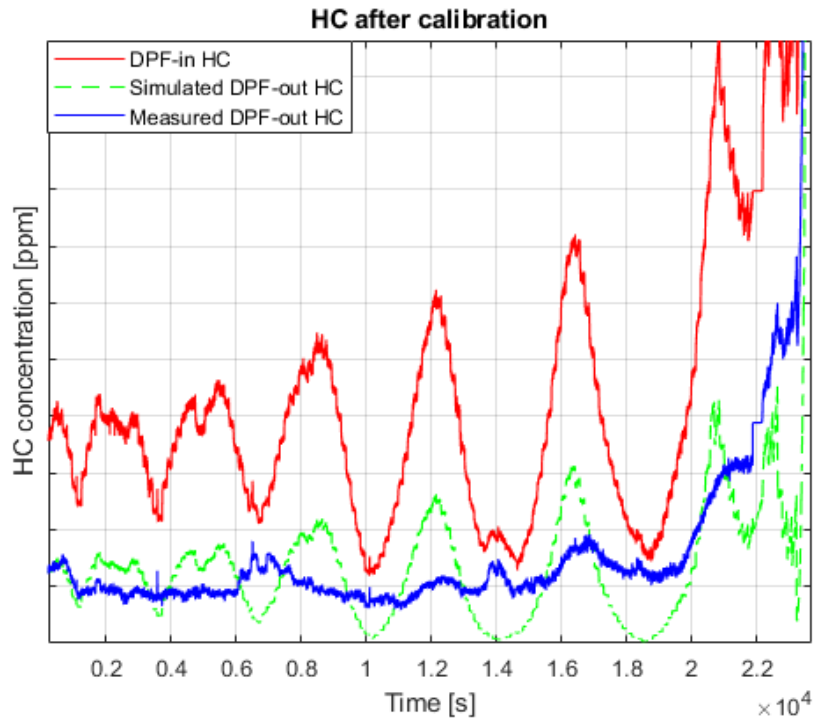


Figure 5.26 A zoom in look at the HC concentrations between 1 and $2.2 \cdot 10^4$ s.

As seen in figure 5.26, the measured HC is not zero at high temperature region. This is regarded as a measurement error as discussed before. The residual of HC at high temperature is rather small and can be neglected. The errors are mainly at a lower temperature, as seen in figure 5.27.

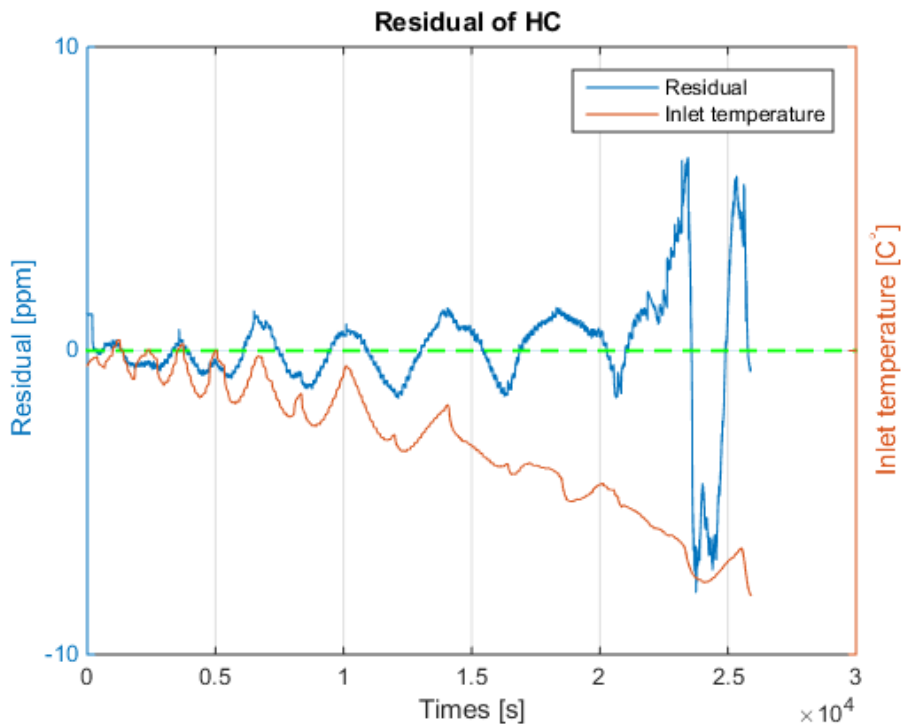


Figure 5.27 Residual of HC. The residual (blue line) represents the difference between the measured and simulated HC concentrations. The residual is then compared with the inlet temperature (red line), and the biggest deviation can be found at the end of PLM in the lower temperature range.

The reasons that large errors occurring at low temperature are attributed to the factors that have been discussed in the DOC section.

5.3.4 NO concentrations for DPF

The result of NO outlet concentrations after the calibration is presented in figure 5.28 and 5.29. The rest of the zoom-in plots and residual plot can be found in the appendix.

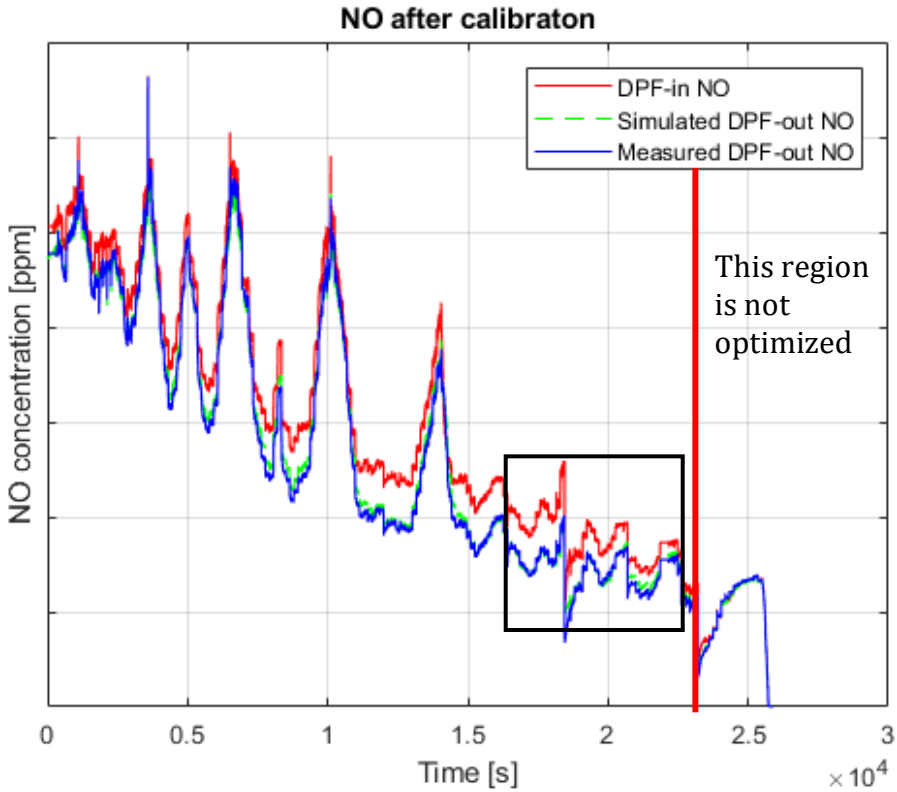


Figure 5.28 The blue line represents the measured NO outlet concentrations and the green line represents the simulated NO outlet concentrations, as well as the NO inlet concentration (red line). The marked region is zoom-in plot showing in figure 5.29.

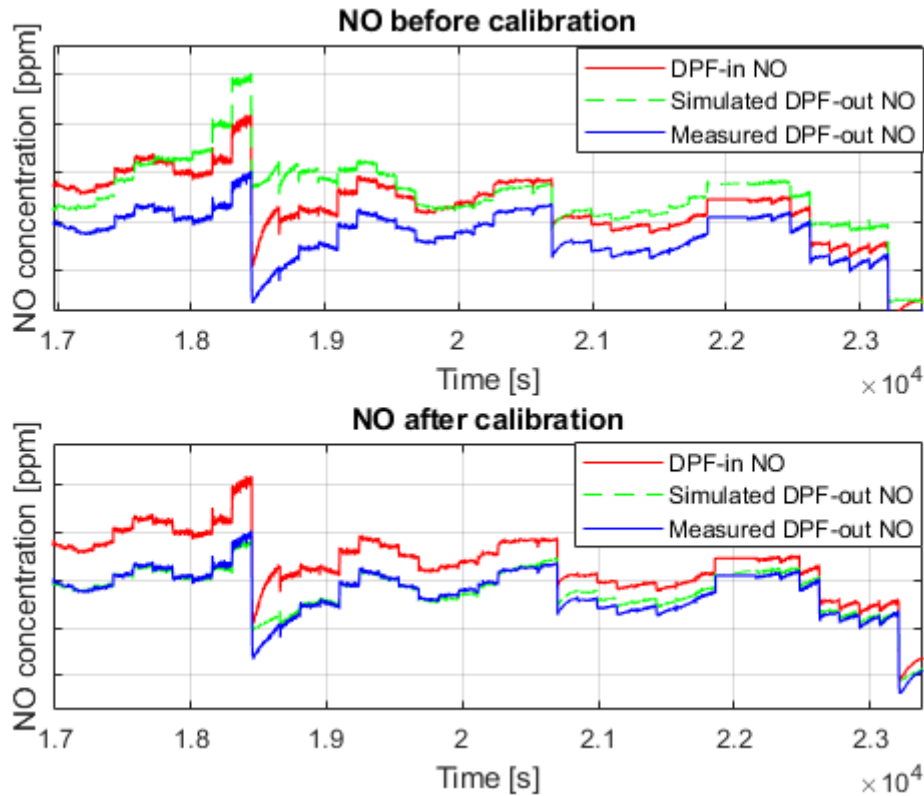


Figure 5.29 A zoom-in look of NO between $1.6 \cdot 10^4$ and $2.2 \cdot 10^4$ s.

In the figure 5.29, the result has been improved after the calibration. Similar to DOC, the accuracy of NO simulation in DPF is also influenced by temperature. However, another critical factor is soot loading. It should be stressed that a used filter measures the PLM data, but the initial soot loading is unknown and assumed to be zero in the model. The unknown soot loading is one of the main reasons for causing the NO prediction error since NO_2 would oxidize soot and NO would be by-products. Therefore, the NO prediction error will be expected in case of wrong soot loading. Hence, a measurement from a clean filter or information about a previous test cycle running in the system to guess the initial soot loading can improve the model accuracy.

5.3.5 DPF pressure drop

Figure 5.30 shows the simulated pressure drop across the DPF after calibration, together with the measured pressure drop. The residual after the calibration is presented in figure 5.32. The result before the calibration can be found in the appendix.

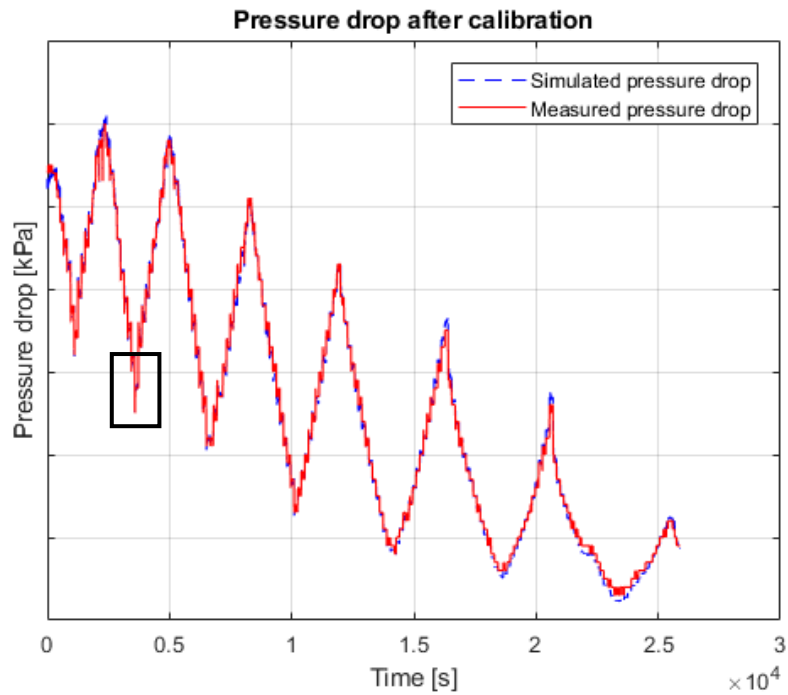


Figure 5.30 The blue line represents the simulated pressure drop, and the red line represents the measured pressure drop. The marked region is a zoom-in look and shown in figure 5.31.

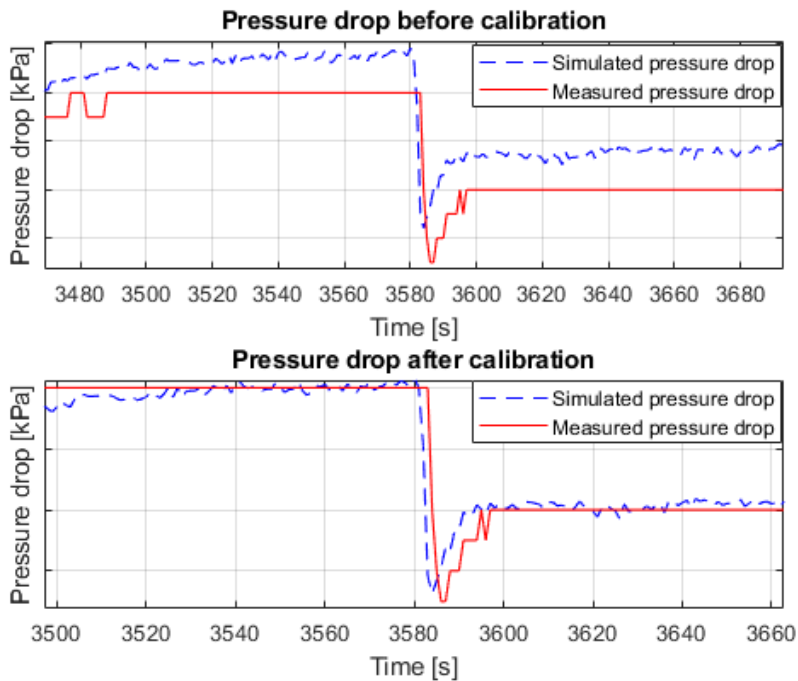


Figure 5.31 A zoom-in look of the pressure drop across DPF.

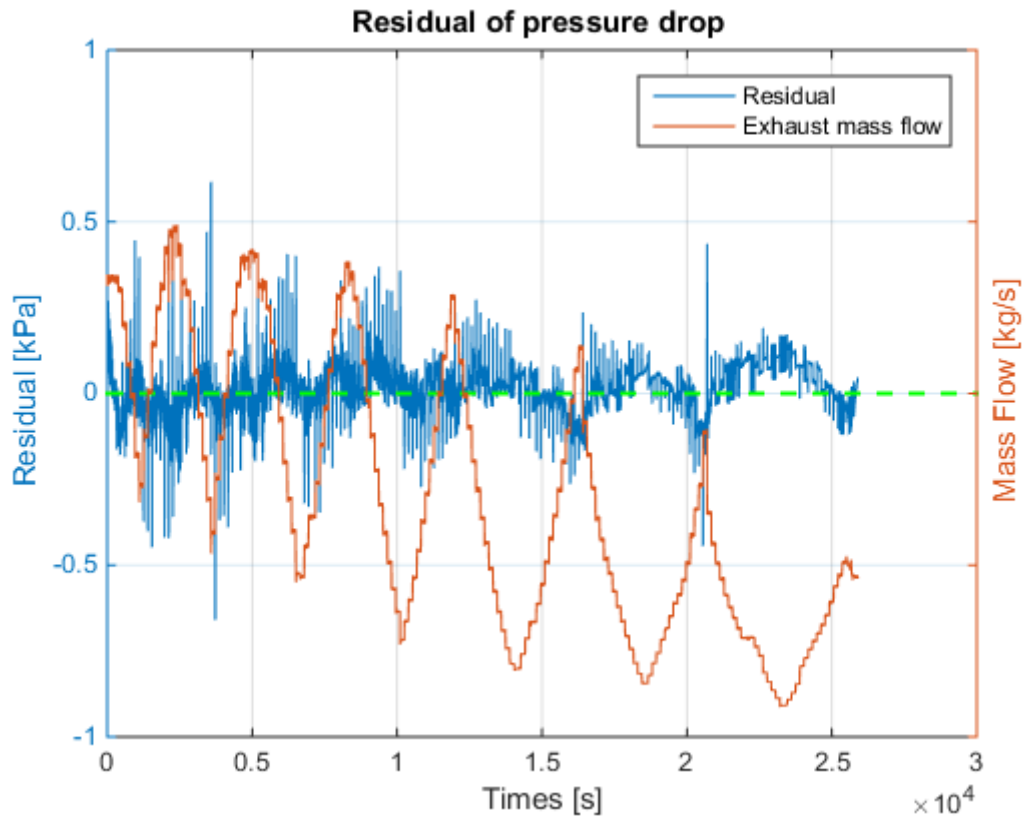


Figure 5.32 The residual (blue line) represents the difference between the measured and simulated pressure drop. The maximum error is about 0.5 kPa. The residual is then compared with the mass flow (red line) to indicate where the errors take place.

According to figure 5.31, the simulated pressure drop is improved after the calibration. It seems that a delay can be found between measurement and simulation. From figure 5.32, the residual becomes quite high at high mass flow while decreasing with mass flow decreasing. On the other hand, the initial soot loading will also influence the pressure drop. Nevertheless, the result is good in general. Since the pressure drop parameters are mainly physical properties of soot cake and wall substrate, the range for the calibration is rather limited. Consequently, a delay function to the model and a calibration to the pressure drop with the clean filter or a better guess of initial soot loading are recommended to get a better pressure drop fit.

5.4 DPF model validation

In this section, the DPF validation results are presented. The DPF model using optimized parameters was validated by running the NRTC. The discussion of the validation results is also demonstrated.

5.4.1 DPF Temperature

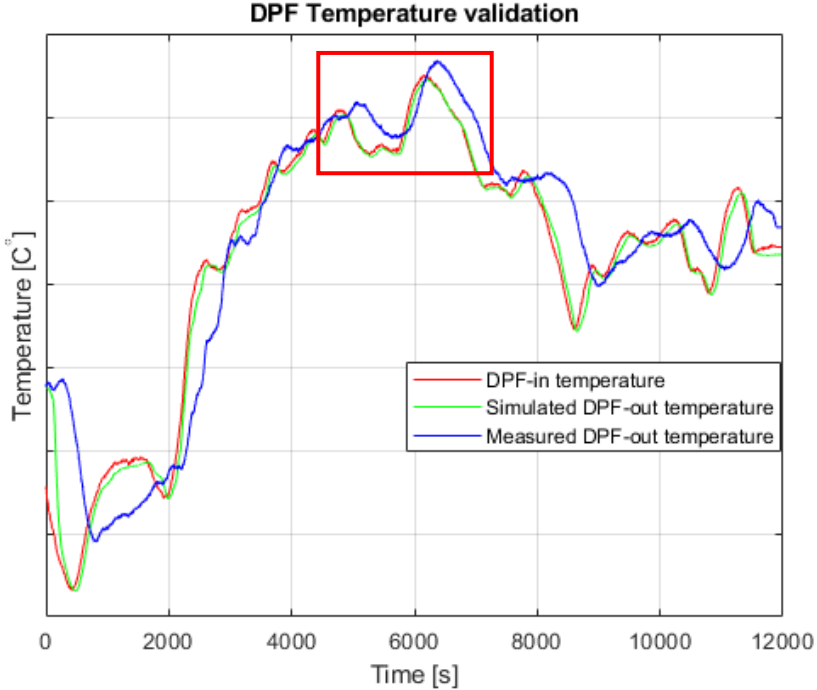


Figure 5.33 Measured (blue line) and simulated (green line) outlet temperature and together with inlet temperature (red line). The marked region is a zoom-in look which is shown in figure 5.34.

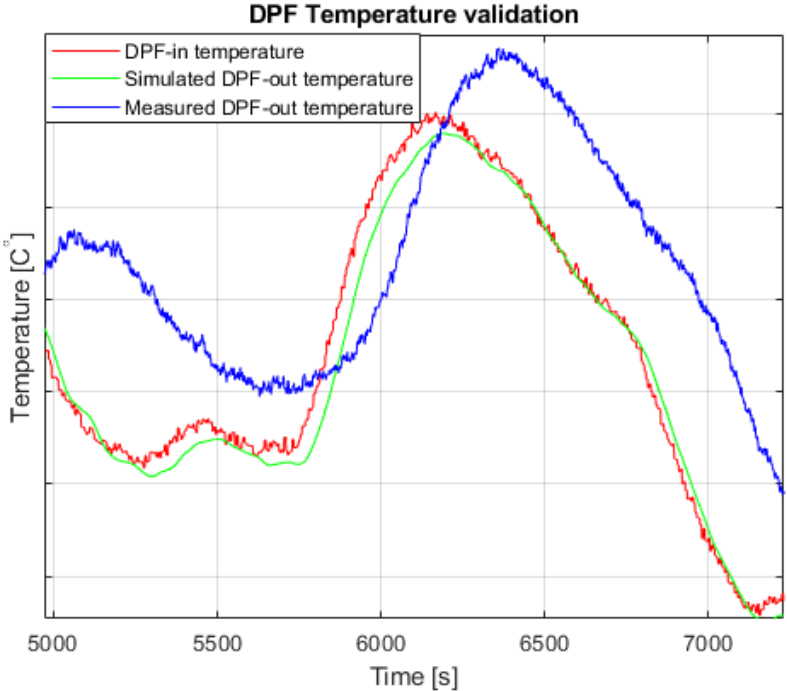


Figure 5.34 A zoom-in of the temperature between 5000 and 7000 s.

Figure 5.33 and 5.34 show the validation result of the temperature. The result is not good. The simulated temperature follows the inlet temperature very closely, indicating that the heat transfer parameters such as thermal inertia and heat losses are not well estimated, resulting in the heat transfer has a minor effect on the temperature. Since the NRTC is different to PLM, the temperature errors are expected. Further calibration on the heat transfer parameters with the transient cycle is needed, as discussed in the DOC temperature analysis.

5.4.2 Validation of other gas species concentrations and pressure drop

Since the validation results are quite similar to the DOC validation and DPF calibration, the plots of the validation results of CO, HC, NO, and pressure drop are moved to the appendix and presented there. CO concentrations are not calibrated for the DPF model. However, the validation of the CO is still performed to investigate the prediction of CO.

5.5 Combined DOC and DPF model validation

The combined DOC and DPF model was validated using the optimized parameters. The validation was performed using both PLM and NRTC. The test cycles are similar to the one using in calibration and validation of two individual models of DOC and DPF. The temperature validation results are presented in this section. The plots of the validation results of the other gas species concentrations and pressure drop are presented in appendix

5.5.1 Temperature PLM validation of DOC+DPF

Figure 5.35 shows the validation result of the temperature. Figure 5.36 shows the residual of temperature. The rest of the zoom-in plots can be found in the appendix.

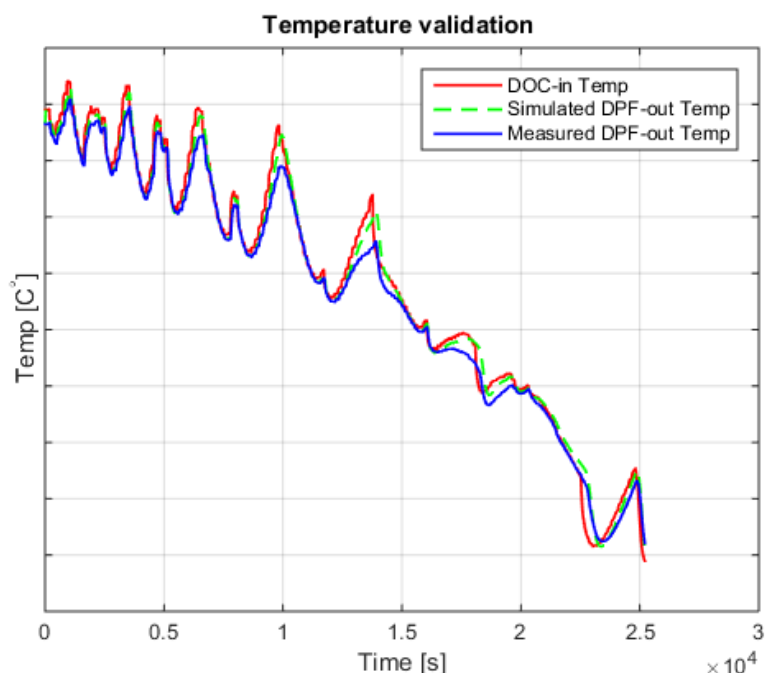


Figure 5.35 Measured (blue line) and simulated (green line) outlet temperature and together with the inlet temperature (red line).

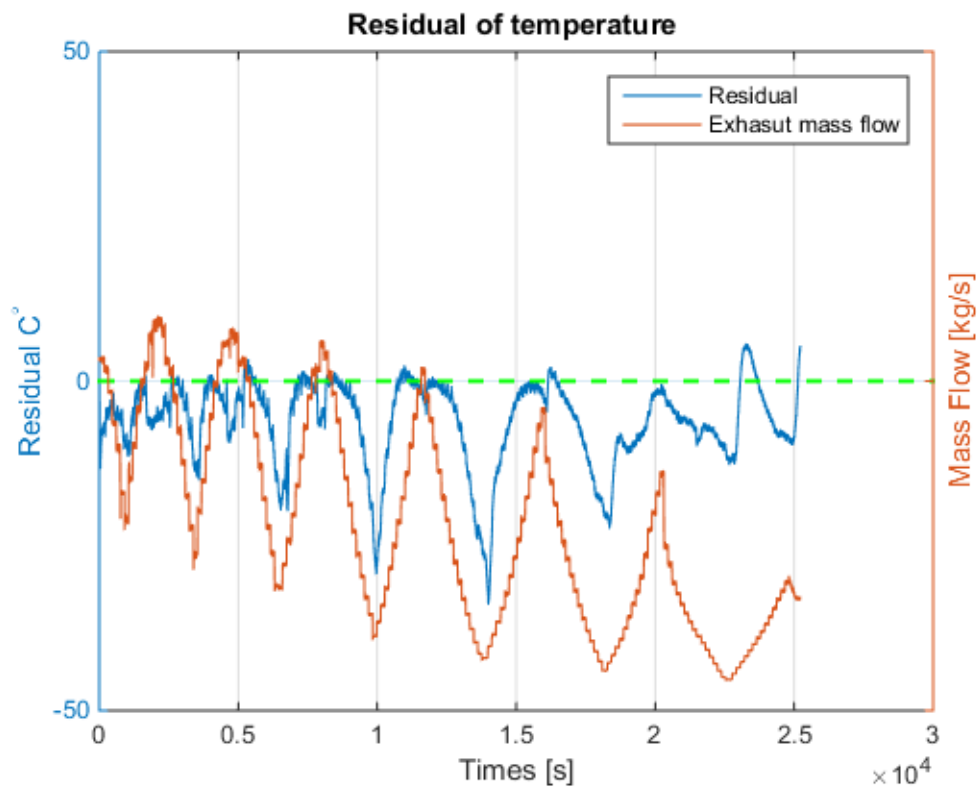


Figure 5.36 The residual (blue line) is compared with the exhaust mass flow (red line).

The errors are expected, since they include both the DOC and DPF temperature errors. As seen in figure 5.36, the residual is almost negative, showing that simulated temperatures are higher than the measurement, meaning that the heat loss is simulated too low in the model. The errors seem to change with mass flow, and the largest errors can be found at low mass flow.

5.5.2 Temperature NRTC validation of DOC+DPF

Figure 5.37 shows the validation result of the temperature.

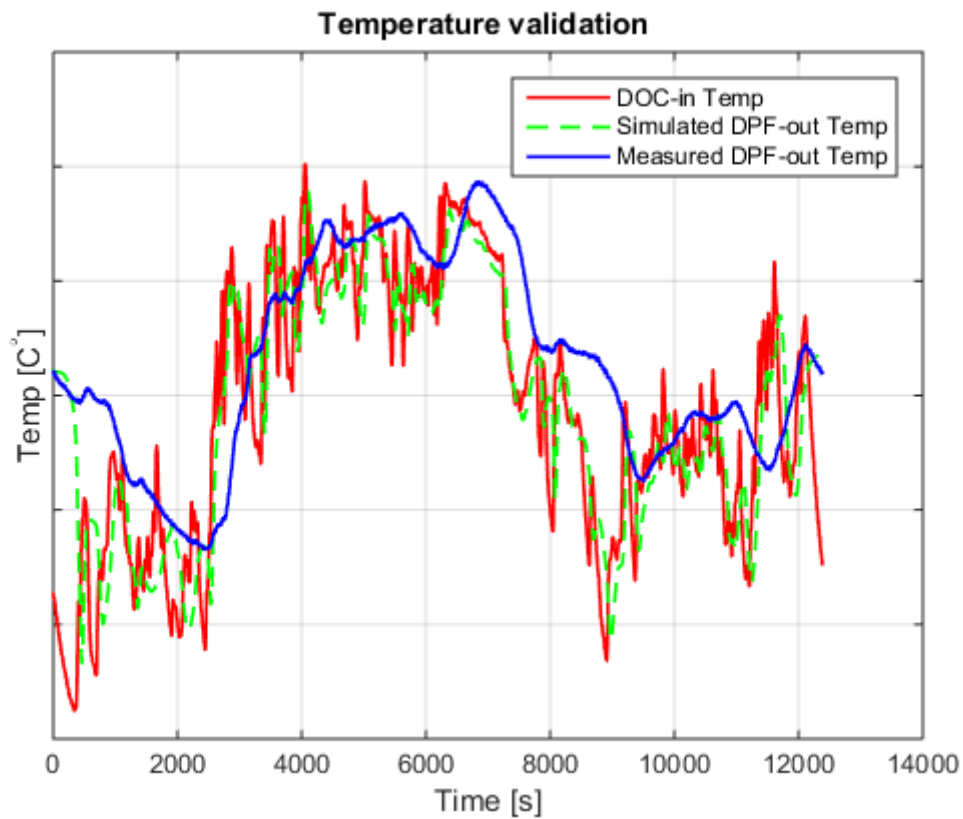


Figure 5.37 Measured (blue line) and simulated (green line) outlet temperature and together with the inlet temperature (red line).

As seen in figure 5.37, the simulated temperature follows the inlet temperature very closely, which means that the heat transfer parameters need to be further calibrated with the transient cycle.

6 Summary and conclusions

This thesis presents a calibration work on a one-dimensional DOC and DPF chemical model using nonlinear least squares optimization method. The model parameters of heat and mass transfer and reaction kinetics were optimized to minimize the difference between experimental and simulated results of the outlet temperature, CO, HC, NO concentrations and pressure drop. PLM cycle was used for the calibration and NRTC was for the validation. The work was divided into two separate parts. In the first stage, the DOC model was calibrated and validated. In the second stage, the DPF model was calibrated and validated. The plot and residual analysis of the calibration and validation results including comparison before and after the calibration were provided. In the end, without further calibration, the combined model was validated against both PLM and NRTC.

The conclusions can be summarized in the following points.

- Temperature deviation becomes large at very high mass flow or very low mass flow. Therefore, parameters that correspond to the mass flow are recommended to calibrate in the future. When performing validation with NRTC, the simulated temperature follows the inlet temperature very closely, indicating that the thermal inertia is not high enough. Therefore, further adjusting for the thermal inertia in the transient cycle is needed.
- The prediction errors of CO and HC concentrations become more obvious at lower temperatures, thus, a further calibration work at this region needs to be performed to have a better estimation of the kinetic parameters.
- The residual of NO concentrations is mainly due to the temperature deviation, kinetics parameters, and the unknown initial soot loading in the DPF. The measurement data in the DPF without any soot loading, in the beginning, is ideal to be used in the calibration work.
- The result of pressure drop shows good agreement with the measured values using both PLM and NRTC. The significant inaccuracies still come from the unknown initial soot loading.

Nevertheless, the accuracy of the model is improved after the calibration. Although at the transient points, the model error becomes quite high, it can be used as a good approximation for industrial applications, especially when using PLM and NRTC cycles.

7 Future work

Further calibration could be useful to improve the accuracy of the model. There are also some recommendations about possible extensions of this thesis work. They are proposed in this section.

Experimental measurements:

- Correct estimation of the model parameters depends on the quality of the measurement data. All the conclusions that have been made from are based on them. It will be interesting to design a specific DOE (Design of experiments) by including different catalyst configurations for the calibration and validation, measuring the experimental data under a fixed speed condition or engine load point. Also, part of the data can be weighted to estimate the related parameters.
- It is also recommended to identify new sampling strategies to reduce possible measurement errors. For example, to reduce the measurement error of HC at high temperature, improve the time alignment of the pressure drop measuring and flow signals.
- A measurement data with the clean filter will be ideal to measure NO concentrations and pressure drop across the DPF. A tracking note about previous cycle running on the system will also give a better guess for initial soot loading.

Future calibration work

- The parameter estimation is complicated by the nonlinearity of the system and high correlation between the tuning parameters. Hence, performing a parameter sensitivity analysis and calculation of parameter confidence intervals can be done to determine how many parameters that prefer to be estimated to achieve a more efficient parameter fitting.
- The system has a strong nonlinearity. A further calibration by manual needs to be considered in the future work.
- It is also recommended to design a weighting method of the residual of the different species to obtain a close fit.
- A more literature study on the tuning range of the kinetic parameters and inhibition factors can help for the improvement of the calibration work.
- Further calibration against transient data is needed to better predict the transient behavior of the heat transfer and reactions properties. Also, a calibration work on an entire model (DOC+DPF) is worth to perform.

Modeling

- A scaling factor of the convective heat transfer coefficient in the catalyst wall can be defined, or parameters which correspond to the mass flow can be defined too since the mass flow is an important factor affecting on the outlet temperature.
- The heat conduction in the solid phase could be added into the model in the future if time and resource allow.
- Moreover, include the $NO_2 + CO \rightarrow NO + CO_2$ and $NO_2 + HC \rightarrow NO + H_2O + CO_2$ chemical reactions into both the DOC and DPF model to account for NO formations at the lower temperature. Include the $C + 0.5O_2 \rightarrow CO$ and $C + NO_2 \rightarrow CO + NO$ active and passive soot oxidations into the DPF model to account better for the CO prediction.
- Better modeling of axial dispersion is needed. Also, choosing a more complex numerical solver or a smaller step size is recommended. Besides, design a delay function in the model can also be an interesting topic in the future work.

Bibliography

1. Reşitoğlu, İ.A., K. Altinişik, and A. Keskin, *The pollutant emissions from diesel-engine vehicles and exhaust aftertreatment systems*. Clean Technologies and Environmental Policy, 2015. **17**(1): p. 15-27.
2. *Emission Formation in Diesel Engines*. 2017-5-27; Available from: https://www.dieselnet.com/tech/diesel_emiform.php
3. Xi, J.a.Z., B.-J, *Soot in Diesel Combustion Systems*. Chemical Engineering & Technology, 2006. **29**: p. 665-673.
4. Heywood., J.B., *Internal Combustion Engine Fundamentals*. 1988, New York, USA: McGraw-Hill Series in Mechanical Engineering.
5. *Emission Standards: Europe: Nonroad Engines*. 2016.11; Available from: <https://www.dieselnet.com/standards/eu/nonroad.php>.
6. *Exhaust Gas Recirculation*. 2017-5-27; Available from: https://www.dieselnet.com/tech/engine_egr.php.
7. *Selective Catalytic Reduction*. 2016-11-10; Available from: https://www.dieselnet.com/tech/cat_scr.php.
8. *Catalyst Fundamentals*. 2000.11; Available from: https://www.dieselnet.com/tech/cat_fund.php.
9. *Cellular Monolith Substrates*. 1998.8; Available from: https://www.dieselnet.com/tech/cat_substrate.php.
10. Ye, S., *Oxidation Catalyst Studies on a Diesel Engine*, in *Department of Mechanical Engineering*. December 2010, Bath.
11. Wurzenberger, J.C. and R. Tatschl, *Exhaust Aftertreatment*, in *Combustion Engines Development: Mixture Formation, Combustion, Emissions and Simulation*, G.P. Merker, C. Schwarz, and R. Teichmann, Editors. 2012, Springer Berlin Heidelberg: Berlin, Heidelberg. p. 363-384.
12. *Diesel Oxidation Catalyst*. 2016-3-22; Available from: https://www.dieselnet.com/tech/cat_doc.php.
13. *Diesel Filter Regeneration*. 2017-5-15; Available from: https://www.dieselnet.com/tech/dpf_regen.php.
14. *Diesel Particulate Filters*. 2013-01-18; Available from: <https://www.dieselnet.com/tech/dpf.php>.
15. *Engine Exhaust Back Pressure*. 2009-5-26; Available from: https://www.dieselnet.com/tech/diesel_exh_pres.php.

16. Konstandopoulos, A.G., et al., *Fundamental Studies of Diesel Particulate Filters: Transient Loading, Regeneration and Aging*. 2000, SAE International.
17. Padilla, A.T., *Development of models to study the emissions, flow, and kinetic characteristics from diesel oxidation catalysts and particulate filters in Mechanical Engineering-Engineering Mechanics*. January 2005, Michigan Technological University.
18. James R. Welty, C.E.W., Robert E. Wilson, Gregory L. Rorrer. , *Fundamentals of Momentum, Heat, and Mass Transfer*. 5 ed.: John Wiley & Sons, Inc.
19. *Arrhenius equation*. 14 December 2017, at 09:19; Available from: https://en.wikipedia.org/wiki/Arrhenius_equation.
20. Voltz, S.E., et al., *Kinetic Study of Carbon Monoxide and Propylene Oxidation on Platinum Catalysts*. Product R&D, 1973. **12**(4): p. 294-301.
21. Konstandopoulos, A.G., E. Skaperdas, and M. Masoudi, *Microstructural Properties of Soot Deposits in Diesel Particulate Traps*. 2002, SAE International.
22. *Choose a Solver*. Available from: <https://se.mathworks.com/help/simulink/ug/types-of-solvers.html#f11-56725>.
23. *Nonroad Transient Cycle (NRTC)*. Available from: <https://www.dieselnet.com/standards/cycles/nrtc.php>.
24. *Simulink® Design Optimization™ User's Guide*. The MathWorks, Inc.
25. sjöblom, J., *Parameter estimation in heterogeneous catalysis*, in *Department of Chemical and Biological Engineering*. 2009, Chalmers University of Technology.
26. *lsqnonlin*. Available from: <https://se.mathworks.com/help/optim/ug/lsqnonlin.html>.
27. *Speed Up Parameter Estimation Using Parallel Computing*. Available from: https://se.mathworks.com/help/sldo/ug/speedup-using-parallel-computing_brzoodu-1.html.
28. *Adiabatic temperature rise*. Available from: http://www.safety-s2s.eu/modules.php?name=s2s_wp4&idpart=4&idp=323.
29. Oh, S.H. and J.C. Cavendish, *Transients of monolithic catalytic converters. Response to step changes in feedstream temperature as related to controlling automobile emissions*. Industrial & Engineering Chemistry Product Research and Development, 1982. **21**(1): p. 29-37.
30. ALMQVIST, F., *Combined Empirical and 1D Modeling Approach for Exhaust Aftertreatment System for Heavy Duty Diesel Engines*, in *Innovative and Sustainable Chemical Engineering*. Chalmers university of technology.

A User's guide in Simulink Design Optimization

In this appendix A, some references from the user's guide in the parameter estimation toolbox are introduced here to guide the readers of using the Simulink Design Optimization toolbox to calibrate the Simulink model. For the details of the content, see *Simulink® Design Optimization™ User's Guide*. R2015b. The MathWorks, Inc.

- Import data: This section tells you how to create an experiment and specify input and output signal data. After you create an experiment, you can import data into your experiment from various sources like MAT-files, Excel® files, or comma-separated-value files. For the details, see *chapter 1, data analysis and processing, Import data on page 1-6*.
- Preprocessing data: This section tells you the way to preprocess data before performing the estimation. The preprocessing operations are for example Scale data, Remove offset or filter data. For the details, see *chapter 1, data analysis and processing, preprocessing data on page 1-16*.
- Specify parameters for estimation: This section describes the way for specifying parameters for estimation experiments. It tells you how to specify initial values and upper and lower bounds of the parameters. For the details, see *chapter 2, parameter estimation, Specify parameters for estimation on page 2-8*.
- Estimation options: This section describes different options of the toolbox. There are three main group options: General options for setting optimization progress and result options. Optimization options including optimization method and algorithm, as well as function tolerance. Also, Parallel options which enable the parallel computing to speed up the estimation. For the details, see *chapter 2, parameter estimation, Estimation options on page 2-30*.
- How to use Parallel computing for Parameter Estimation: This section will guide you how to speed up parameter estimation using parallel computing on multicore processors or multiprocessor networks. For the details, see *chapter 2, parameter estimation, How to use Parallel computing for Parameter Estimation, on page 2-60*.

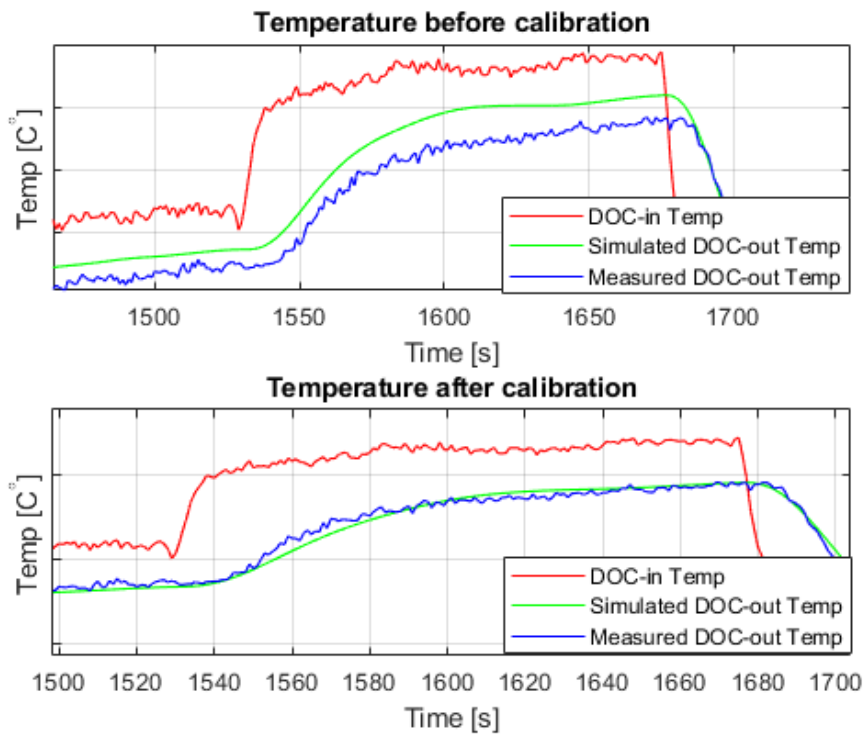
Examples: These examples show how to use experimental data to estimate model parameter values.

1. Estimate model parameter values (Using MATLAB script). On page 2-92
2. Estimate model parameters and initial states (Using MATLAB script). On page 2-104
3. Estimate model parameters using multiple experiments (Using MATLAB script). On page 2-116

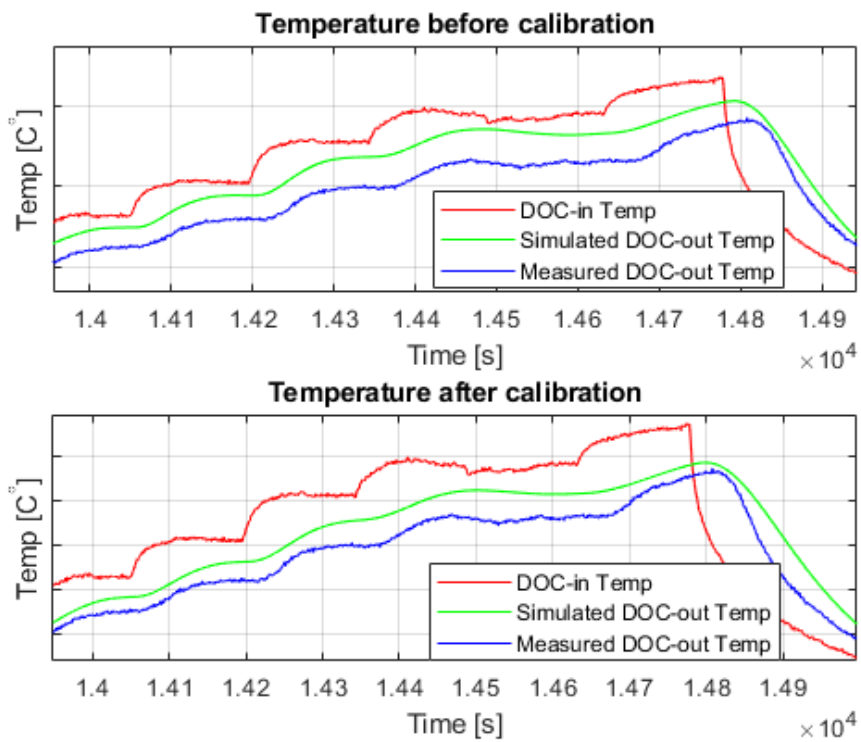
4. Estimate model parameters per experiment (Using MATLAB script). On page 2-128
5. Estimate model parameter values (GUI, Graphic user interface). On page 2-153
6. Estimate model parameters per experiment (GUI). On page 2-166
7. Estimate model parameters and initial states (GUI). On page 2-181
8. Improving optimization performance using fast restart (GUI). On page 2-198
9. Improving optimization performance using fast restart (MATLAB script). On page 2-206.

B DOC model calibration results

In this appendix B, the rest of the zoom-in and comparison plots between before and after the calibration of DOC model are presented here.



(a)



(b)

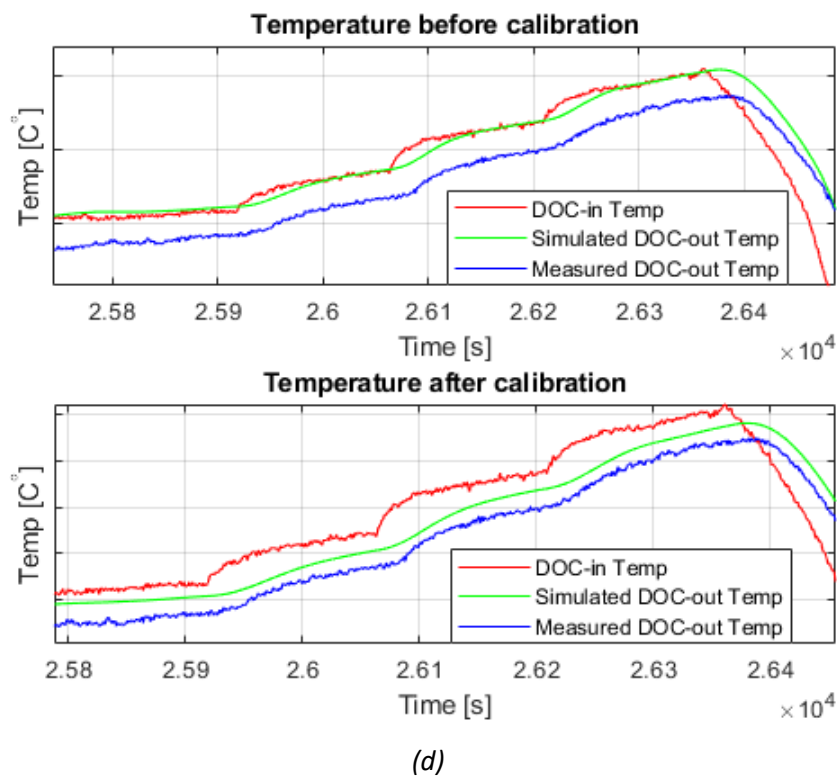
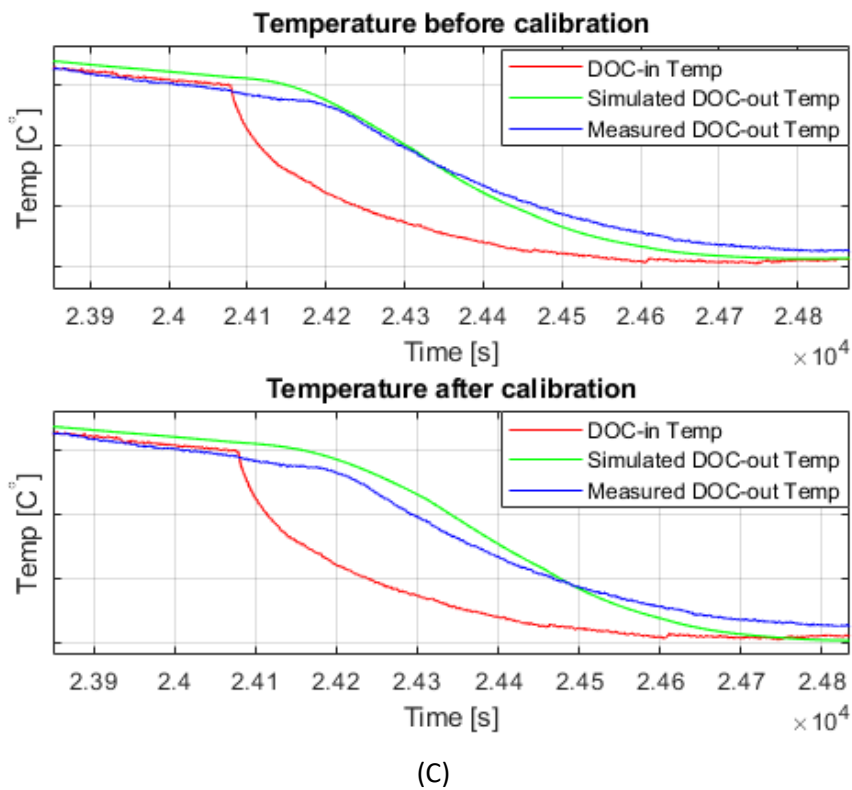


Figure B.1 Zoom-in plots of the outlet temperature. The upper chart represents the outlet temperature before calibration and the lower chart shows the temperature after the calibration. Each plot shows the measured (blue line) and simulated (green line) outlet temperature for all time points, together with the DOC inlet temperature (red line).

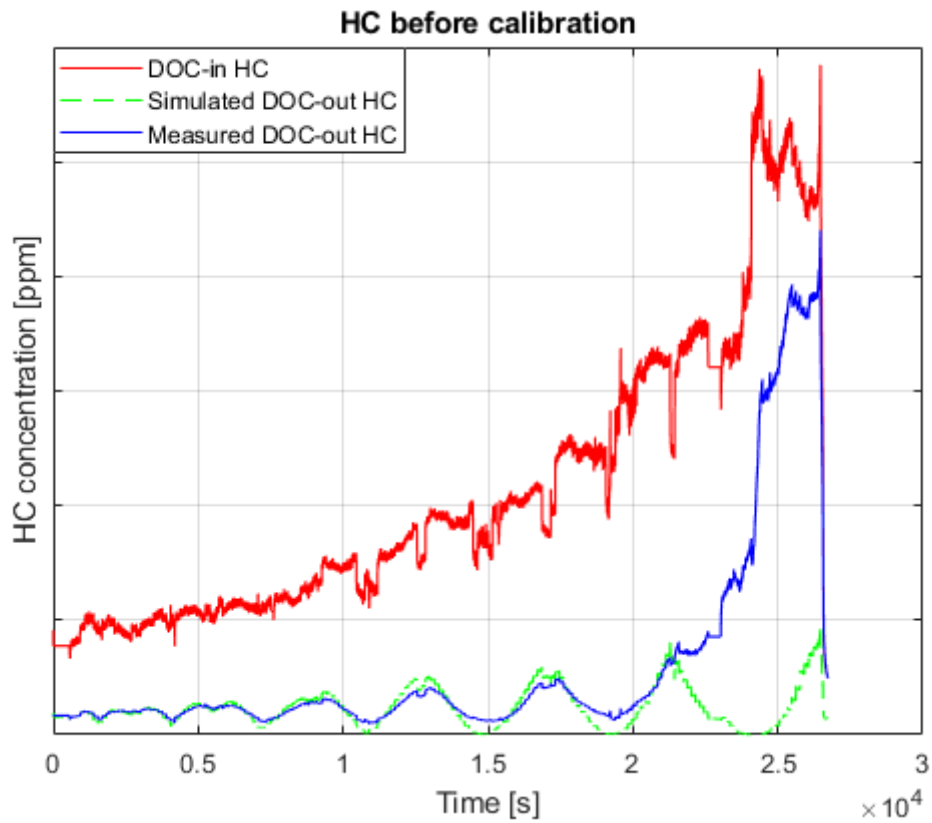
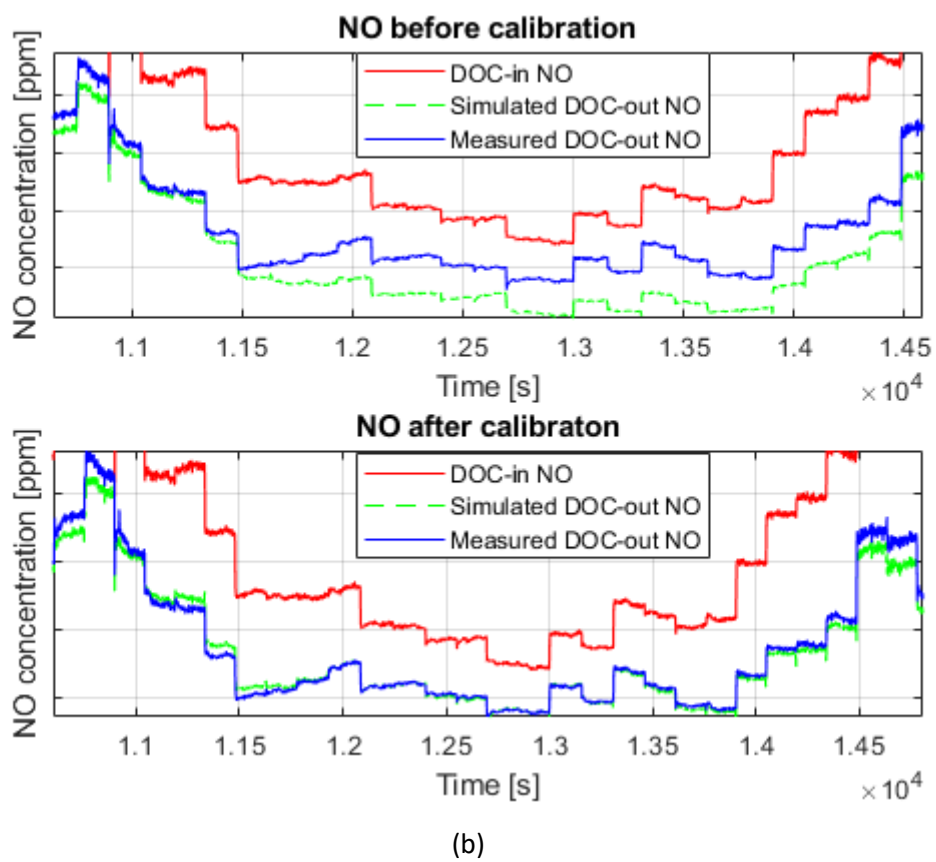
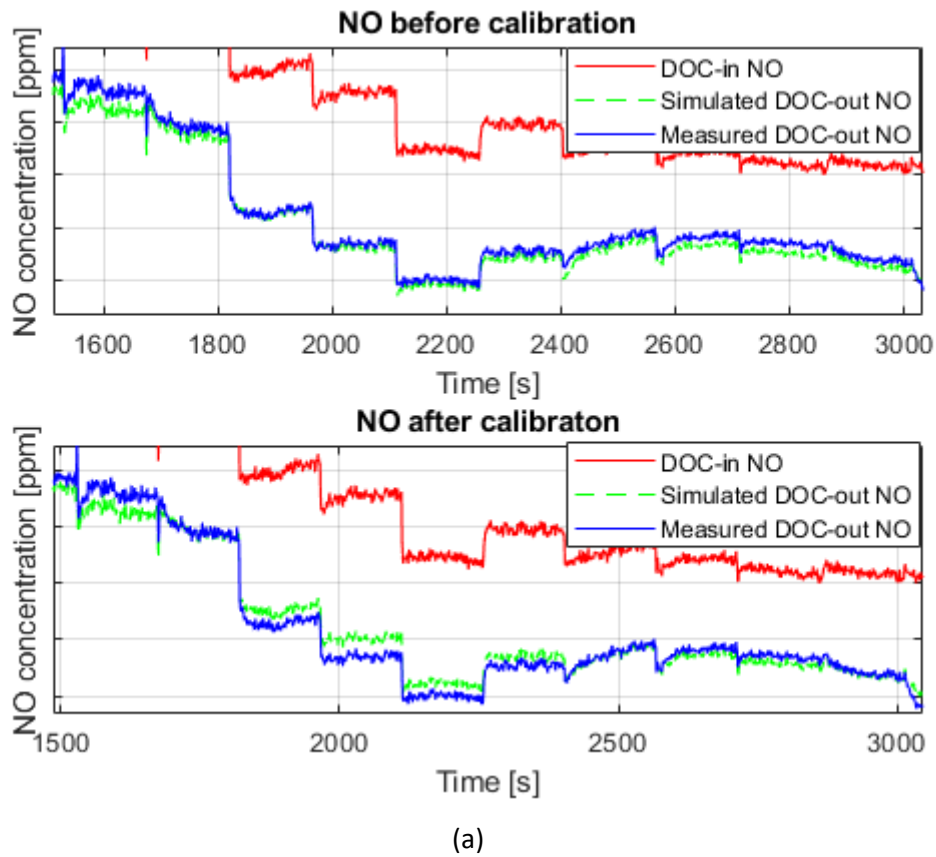


Figure B.2 Simulation results before the calibration. The blue line represents the measured HC outlet concentrations and the green line represents the simulated HC outlet concentrations, as well as the HC inlet concentration (red line).



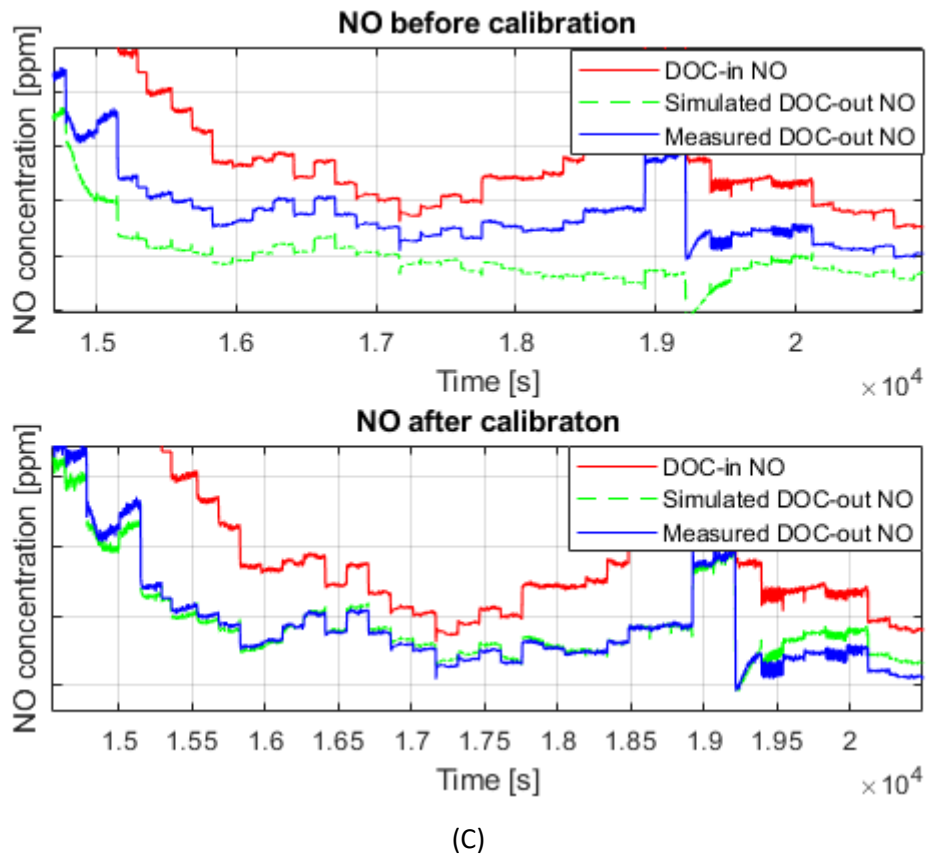


Figure B.3 The upper chart represents NO concentrations before calibration and the lower chart shows NO concentrations after the calibration. The blue line represents the measured NO outlet concentrations and the green line represents the simulated NO outlet concentrations, as well as the NO inlet concentration (red line).

C DOC model validation results

In this appendix C, the temperature residuals plot according to the model validation is presented here.

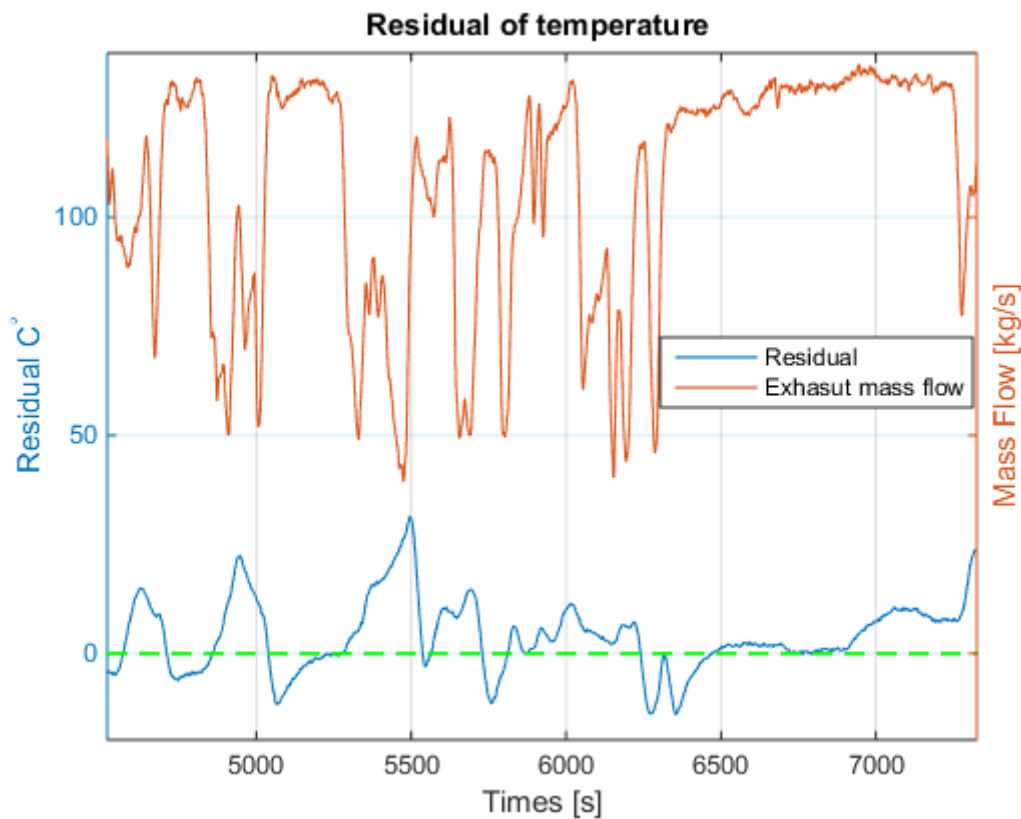
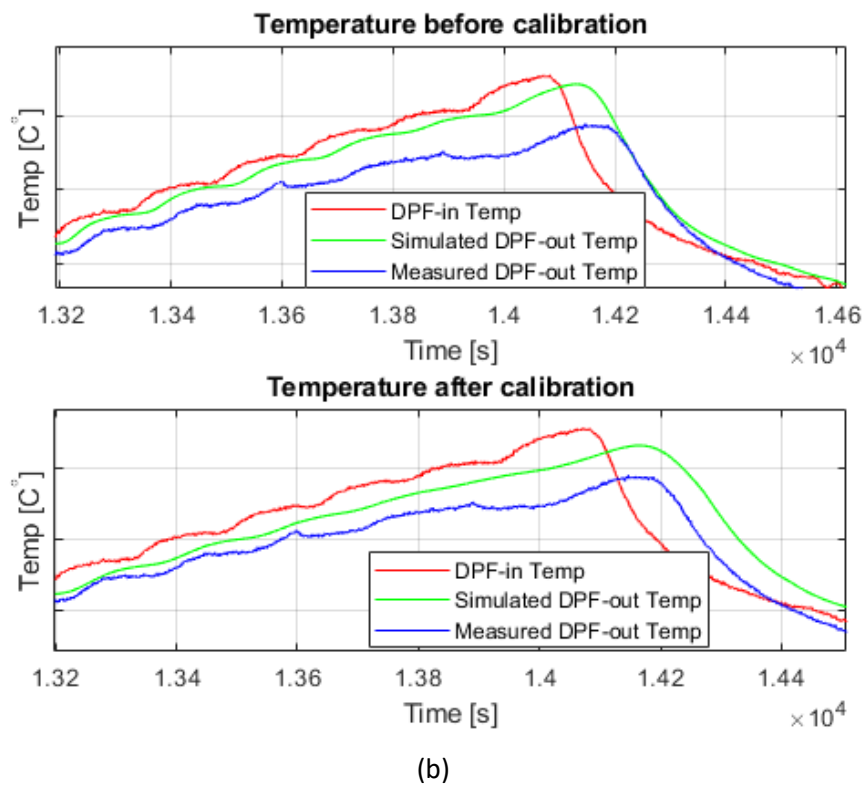
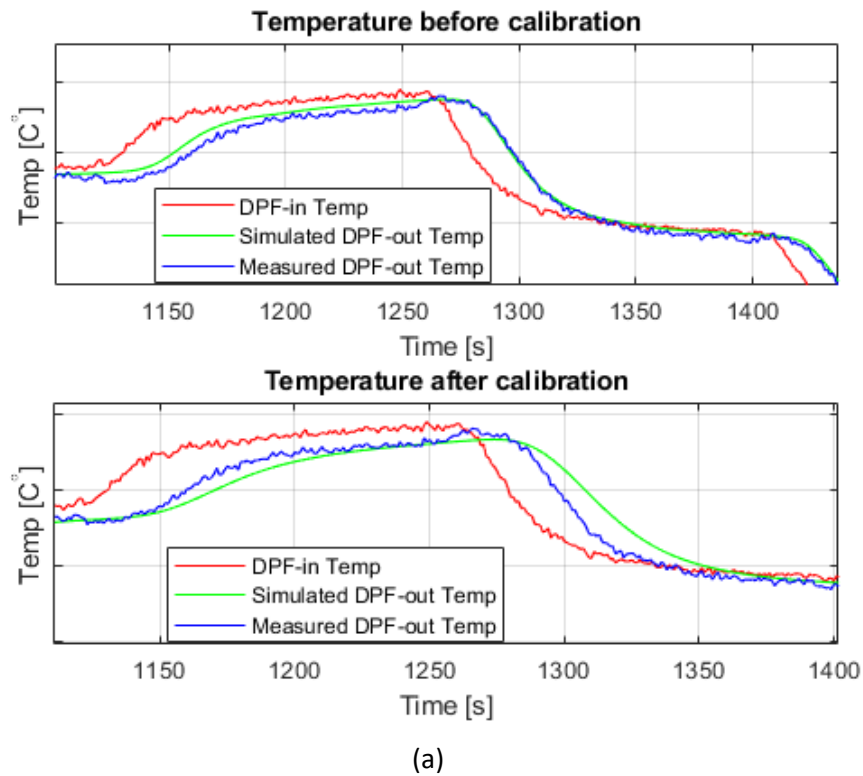


Figure C.1 The figure shows a zoom-in plot of the temperature residual between 5000 and 7000 s. The residual (blue line) represents the difference between the measured and simulated outlet temperature. The plot is compared with the exhaust mass flow (red line). When the mass flow becomes flat (between 5100 and 5250 s), the residual is close to zero. As the mass flow starts to fluctuate, the residual starts to increase. When the mass flow becomes flat between 6400 and 6900 s, the residual approaches to zero again. This demonstrates that the model does not predict the temperature well when the mass flow fluctuates frequently.

D DPF model calibration results

In this appendix D, the rest of the zoom-in and comparison plots between before and after the calibration of DPF model are presented here.



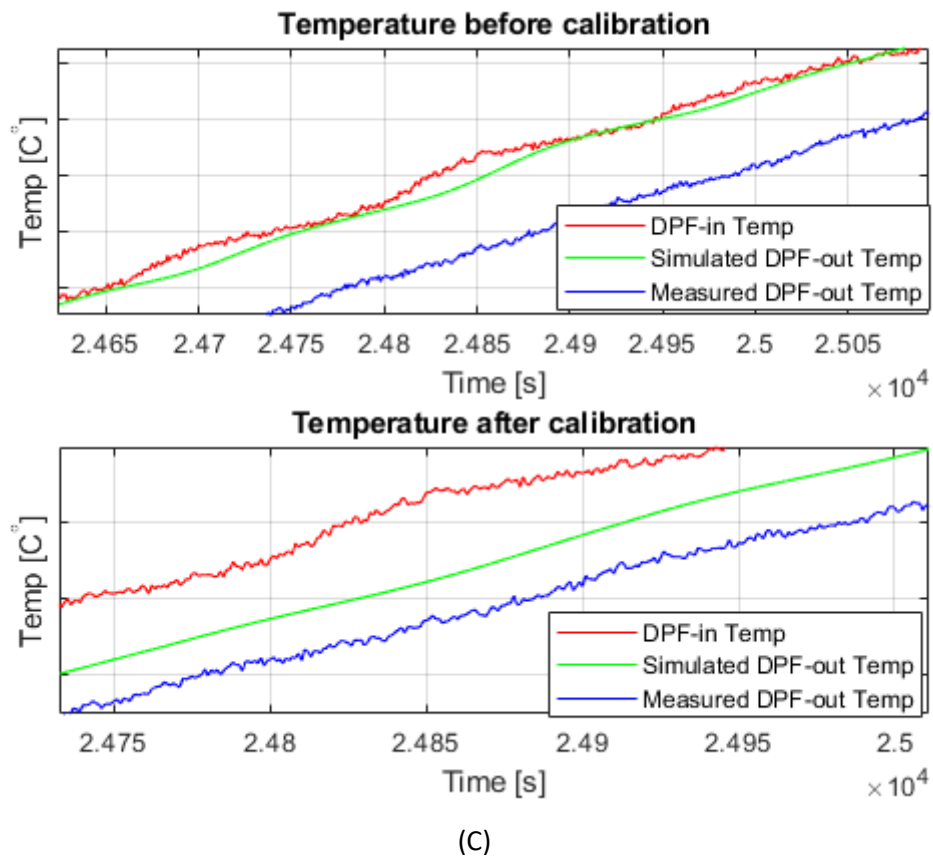


Figure D.1 Zoom-in plots of the outlet temperature. The upper chart represents the outlet temperature before calibration and the lower chart shows the temperature after the calibration. Each plot shows the measured (blue line) and simulated (green line) outlet temperature for all time points, together with the DPF inlet temperature (red line).

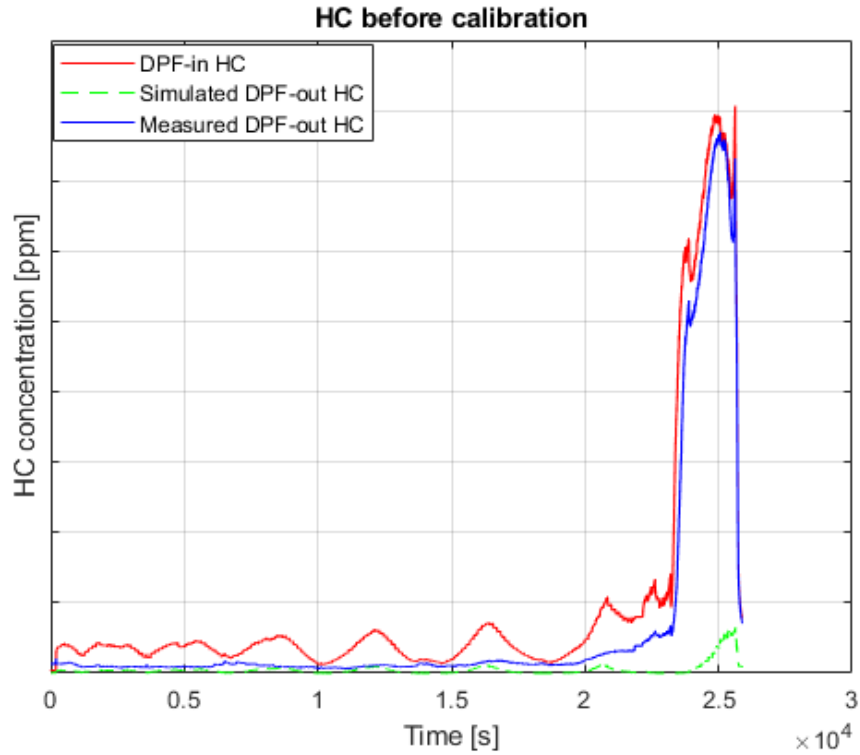


Figure D.2 Simulation results before the calibration. The blue line represents the measured HC outlet concentrations and the green line represents the simulated HC outlet concentrations, as well as the HC inlet concentration (red line).

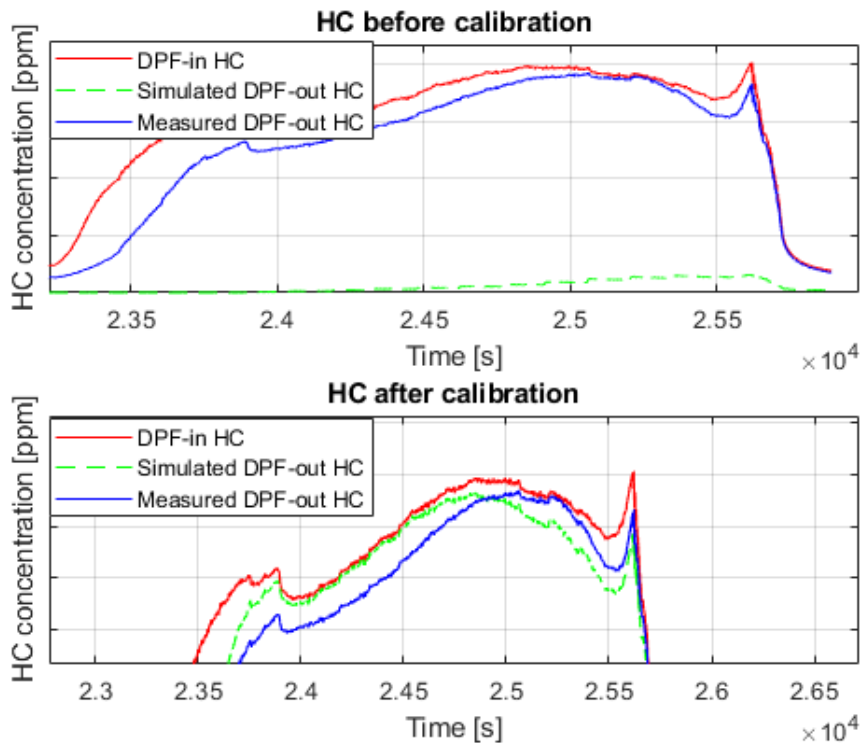
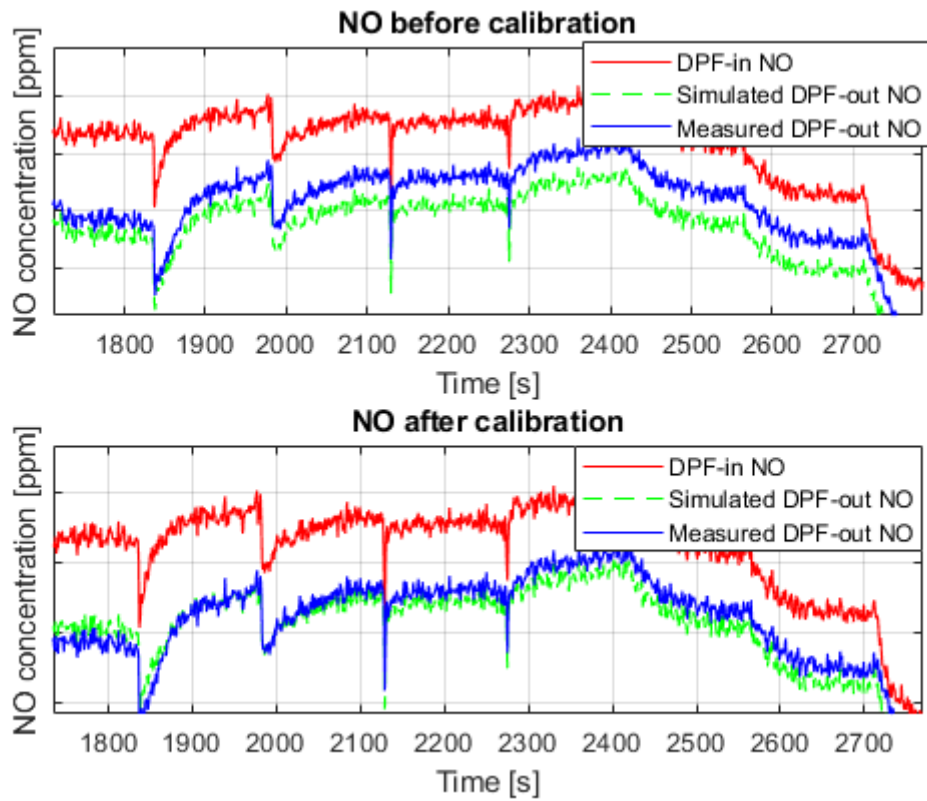
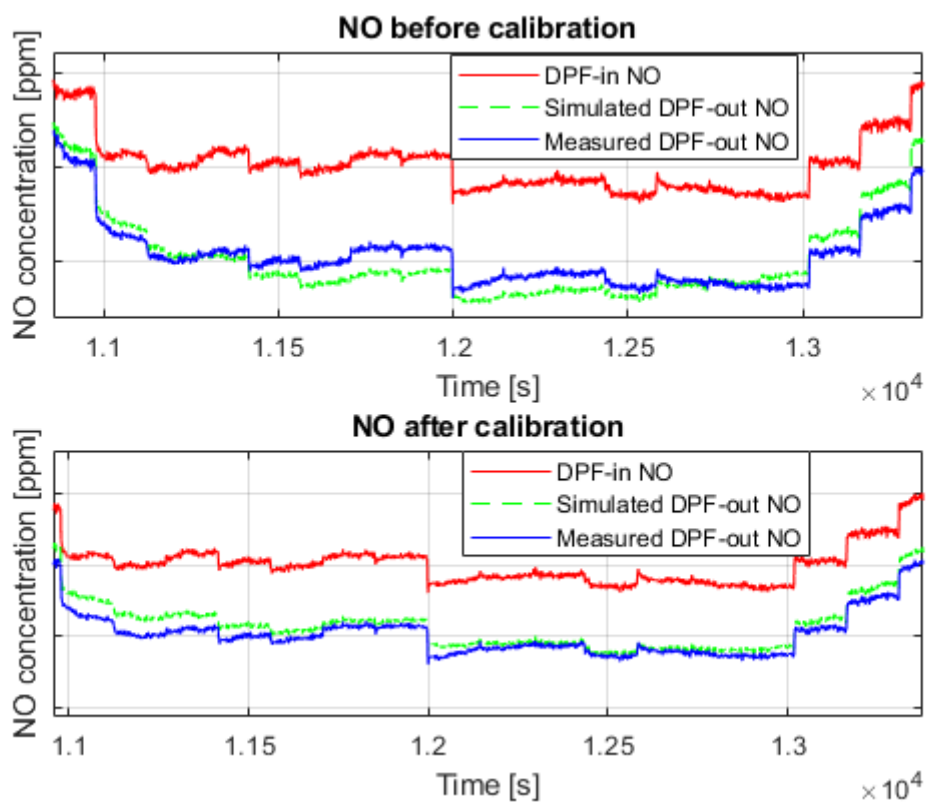


Figure D.3 A zoom-in look of the HC at the end of PLM cycle. the simulated HC is improved after the calibration.



(a)



(b)

Figure D.4 The upper chart represents NO concentrations before calibration and the lower chart shows NO concentrations after the calibration.

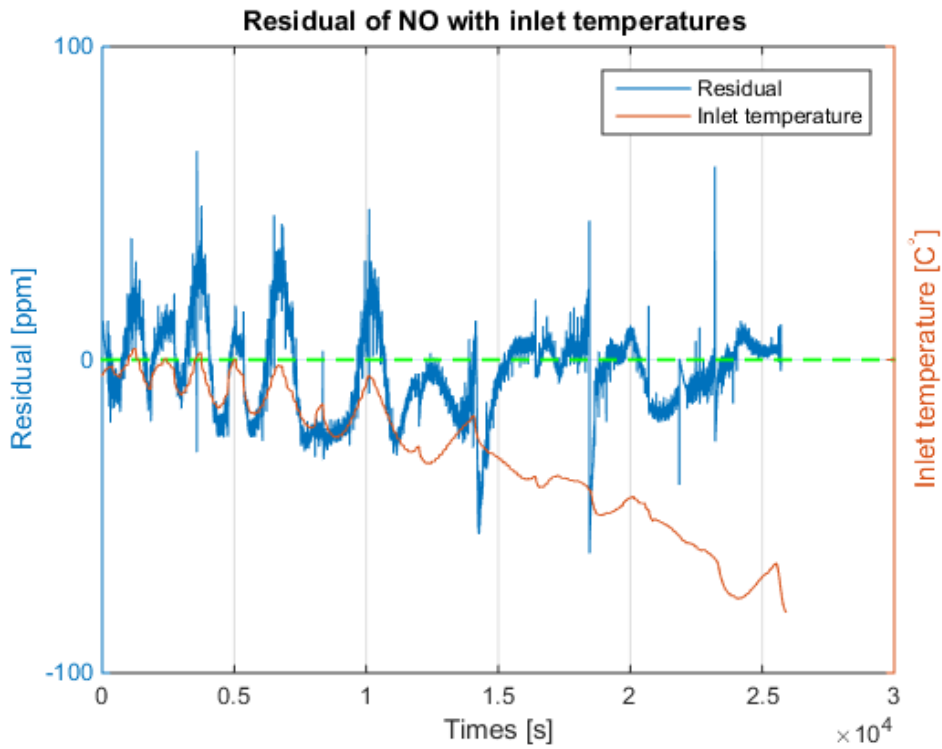


Figure D.5 The residual (blue line) represents the difference between the measured and simulated NO concentrations. The largest error is around 50 ppm. The residual is then compared with the inlet temperature (red line) to indicate where the error can be found.

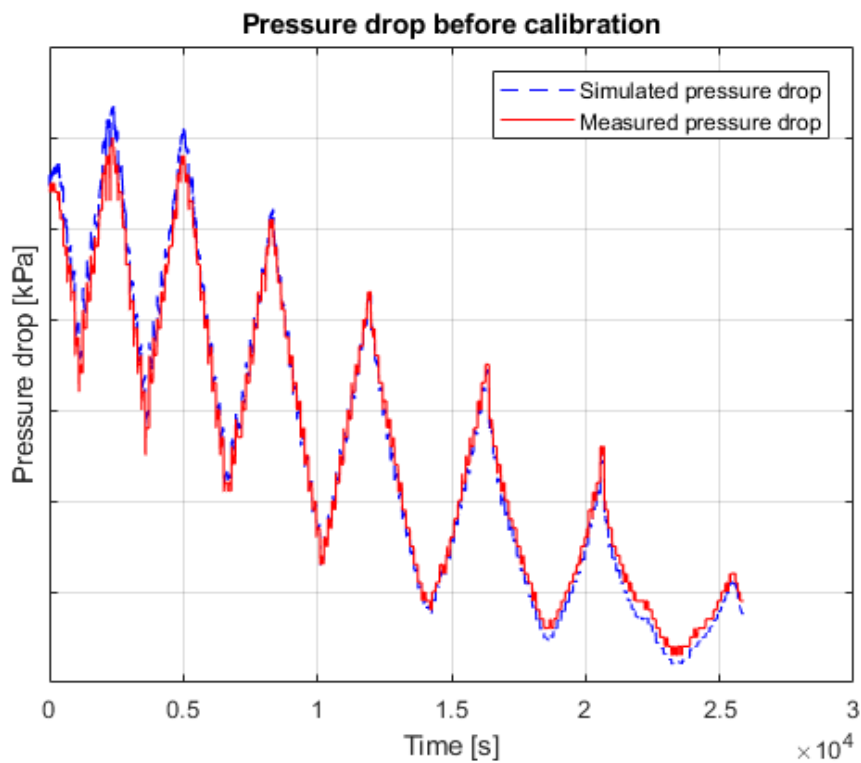


Figure D.8 Pressure drop before the calibration. The blue line represents the simulated pressure drop and the red line represents the measured pressure drop.

E DPF model validation results

In this appendix E, the temperature residuals plot is presented here. The plots of the validation results of CO, HC, NO, and pressure drop of the DPF are also illustrated here.

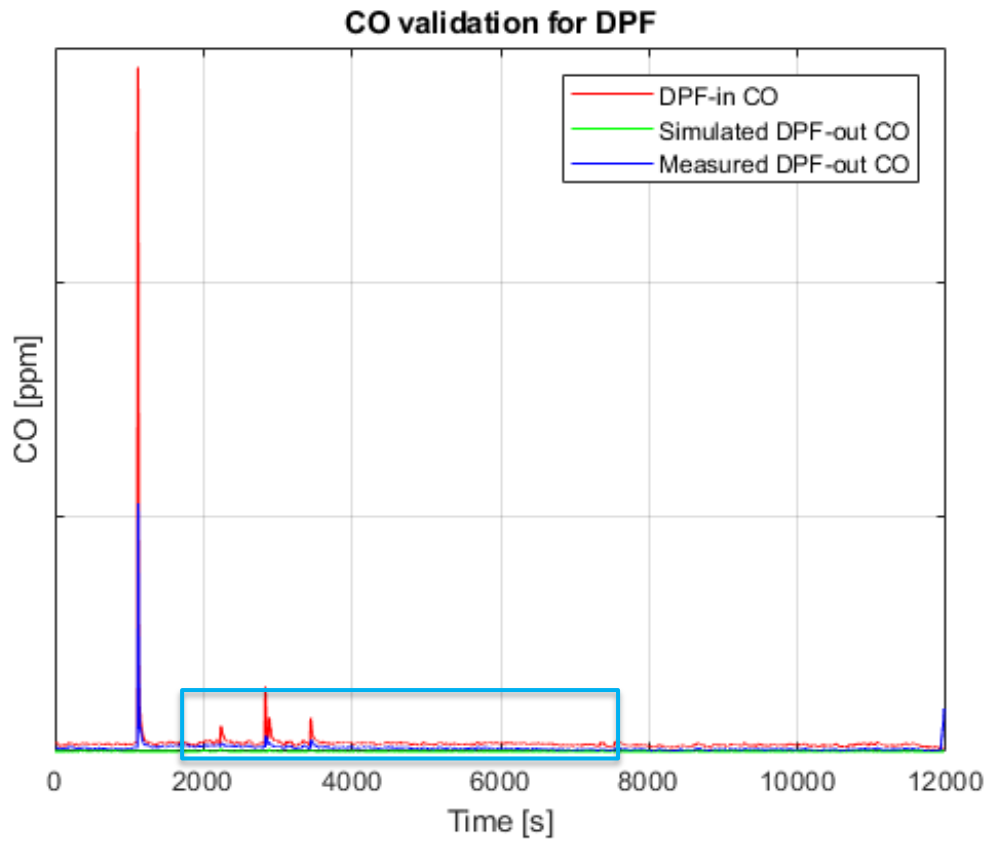


Figure E.1 Simulated (green line) and measured (blue line) outlet concentrations of CO, and together with inlet CO concentrations (red line). The marked region is a zoom-in look which is shown in figure E.2.

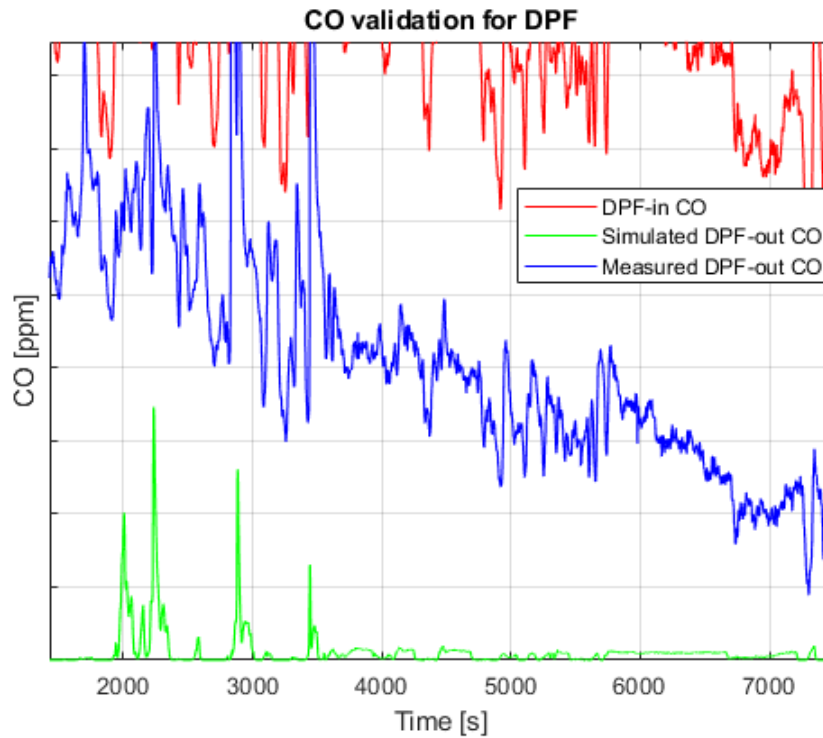


Figure E.2 A zoom-in of the CO concentrations between 2000 and 7000 s.

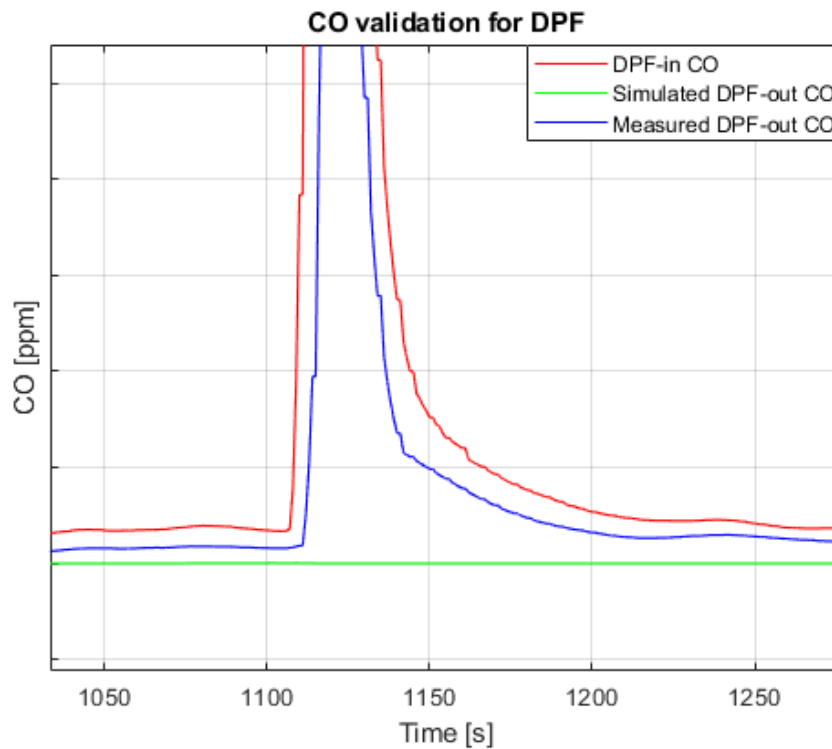


Figure E.3 A zoom-in of the CO concentrations at 1120 s.

The measured CO is more than the simulated CO. The mismatch is mainly due to that the CO is generated in soot oxidation in the real system while the model doesn't account for.

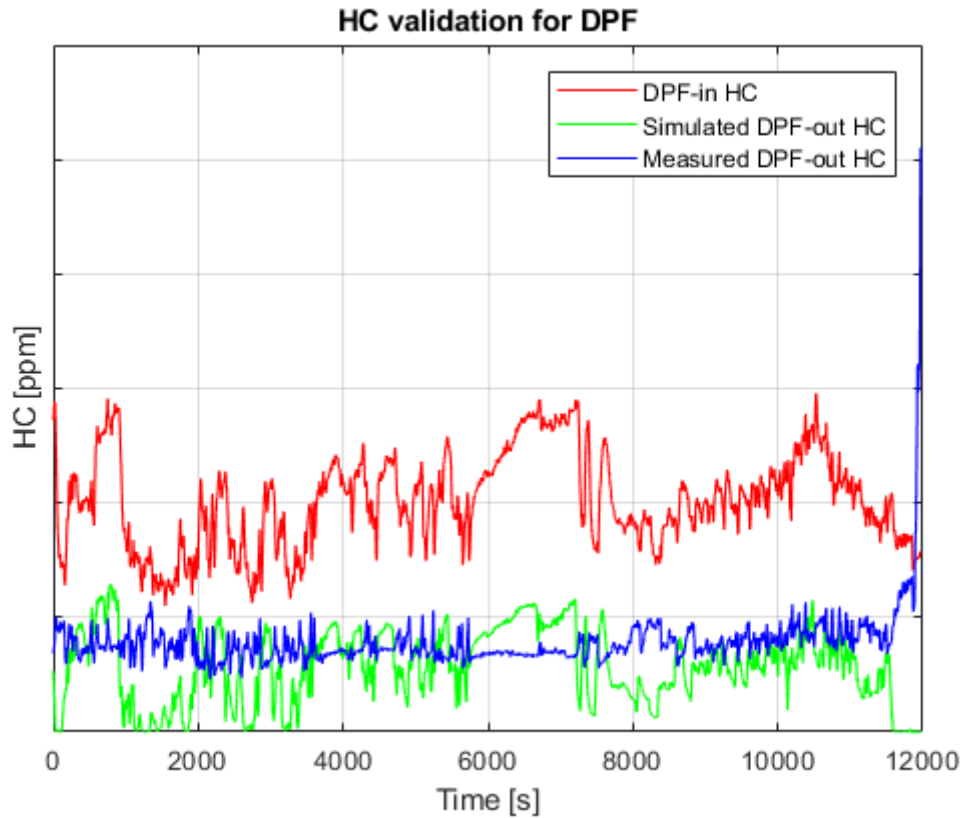


Figure E.4 Simulated (green line) and measured (blue line) outlet concentrations of HC, and together with inlet HC concentrations (red line). The measurement HC concentrations should be zero at high temperature. Here the measured HC is not zero which is regarded as the measurement error. The errors are however very low. Hence the result is acceptable.

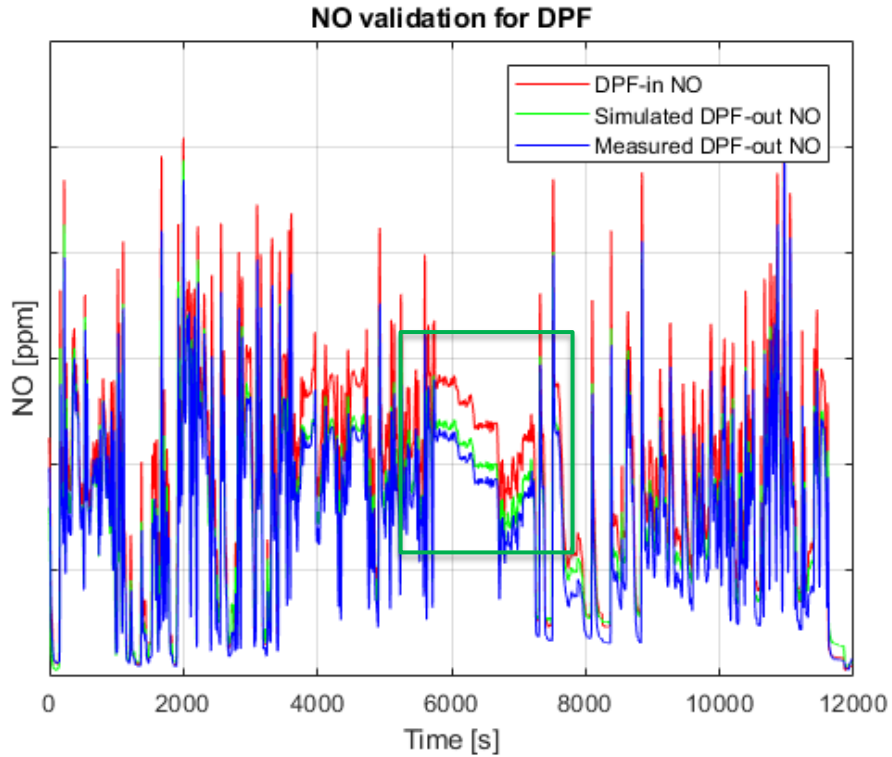


Figure E.5 Simulated (green line) and measured (blue line) outlet concentrations of NO, and together with inlet NO concentrations (red line). The marked region is a zoom-in look which is presented in figure E.6.

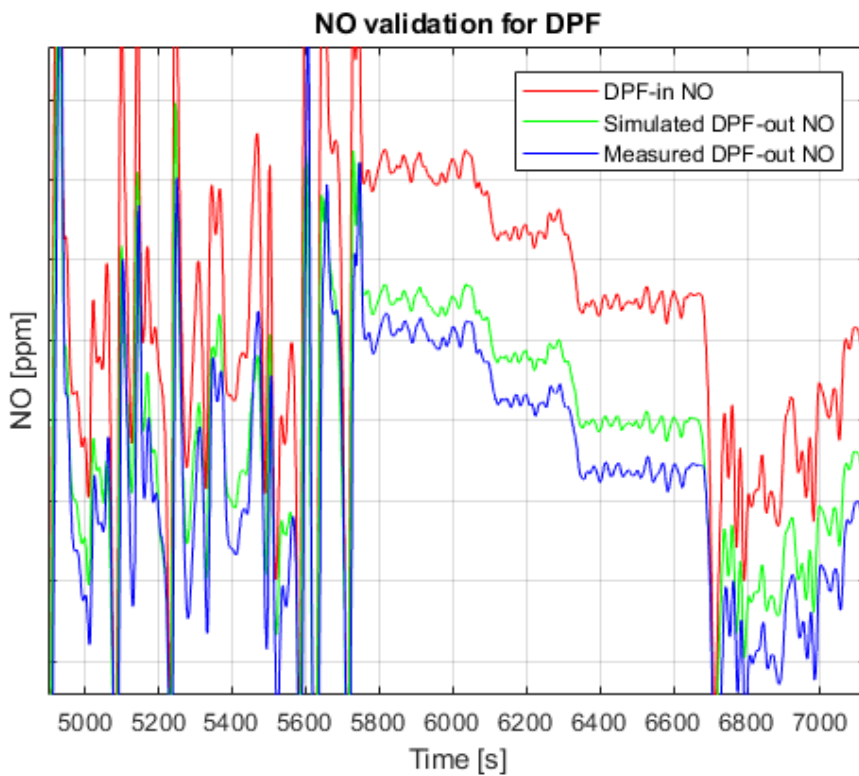


Figure E.6 A zoom-in of the NO concentrations between 5000 and 7000 s.

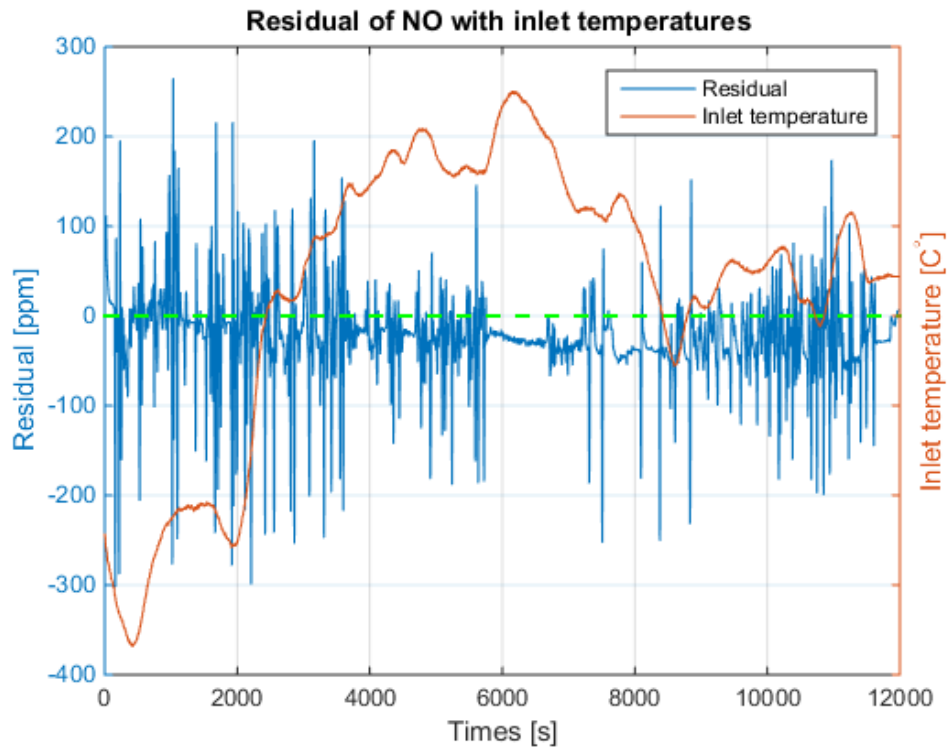


Figure E.7 The residual of NO concentrations (blue line) is compared with the inlet temperature (red line).

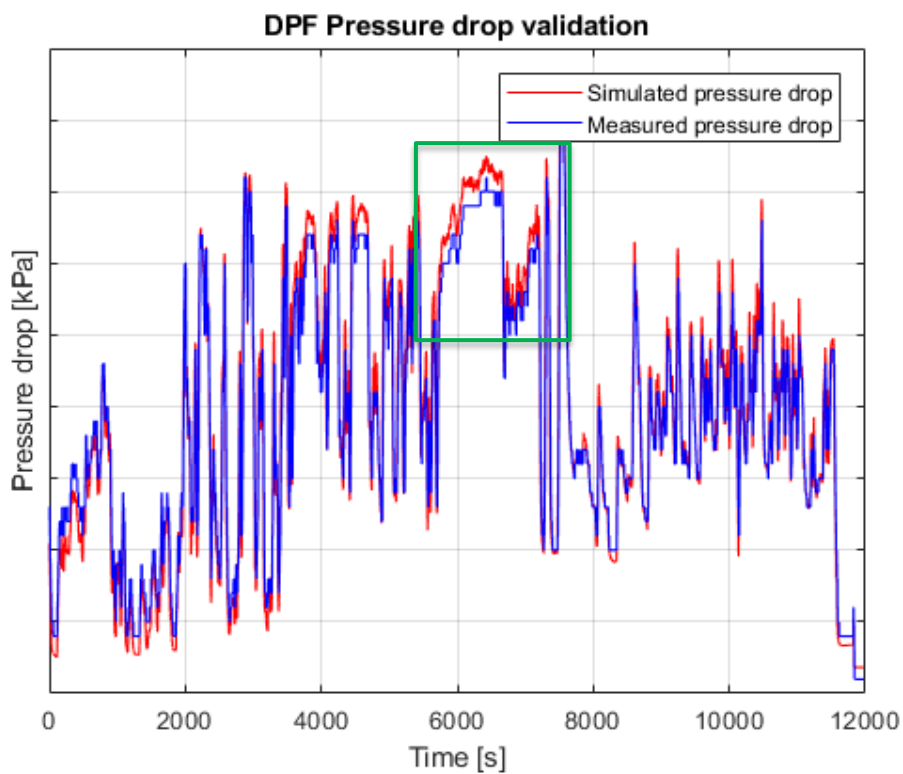


Figure E.8 Simulated (red line) and measured (blue line) pressure drop across the DPF. The marked region is a zoom-in look which is presented in figure E.9.

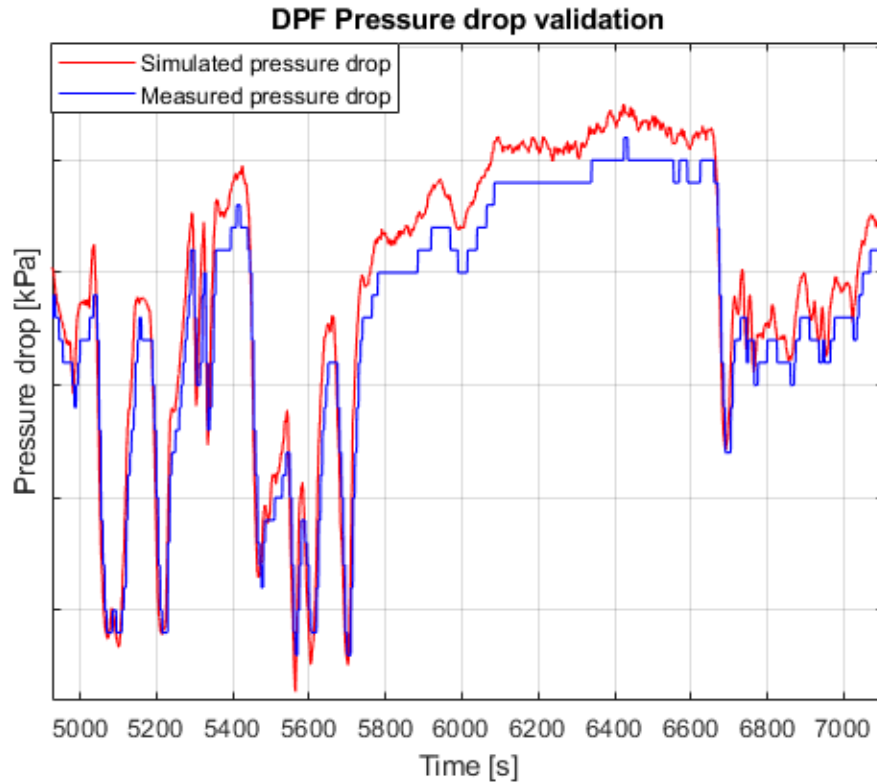


Figure E.9 A zoom-in look of the pressure drop between 5000 and 7000 s.

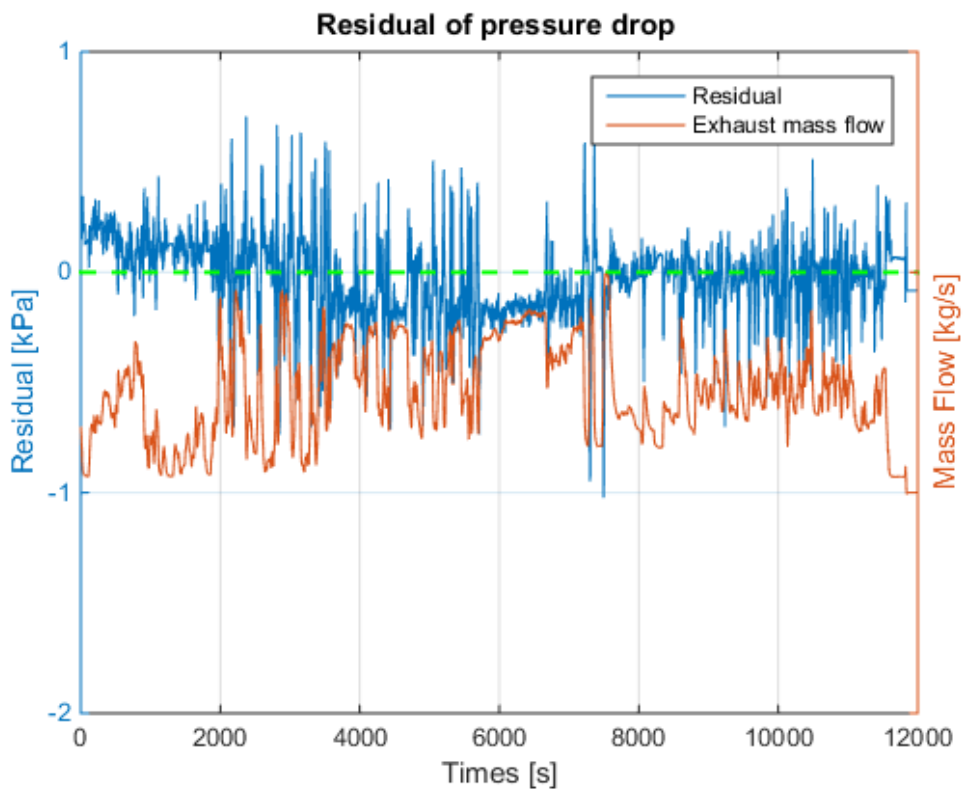
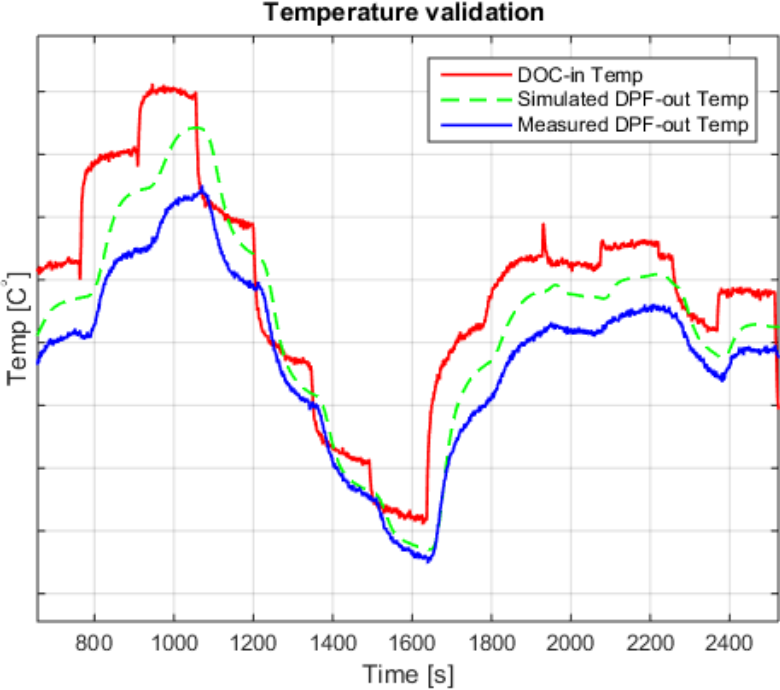


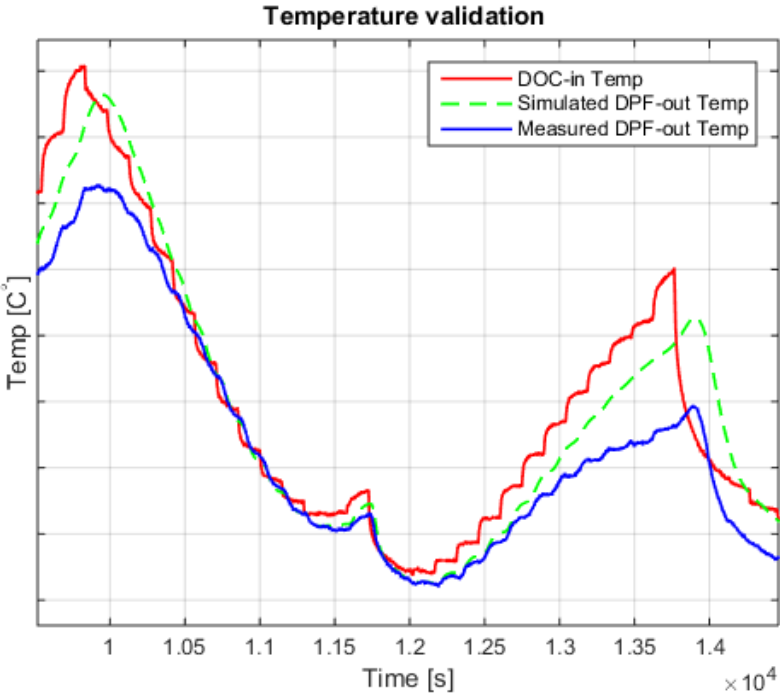
Figure E.10 The residual (blue line) of the pressure drop compared with the mass flow (red).

F Combined DOC and DPF model validation using PLM

In this appendix F, the validation results of temperature and the other gas species concentrations and pressure drop are presented here.



(a)



(b)

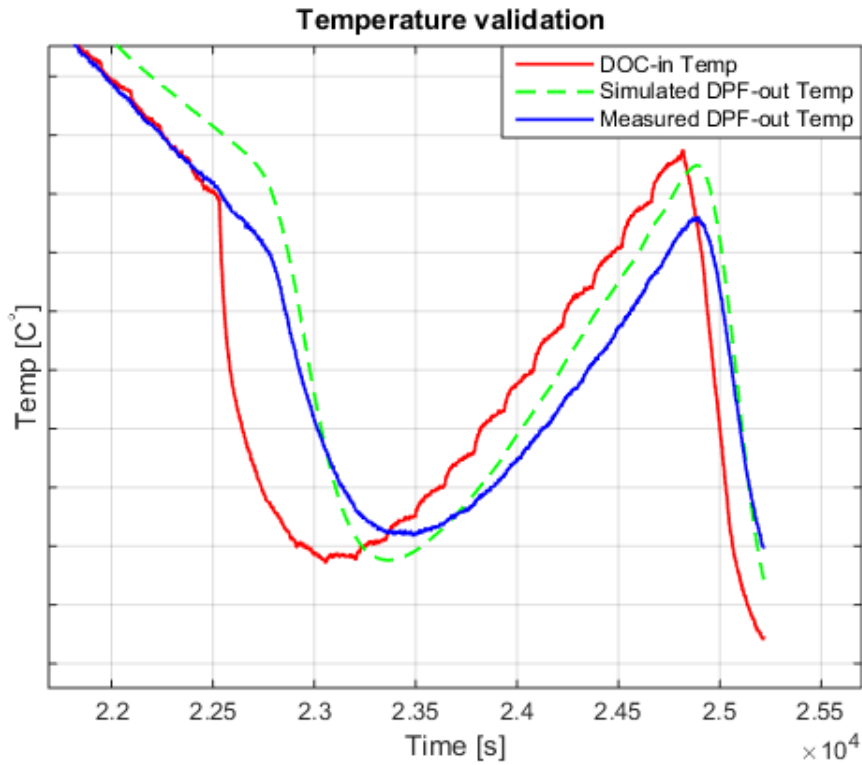


Figure F.1 Zoom-in plots of the temperature. Measured (blue line) and simulated (green line) outlet temperature and together with the inlet temperature (red line).

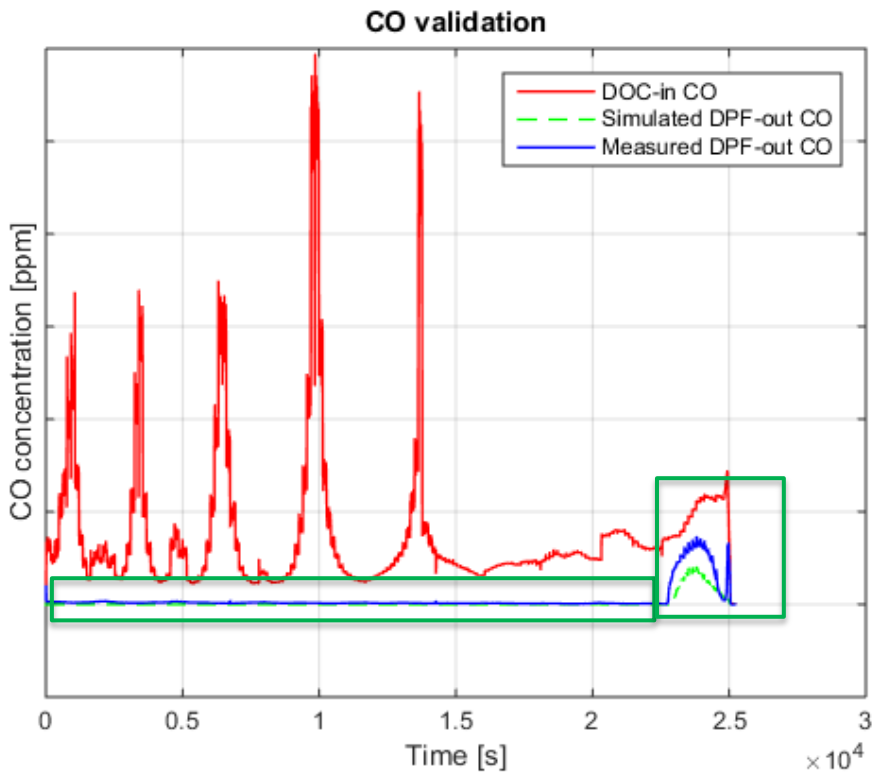


Figure F.2 Measured (blue line) and simulated (green line) outlet concentrations of CO, and together with the inlet CO (red line). The marked region is a zoom-in look which is shown in figure F.3.

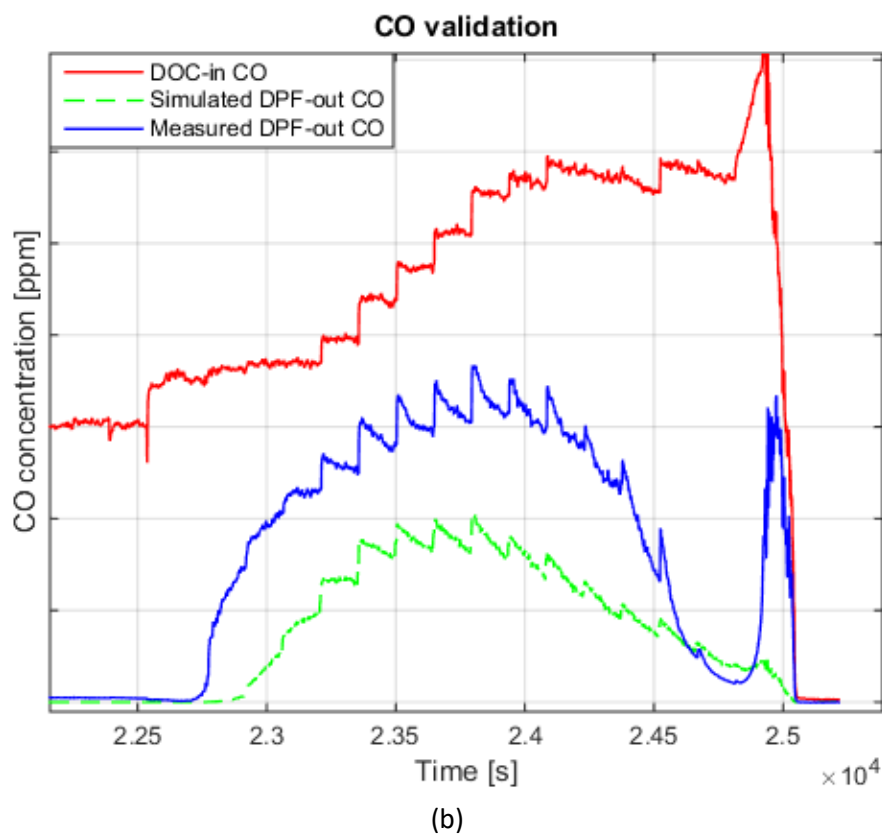
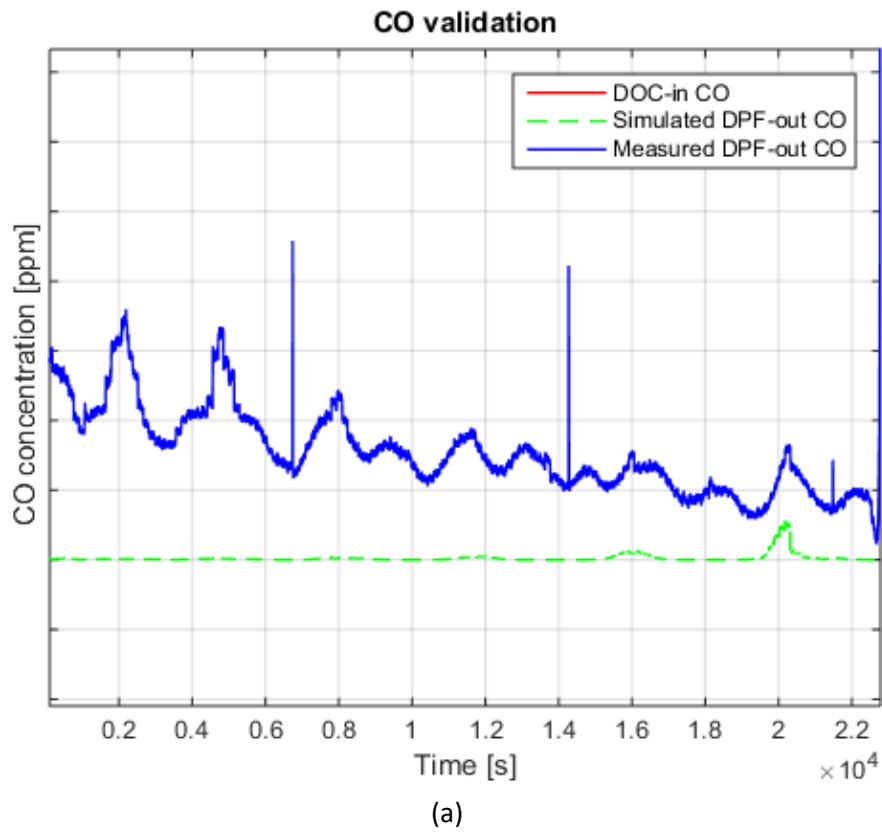


Figure F.3 The measured CO is higher than the simulation. This is mainly due to the CO formations during active and passive regeneration in DPF, whereas the DPF module doesn't contain any CO formations.

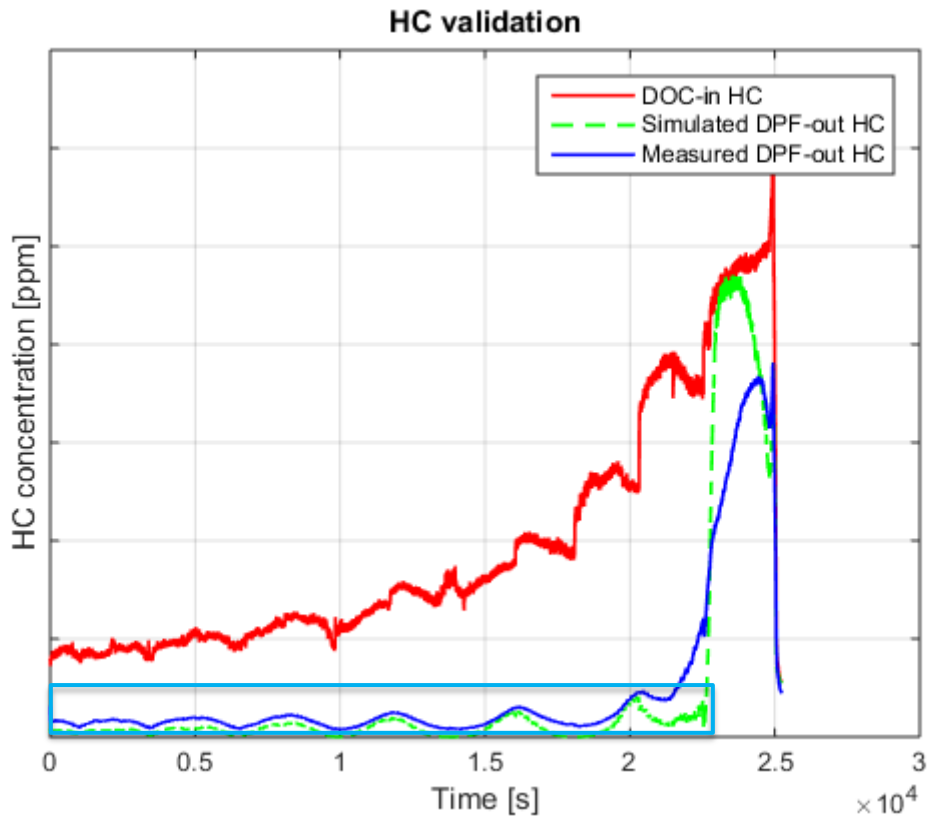


Figure F.4 Measured (blue line) and simulated (green line) outlet concentrations of HC, and together with the inlet HC (red line). The marked region is a zoom-in look which is shown in figure F.5.

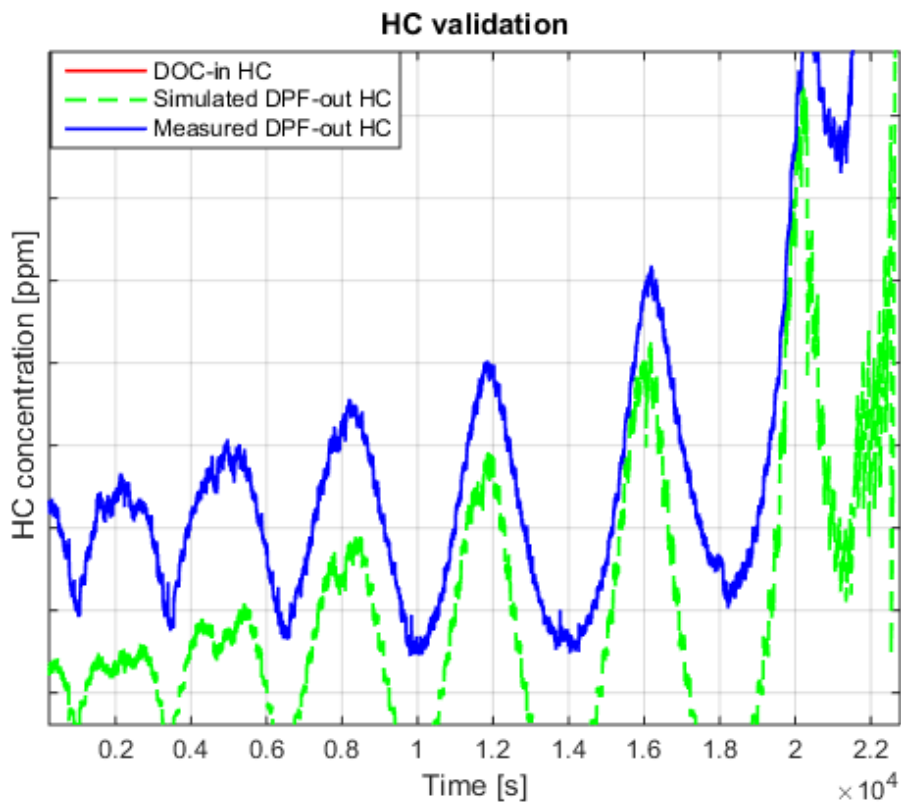


Figure F.5 A zoom in of the HC concentrations between 0 and $2 \cdot 10^4$ s. There are measurement errors in the beginning of the PLM. The measured HC should be zero at high temperature.

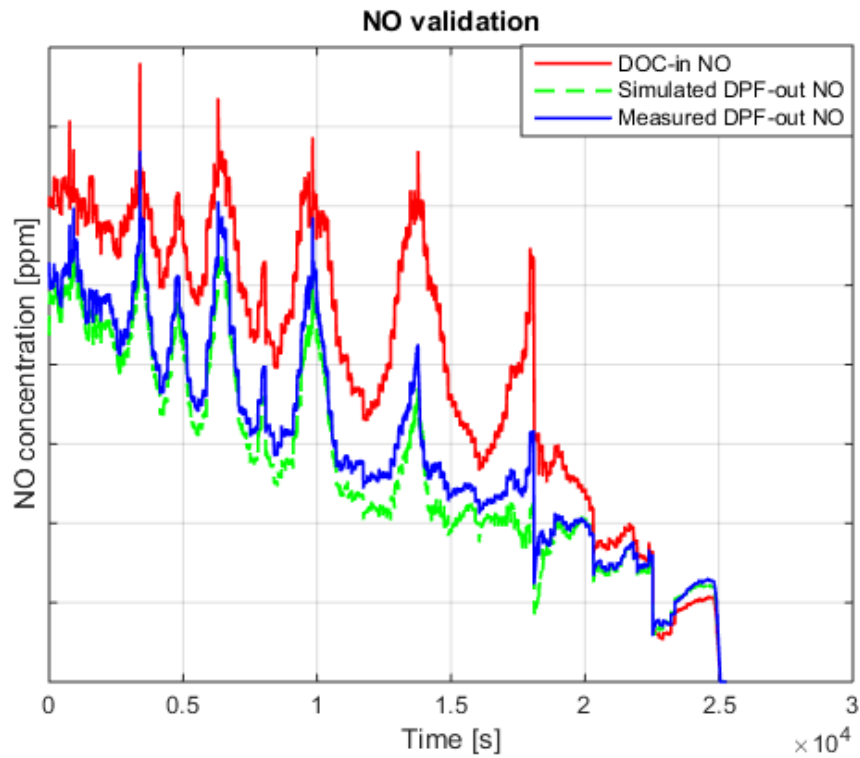


Figure F.6 Measured (blue line) and simulated (green line) outlet concentrations of NO, and together with the inlet NO (red line).

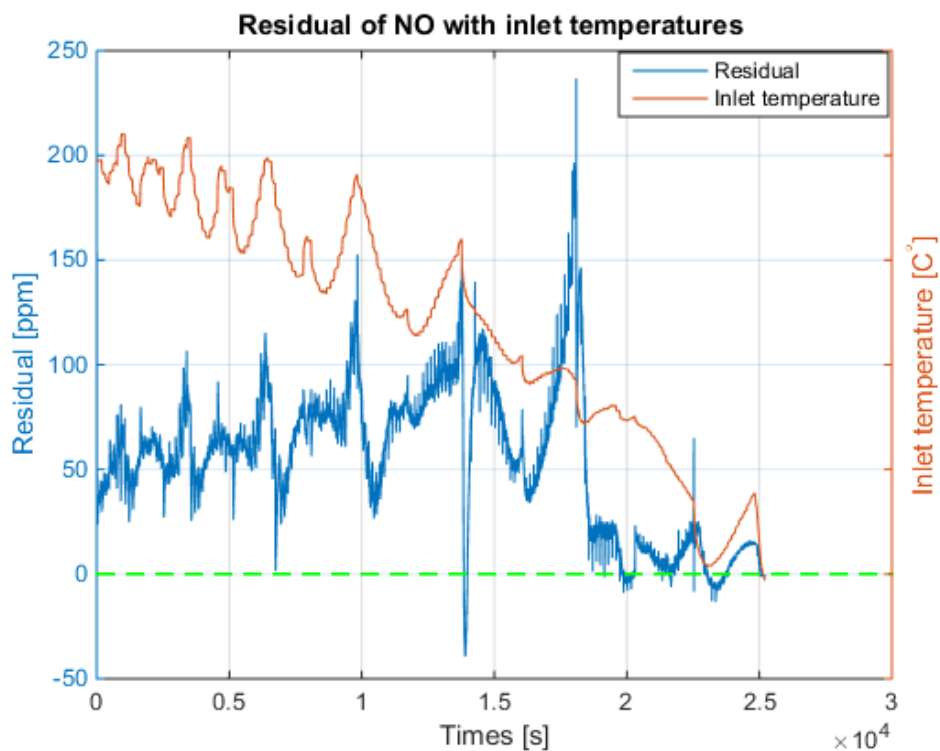


Figure F.7 The residual (blue line) is compared with the inlet temperature (red line). The residual is nearly positive, meaning that the model under-predicts the NO concentrations.

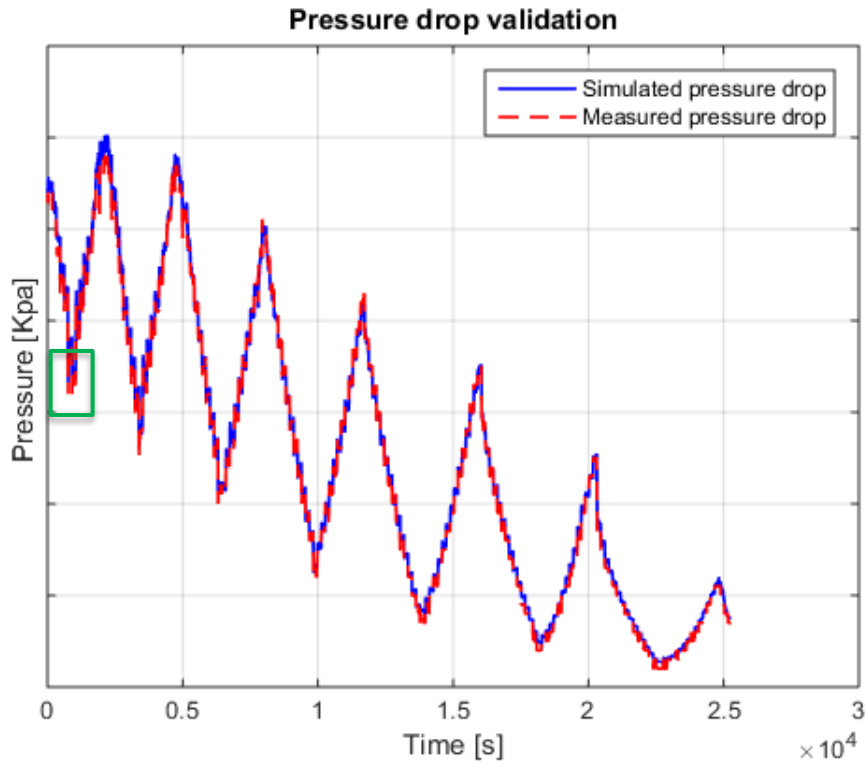


Figure F.8 Measured (red line) and simulated (blue line) pressure drop over both DOC and DPF. The marked region is a zoom-in plot which is shown in figure F.10.

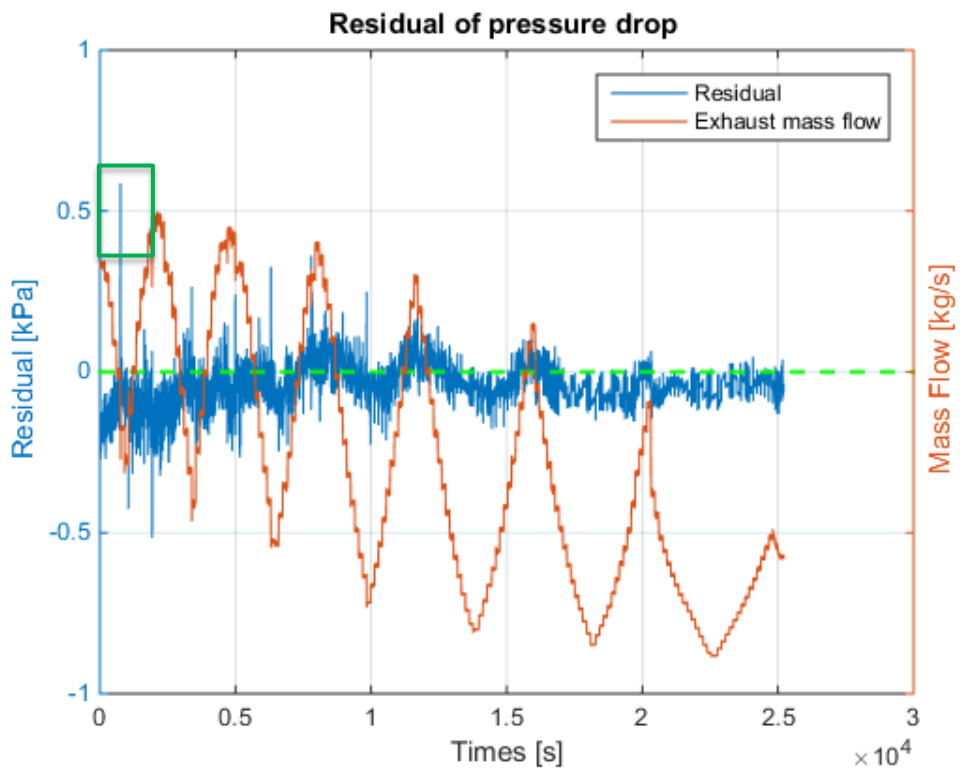


Figure F.9 The residual (blue line) is compared with the mass flow (red line). The marked region is a zoom-in plot which is shown in figure F.10.

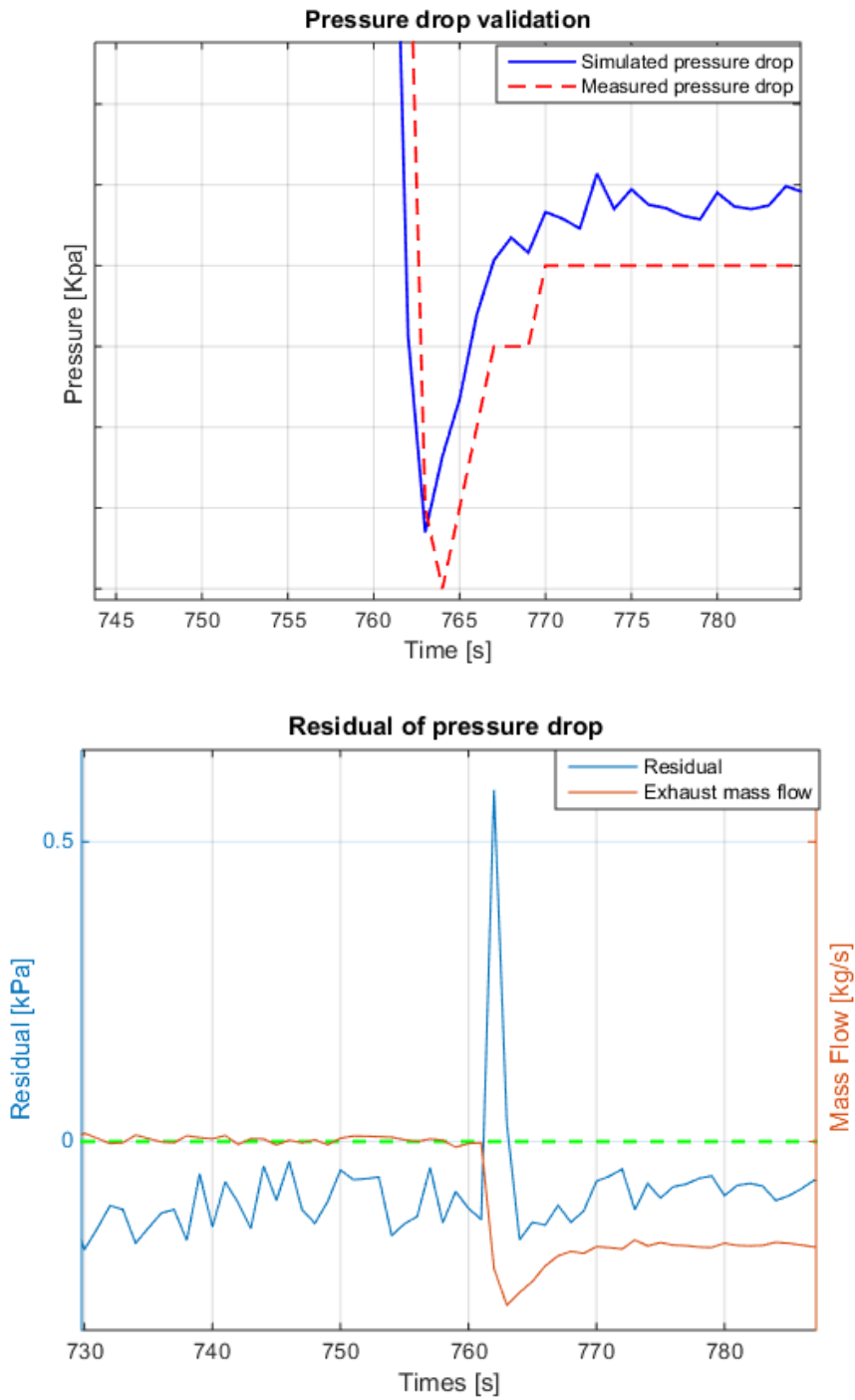


Figure F.10 The error of the pressure drop at 765 s. This is a large error which is higher than 0.5 kPa. The deviation is due to the delay.

G Combined DOC and DPF model validation using NRTC

In this appendix G, the validation results using NRTC are presented here.

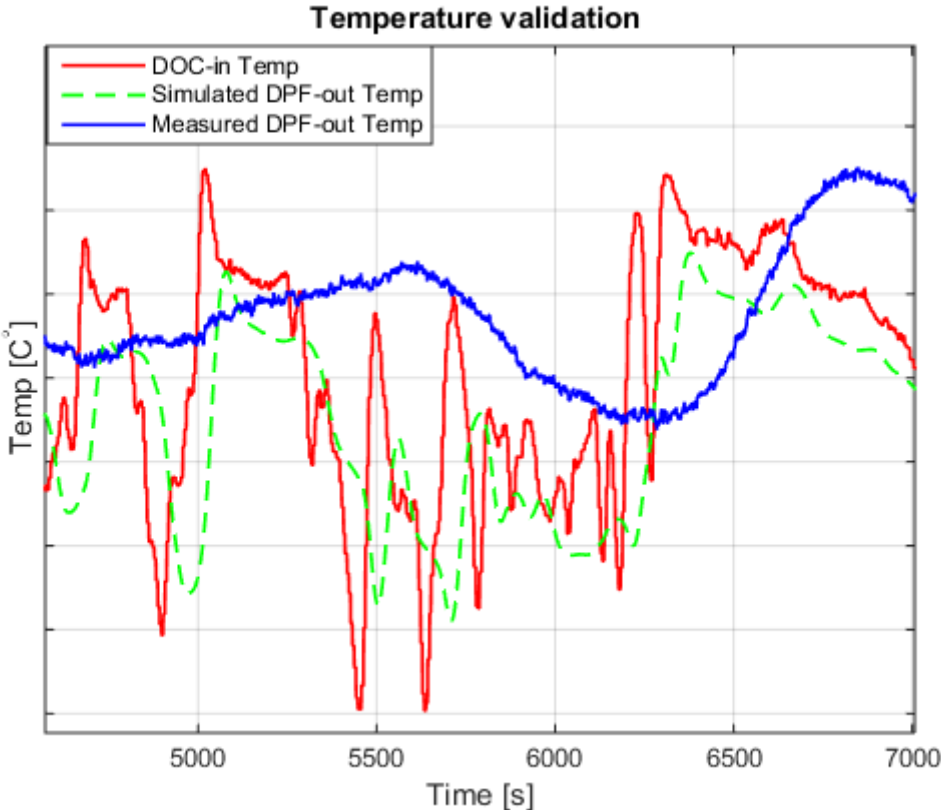


Figure G.1 A zoom-in of the temperature between 5000 and 7000 s.

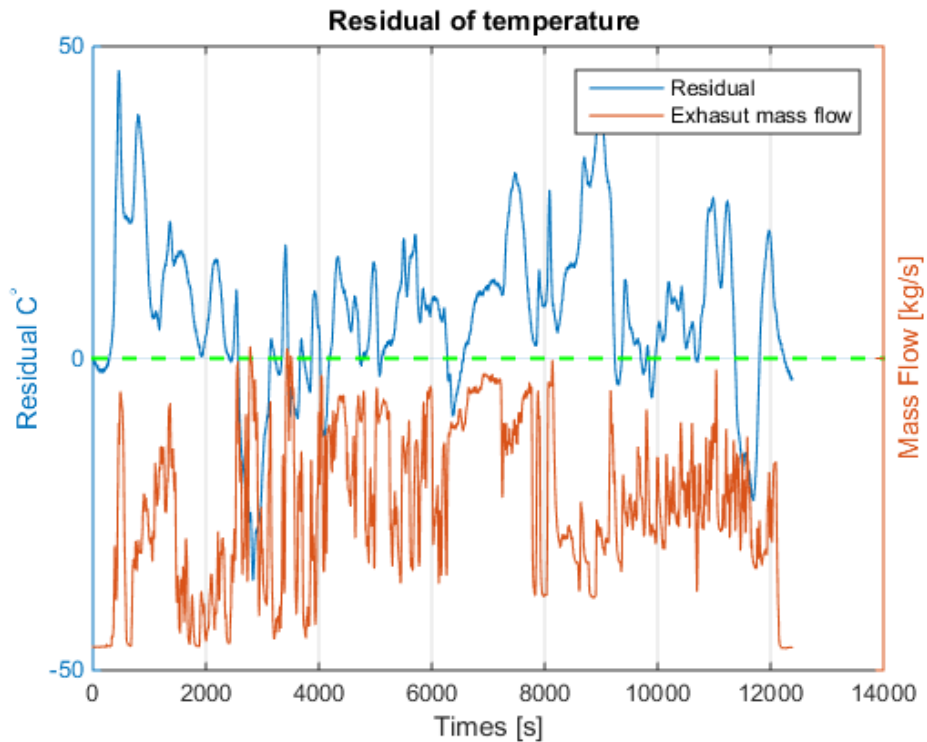


Figure G.2 The residual (blue line) is compared with the exhaust mass flow (red line). This implies that the errors between model and test are kind of big during the transient points.

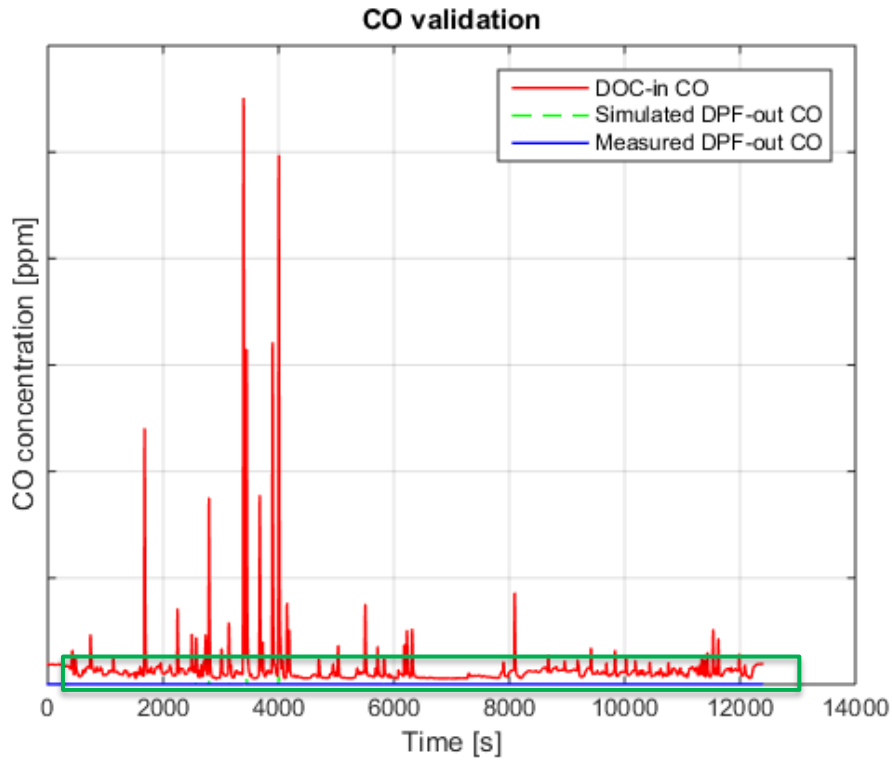


Figure G.3 Measured (blue line) and simulated (green line) outlet concentrations of CO, and together with the inlet CO (red line). there are many spikes in the inlet CO concentrations.

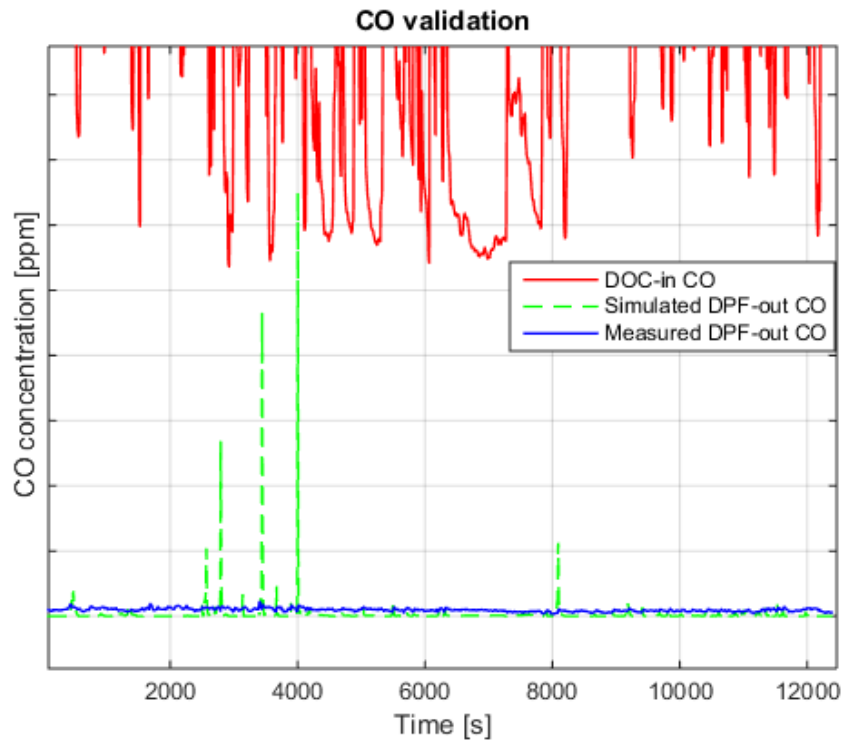


Figure G.4 A zoom in of the CO concentrations of NRTC cycle.

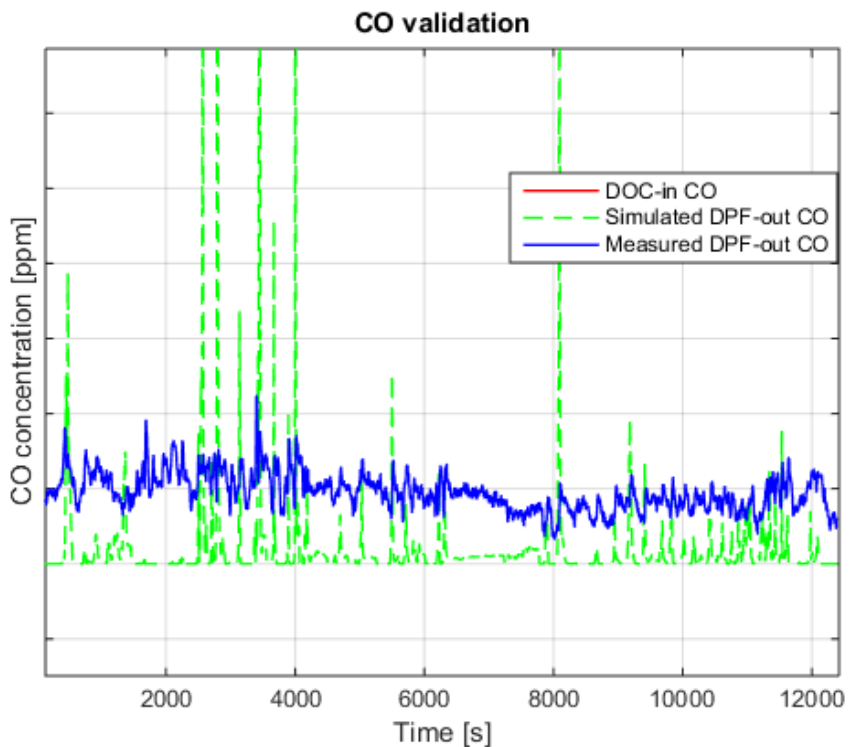


Figure G.5 A zoom in of the CO concentrations of NRTC cycle. The simulated results include several spikes, while the measurement is quite equally compared to the simulation. The incorrect temperature prediction can be one reason. The axial dispersion can be another reason. Also, the non-uniform inlet gas flow can result in the wrong conversion rate. Except spikes, the measurement is basically larger than the simulation. This is due to the CO formations in the DPF, while the model lacks CO formations which leads to the wrong prediction.

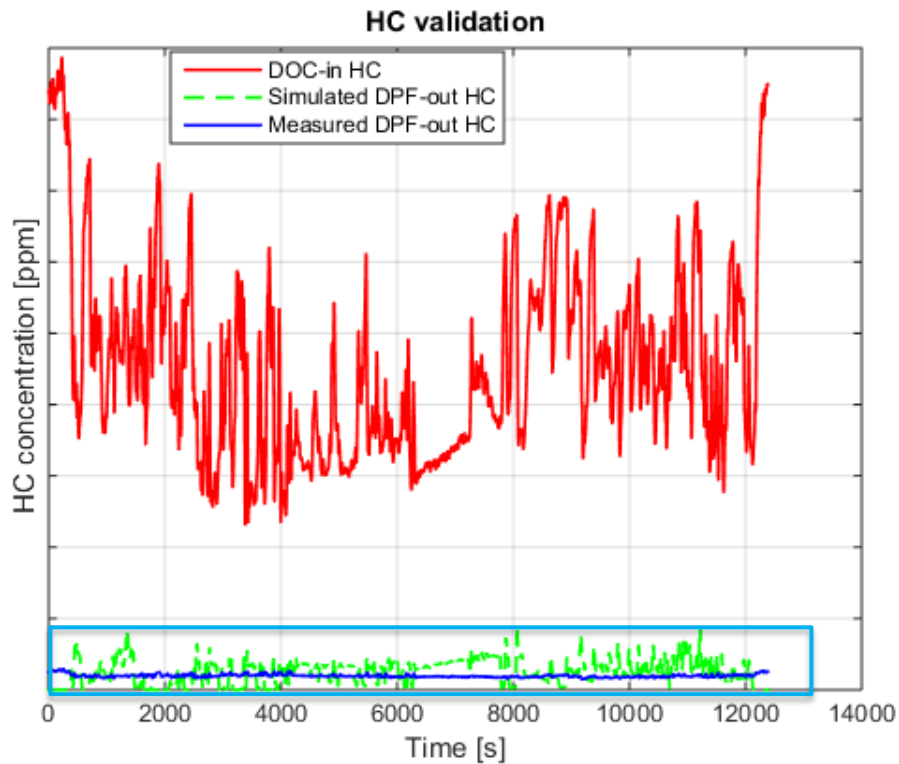


Figure G.6 Measured (blue line) and simulated (green line) outlet concentrations of HC, and together with the inlet HC (red line). The marked region is a zoom-in look which is shown in figure G.7.

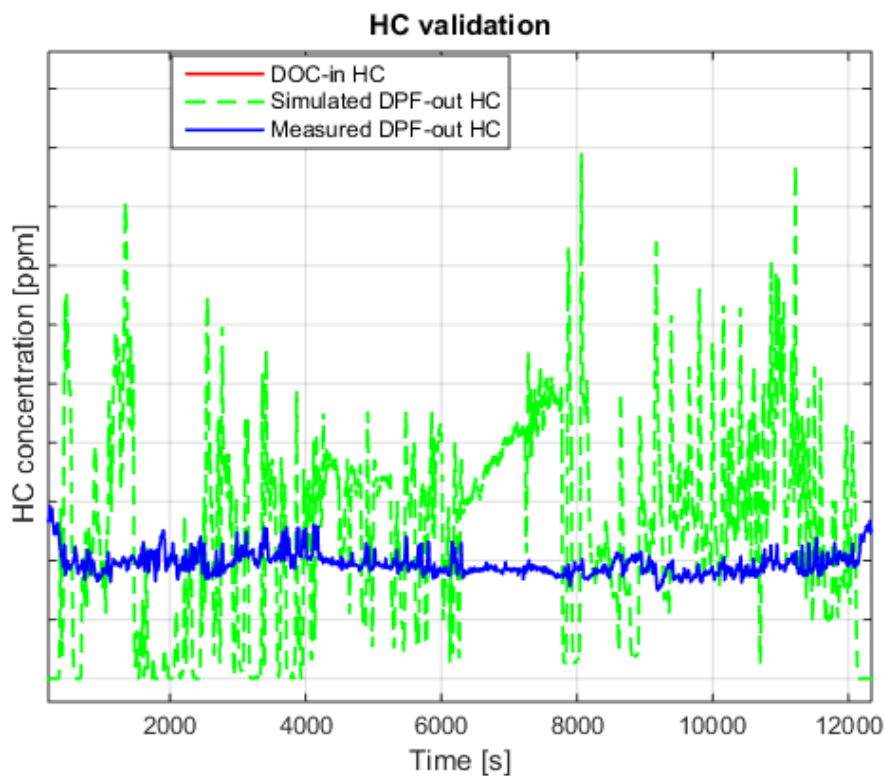


Figure G.7 A zoom-in of the HC concentrations of NRTC. The residuals are not high and below 10 ppm. For industrial perspective, the result is acceptable.

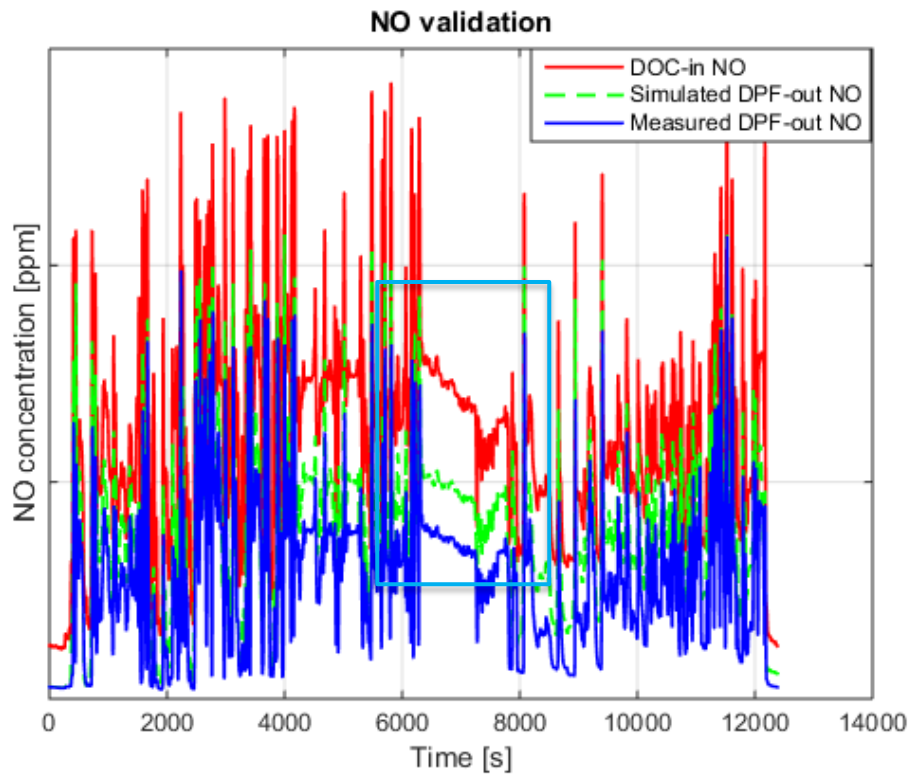


Figure G.8 Measured (blue line) and simulated (green line) outlet concentrations of NO, and together with the inlet NO (red line).

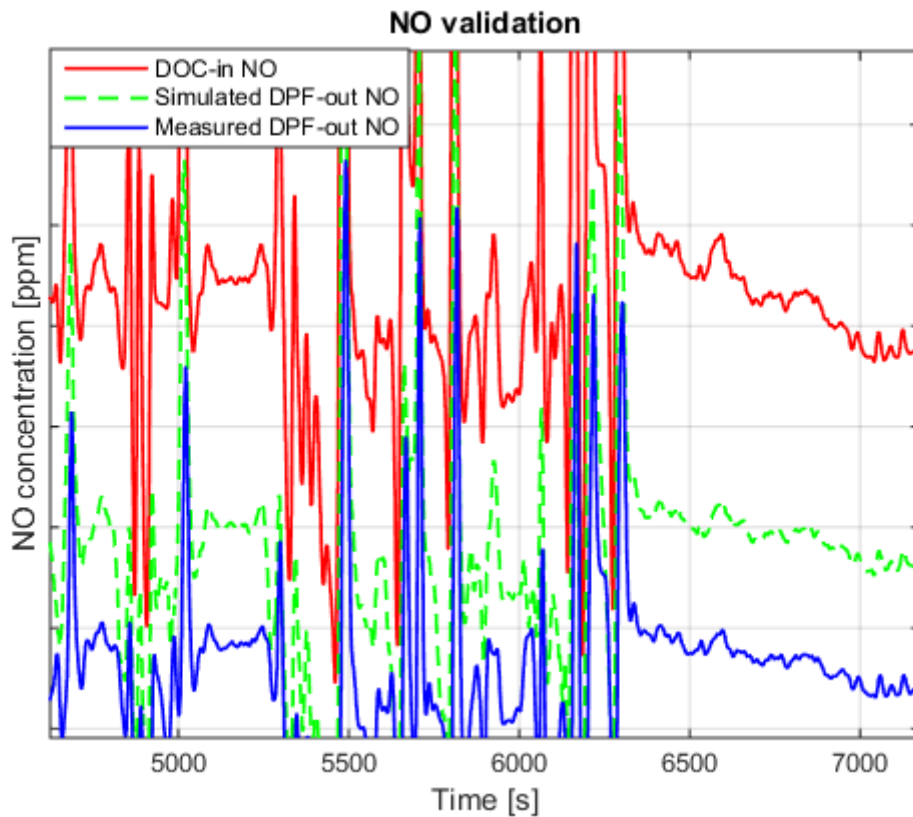


Figure G.9 A zoom-in of the NO concentrations between 5000 and 7000 s.

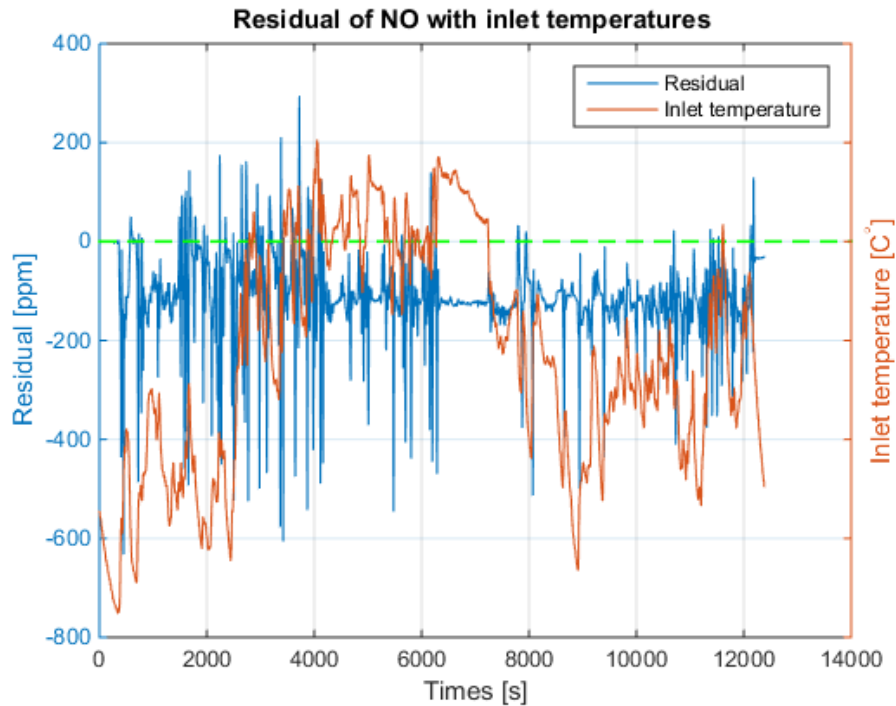


Figure G.10 The residual (blue line) is compared with the inlet temperature (red line). The residual is mainly negative, meaning that the model overpredicts NO concentrations. Comparing the result to figure F.7, on page 98, the model under-predicts the NO concentrations when using PLM as the validation test cycle. One of the main reasons is the temperature deviations. The model overpredicts the temperature with PLM validation while under-predicts the temperature with NRTC validation. Since the reaction rates have an exponential dependence on temperature, the difference of the temperature errors in PLM and NRTC can cause the large difference of NO predictions.

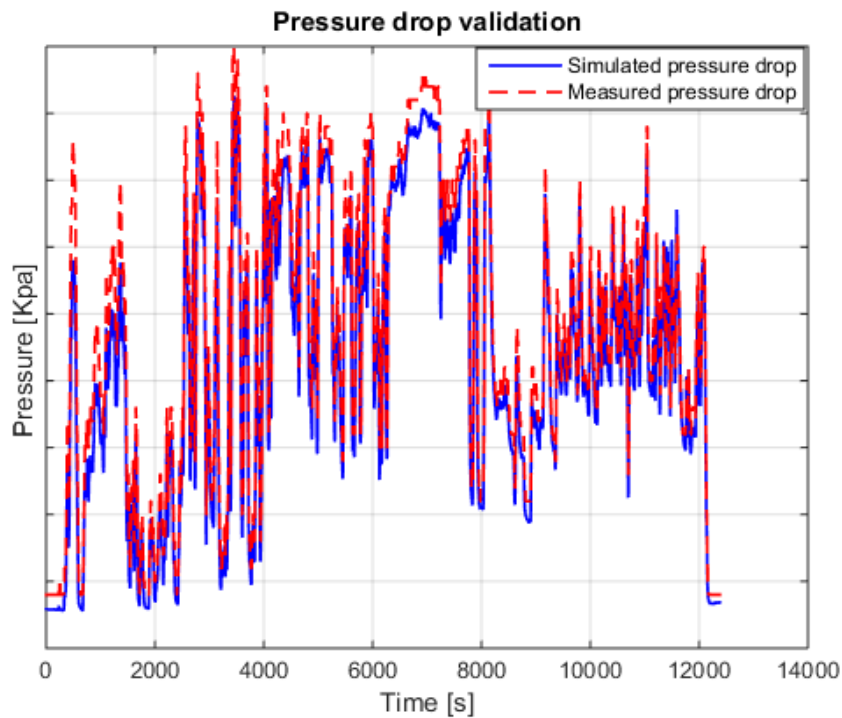


Figure G.11 Measured (red line) and simulated (blue line) pressure drop over both DOC and DPF.

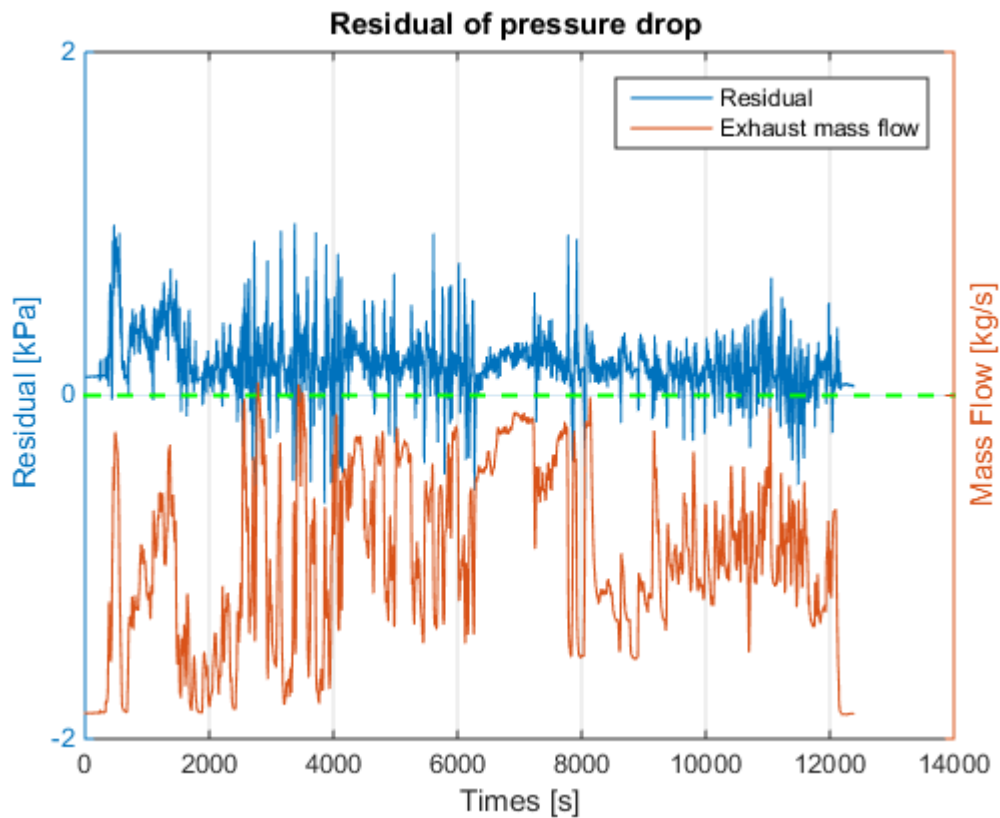


Figure G.12 The residual (blue line) is compared with the inlet temperature (red line). The maximum error is about 1 kpa. The errors from NRTC validation is higher than the PLM validation. The latter has the maximum error around 0.5 kpa. The reason can be the temperature deviation between the two cycles. One is overpredicted, the other is under-predicted. The temperature errors can affect the soot regeneration, which then affect the pressure drop. Another reason can be the transient test cycle. The fluctuating mass flow can result in higher pressure drop errors than the slow transient PLM cycle. Also, unknown initial soot loading can be the error source.